

**A STUDY OF COMPONENTS FOR LITHIUM AND SODIUM
BATTERIES AND OTHER STORAGE DEVICES**

**A STUDY OF COMPONENTS FOR LITHIUM AND SODIUM BATTERIES AND
OTHER STORAGE DEVICES**

By XAVIER DANIEL MICHAUD, M.A.Sc., B.Eng.

A Thesis Submitted to the School of Graduate Studies in Partial Fulfillment of the
Requirements for the Degree of Doctor of Philosophy

DOCTOR OF PHILOSOPHY (2019)
Department of Materials Science & Engineering

McMaster University
Hamilton, Ontario

TITLE: A Study Of Components For Lithium And Sodium Batteries And Other Storage Devices

AUTHOR: Xavier Daniel Michaud, M.A.Sc., (McMaster University), B.Eng., (Dalhousie University)

SUPERVISOR: Prof. Anthony Petric, Professor Emeritus, Ph.D., P.Eng.

CO-SUPERVISOR: Prof. Igor Zhitomirsky, Distinguished Engineering Professor, Ph.D., P.Eng.

NUMBER OF PAGES: XXIII, 177.

Lay Abstract

The goal of this work is to examine materials used in different types of electrochemical storage devices. The modification of resistive properties of β -alumina electrolytes are examined for use in high temperature sodium batteries. Electrophoretic deposition methods are used to rapidly make thin electrodes for lithium ion batteries and supercapacitors. The stoichiometric compound NaSi, a potentially safer and greener method of producing hydrogen gas, is characterized for a better understanding of its properties, and therefore production.

Abstract

An investigation of electrochemical storage device materials has been undertaken in four parts. The bulk and interfacial resistance of Na⁺ beta-alumina tubes were separated using a galvanostatic charge-discharge method. Sodium silicide was characterized to better understand its synthesis. BiMn₂O₅ was produced using a sol-gel method and tested for pseudocapacity. Different lithium ion anode and cathode materials were deposited using a new electrophoretic deposition method.

A novel galvanostatic charge-discharge method was developed for the determination of bulk and interface resistance in Na⁺ beta-alumina solid electrolytes [**BASE**]. Dense and duplex BASE tubes were tested by varying the exposed surface area. The results of dense BASE tube pairs were used to determine the bulk and interfacial resistance components, while duplex BASE tubes were tested to determine the reduction in interfacial resistance. It was found that duplex tubes had reduced the interfacial resistance by 75%, when compared to a uniformly dense electrolyte.

Sodium silicide was characterized using various methods to better understand the phase and the Na-Si phase diagram. EMF experiments using Na⁺ BASE tubes was used to determine the activity in the silicon rich region of the phase diagram, which showed a sodium activity of 0.5 at 550°C. TGA/DSC was used to determine phase transformation temperatures, as well as the heat of formation for NaSi, which was recorded to be below 1 kJ mol⁻¹.

A sol-gel precipitation method was used to produce fine BiMn_2O_5 powders used for supercapacitors. The powders resulting from a consistent method were tested for pseudocapacitance using bulk and thin film electrodes. Bulk electrodes had a gravimetric capacitance of 10 F g^{-1} , while thin film electrodes only reached 2.6 F g^{-1} .

Lithium ion battery anode ($\text{Li}_4\text{Ti}_5\text{O}_{12}$) and cathode (LiFePO_4 , LiMn_2O_4 , $\text{LiMn}_{1.5}\text{Ni}_{0.5}\text{O}_4$) materials were electrophoretically deposited with the assistance of PAZO-Na and CMC-Na. Cathodes were successfully deposited on aluminium substrates, and were tested in the potential window 2 – 4.3 V. The LiFePO_4 cathodes showed capacity of 146.7 mAh g^{-1} at C/10, while showing capacity retention of 103% after 50 cycles.

Acknowledgements

As I begin the next steps in my career, I must look back to the past six years here at McMaster University. They were filled with many trials, from the personal to the professional. There were many victories, and many more disappointing failures. If it wasn't for the people who have supported and encouraged me, pursuing my PhD would have remained an unreachable dream. I would like to thank you all from the bottom of my heart.

Dr Anthony Petric, thank you for the dedication and support you provided me over the years. Throughout these six long years, you have given me the guidance to grow as an aspiring researcher, to one that is better prepared to tackle all aspects of a life dedicated to science. Thank you for placing your trust in my abilities, and for not giving up on me. I wish you the best of retirements.

I would like to thank Dr Igor Zhitomirsky for accepting me into his lab when I branched out to find new projects. You and your group accepted me with the warmest hearts. For too long I had worked alone, and finding camaraderie with your students not only gave me the drive to finish my thesis, but general hope in the next generation of scientists.

I would like to thank Dr Gillian Goward for putting the time and effort of being part of my supervisory committee. Your participation in my yearly meetings and examinations was crucial in refining my abilities and thought processes.

I appreciate the various members of the university who I have encountered and worked with. I appreciate the help and advice given by Dr Alex Adronov, Dr James Britten, Doug Culley, Frank Gibbs, Victoria Jarvis, Xiaogang Li, Ed McCaffrey, and to all my fellow graduate students. Special thanks go to Dr Joey Kish, Dr Dmitri Malakhov, and Dr Hatem Zurob for the invaluable advice throughout my final years at McMaster.

I would also like to thank Jim Garrett. You have provided me invaluable insight from the endless knowledge you have accumulated. There is no one with whom I would have rather worked alongside. I only wished that I could have learned more from you.

To my family, thank you for cheering me on from afar. Your expectations and hopes for me helped me push through the clutter of life and find what was important for me. Most importantly, I must express my love and gratitude to my wife, Chiao-Ting Shen. You stood by me through all the years of hard work, frustration, and disappointments. When all seemed to crumble, you were the rock that I held onto as we weathered the roughest storms. I am excited to continue our journey through life together, into a brighter and thrilling future. I can only hope to now make your dreams come true.

Table of Contents

Lay Abstract	iii
Abstract	iv
Acknowledgements	vi
Table of Contents	viii
List of Figures	xii
List of Tables.....	xviii
List of Abbreviations and Symbols.....	xix
Abbreviations	xix
Symbols.....	xx
Declaration of Academic Achievement	xxii
Chapter 1: Introduction	1
Chapter 2: Literature Review	4
High Temperature Molten Sodium-Anode Batteries	4
Beta-Alumina Solid Electrolyte [BASE]	4
Ionic Conductivity in BASE	6
Ion Exchange in BASE	9
BASE Synthesis & Production.....	11
Sodium Sulfur Cell.....	13
Sodium Metal Halide Cell.....	17
Planar Cells	20
Lithium Ion Batteries.....	22
Cathode Materials	23
Intercalation Cathodes.....	24
Conversion Cathodes.....	25
Anode Materials	27
Carbon-Based Anodes.....	27
Lithium Titanate ($\text{Li}_4\text{Ti}_5\text{O}_{12}$) Anodes.....	28
Capacitors.....	28
Bismuth Manganese Oxide (BiMn_2O_5).....	31
Electrophoretic Deposition.....	32

Sodium-Silicon System	36
Proposed Na-Si Phase Diagrams	38
Chapter 3: Problem Statement	41
Chapter 4: Experimental Procedure	43
Sol-gel synthesis of complex ceramics	44
Sodium β -Alumina Powders & Sodium-Aluminate Eutectic Seal	44
Bismuth Manganese Oxide Powder	44
Forming of Ceramic Parts	45
Pressing, Machining, and Sintering of α -Alumina caps	45
Slip Casting and Sintering of β -Alumina Electrolyte Tubes	46
Sealing of β -alumina solid electrolyte tubes to Alumina Caps	50
Glass Seals	50
Ceramic Seals	51
β -Alumina Solid Electrolyte Ionic Resistance Testing	52
Sodium Silicide Characterization	55
Thermodynamic Study of Na-Si System	55
Conductivity of NaSi experiment	55
DTA / DSC Characterization	57
Determination of NaSi Melting Point	58
Production of Electrochemical Electrodes using Ceramics for Energy Devices	60
Electrophoretic Deposition of Ceramic Materials	60
BiMn ₂ O ₅ Loaded on Nickel Foam Electrode	61
Testing of Electrochemical Electrodes	62
Chapter 5: Duplex Solid Electrolyte	64
Experimental Considerations	64
Assumptions and Mathematical Derivations	64
Wettability of BASE Tube	67
PMMA vs Carbon Powder as Pore Formers	69
Internal Porosity vs External Porosity	72
Conductivity Measurements of Cells	75
Dense Electrolyte Cells	75
Duplex Electrolyte Cells	78

Experiment Design Failures	80
Conclusion of β -Alumina Solid Electrolyte Conductivity Testing	81
Chapter 6: Sodium Silicide and Na-Si Binary System.....	82
Electronic Conductivity.....	83
Shortcomings of Conductivity Measurements	96
Autoclave Melting.....	97
Synthesis of NaSi inside the Autoclave	101
High Temperature XRD Analysis	102
DTA & DSC Experiments.....	104
Approximation of Heat of Reaction for NaSi from DTA signals	110
DSC Experiments.....	111
EMF Experiments.....	116
Concluding Phase Diagram.....	118
Chapter 7: Bismuth Manganese Oxide Supercapacitors.....	121
Synthesis of BiMn_2O_5	121
Testing of Material for Pseudocapacitance	128
Bulk Electrode Capacitance	128
Thin Film Electrodes Capacitance	131
Conclusion to BiMn_2O_5 Capacitance	136
Chapter 8: Electrophoretic Deposition of Lithium-ion Battery Materials	137
EPD Coating of Li^+ Compounds.....	137
Anode Materials / Carbon Black on Aluminum Using CMC	144
$\text{Li}_4\text{Ti}_5\text{O}_{12}$ / Carbon Black on Copper Anodes	147
Performance of Electrodes	148
LiFePO_4 / Carbon Black on Aluminum Using CMC	148
LiMn_2O_4 and $\text{LiMn}_{1.5}\text{Ni}_{0.5}\text{O}_4$ with Carbon Black on Aluminium Using CMC	149
Conclusion to Li-ion Battery Electrode Materials	151
Final Conclusions.....	152
References	155
Appendix.....	170
Appendix: Ceramic Compositions Used for Sealing BASE Tubes	170
Appendix: Impedance Spectroscopy of BiMn_2O_5 Electrodes.....	171

Bulk Electrode (Pre-Ball Milling 2.65 μm).....	171
Bulk Electrode (Ball Milling 1.28 μm)	172
Bulk Electrode (Ball Milling 0.23 μm)	173
Thin Film Electrode (Seperated 1 μm).....	174
Appendix: Important Powder Diffraction Profiles.....	175
Sodium Silicon System	175
Bismuth Manganese Oxide System.....	177

List of Figures

Figure 1: Idealized structures of Beta & Beta" (Reproduced from [9]).....	5
Figure 2: Effects of Mixed β/β'' on Resistivity [7].....	7
Figure 3: Arrhenius Plot of Conductivities of β and β'' [12].....	9
Figure 4: Ion exchange in BASE using molten metal nitrate bath [6].....	11
Figure 5: Na-S Battery Architecture [22].....	14
Figure 6: Voltage Profile during discharge of Na-S cell [22].....	15
Figure 7: Na-S Binary Phase Diagram [23].....	16
Figure 8: Na-NiCl ₂ cell architecture with secondary electrolyte [22].....	18
Figure 9: Na-NiCl ₂ cell voltage profile during charge & discharge (Modified from [24])18	
Figure 10: Open circuit voltages of various sodium metal chloride cells [23].....	19
Figure 11: Similarities and differences between tubular (tradition) and planar (advanced) NaS cells [37].....	20
Figure 12: Schematic of Li-ion battery operation [43].....	23
Figure 13: Crystal structures of a) layered (LMNCO) b) spinel (LMO) and c) olivine (LFPO) cathode materials [44].....	24
Figure 14: Specific Capacity of Intercalation Cathodes [4].....	25
Figure 15: Specific Capacity of Li-ion conversion cathodes [4].....	26
Figure 16: A simple dielectric capacitor.....	29
Figure 17: Schematic of anodic electrophoretic deposition.....	32
Figure 18: Crystal structures of a) NaSi, b) Type I clathrate, and c) Type II clathrate ($x=20$).....	37
Figure 19: Na-Si Binary Phase Diagram by Morito et al.....	40
Figure 20: Na-Si Binary Phase Diagram by Mali et al.....	40
Figure 21: Schematic of α -Al ₂ O ₃ cap used in BASE cells.....	46
Figure 22: Slip Casting Process for Duplex BASE tubes with inner surface porosity.....	48
Figure 23: Pre-sintering temperature profile for BASE tubes.....	50
Figure 24: Sintering temperature profile for BASE tubes.....	50

Figure 25: Temperature heating profile for Corning 1720 glass seal.	51
Figure 26: Temperature heating profile for the alternative seal.....	51
Figure 27: Temperature profile for eutectic composition ceramic seal.....	52
Figure 28: Schematic of coulometric bath. The arrows indicate the electron flow during titration into the cell [85].....	55
Figure 29: Working and reference (no nickel powder) electrode construction [85].....	55
Figure 30: 4-probe crucible for NaSi conductivity	56
Figure 31: Schematic for sealing of NaSi 4-probe system.....	56
Figure 32: DTA cell. Made from 300-series steel and screw (Mass >3000 mg). Chamber allowed ~100 mg NaSi.....	57
Figure 33: DSC cell. Made from 300-series steel (Mass ~800 mg). Chamber allowed for ~40 mg NaSi.....	57
Figure 34: Mounting of capillaries to the heating stage for high temperature XRD.	59
Figure 35: Swagelok [®] autoclave design, with long alumina crucible.....	59
Figure 36: Three-electrode cell for testing capacitance of BiMn ₂ O ₅	62
Figure 37: Inability to embed sodium metal into the porous layer of duplex cells.....	68
Figure 38: Effects of carbon coat on titration through porous layer of duplex cell.	68
Figure 39: Duplex BASE tube using graphite as a pore former. The left side is the dense layer, and the right side is the porous layer.....	70
Figure 40: Duplex BASE tube using PMMA as a pore former. Large interconnected spherical pores (left) with a thin (~50 μm) dense layer (right).	71
Figure 41: Porosity within dense layer of duplex BASE tubes due to the resuspension of PMMA powders during casting of dense slurry.....	74
Figure 42: Blocked porosity due to improper cleaning of alumina mould powder.	74
Figure 43: Resistivity profiles of BASE tubes as an inverse function of area.....	75
Figure 44: Resistance profiles of dense tubes as a function of area submerged into tin-sodium bath.	78
Figure 45: Resistance profiles of duplex tubes as a function of area submerged into tin-sodium bath.	79

Figure 46: Reaction of sodium and silicon to form NaSi in a “synthesis” cell.....	83
Figure 47: Reaction of sodium and silicon to form NaSi in a “reverse” cell.....	84
Figure 48: Conductivity of NaSi as an inverse function of Temperature.	86
Figure 49: Four-point conductivity setup for room temperature measurements of NaSi .	88
Figure 50: Conductivity of NaSi at room temperature using 0.5 cm metal probes.....	88
Figure 51: Conductivity measurements of NaSi at elevated temperatures (650°C).	89
Figure 52: XRD phase analysis of resulting powder from first 650°C NaSi conductivity experiment.....	90
Figure 53: Conductivity measurements of NaSi at elevated temperatures (550°C).	91
Figure 54: XRD phase analysis of resulting powder from 550°C NaSi conductivity experiment.....	92
Figure 55: Conductivity measurements of NaSi at elevated temperatures; reacted at 650°C and cooled down for multiple measurements.....	93
Figure 56: Close up of stability plateaus for step-down cooling of NaSi.	93
Figure 57: XRD phase analysis of resulting powder from NaSi conductivity experiment with cooling steps.....	94
Figure 58: Conductivity measurements of NaSi at elevated temperatures (750°C).	95
Figure 59: Estimation of the conductivity of NaSi at 750°C, based on the shift in slope during the conductivity measurement.	96
Figure 60: XRD phase analysis of NaSi near electrode (stainless steel or chromium)....	97
Figure 61: Image of autoclave samples Left) A1, Middle) A6, and Right) A7.	98
Figure 62: Sample A9, post autoclave heating at 875°C.	99
Figure 63: Sample A10, post autoclave heating at 900°C.	99
Figure 64: XRD analysis of NaSi powder prior and after autoclave heating (A2, A6, A7).	100
Figure 65: Autoclave sample A11. Elemental silicon and sodium were reacted to produce cylindrical NaSi slabs.....	102

Figure 66: High Temperature Analysis of NaSi in Capillary. The PEEK protective dome significantly interferes with the sample signal. The peak at $2\theta = 19.5$ is an artifact of the dome, but not from the polymer itself.....	103
Figure 67: High Temperature of NaSi capillary, with most PEEK dome artifacts removed. Intensity of scan normalized for $I_{Max}/I_0 = 100^\circ\text{C} + \text{Temperature}$	104
Figure 68: Secondary reactions with NaSi within DTA cells. Silicon from the NaSi reacted with cells.....	106
Figure 69: DTA of NaSi powder (SiGNa material).....	107
Figure 70: DTA of NaSi using a cell loaded from elemental Na (51 mol%) and Si (49 mol%).....	109
Figure 71: DTA from pure elements Na (14% mole basis).....	110
Figure 72: DSC Analysis of NaSi (Blue), Silver (Red), Zinc (Green). The dotted lines show the temperature difference between the sample and reference crucibles.....	112
Figure 73: Area of interest for the DSC analysis of NaSi (blue). Notice the high reproducibility of DSC signal.	114
Figure 74: Continuous ramp DSC of NaSi from elements.....	115
Figure 75: Sodium activity in NaSi (SiGNa).....	117
Figure 76: Average EMF values for NaSi, as a function of temperature below 570°C ..	117
Figure 77: Revised Na-Si phase diagram using new DTA/DSC and EMF data. Symbols represent phase transition onset temperatures of various DTA and DSC experiments...	120
Figure 78: XRD Analysis of BiMn_2O_5 powders calcined at various temperatures. Arrows point to characteristic peaks of Mn_2O_3 . All other peaks in sample K through O are from BiMn_2O_5	125
Figure 79: Repeatability of BiMn_2O_5 Sol-gel Synthesis at 750°C	125
Figure 80: Change in BiMn_2O_5 particle size with ball milling.	127
Figure 81: SEM image of BiMn_2O_5 powders after ball milling for 13 days.....	127
Figure 82: CV of BiMn_2O_5 (Pre Milling) at Left) 2, 5, 10 mV s^{-1} , Center) 20, 50, 100 mV s^{-1} . Gravimetric and areal capacitance (Right).....	129

Figure 83: CV of BiMn ₂ O ₅ (Milling to 0.65 μm) at Left) 2, 5, 10 mV s ⁻¹ , Center) 20, 50, 100 mV s ⁻¹ . Gravimetric and areal capacitance (Right).	129
Figure 84: CV of BiMn ₂ O ₅ (Milling to 0.25 μm) at Left) 2, 5, 10 mV s ⁻¹ , Center) 20, 50, 100 mV s ⁻¹ . Gravimetric and areal capacitance (Right).	130
Figure 85: SEM images of coating deposited using CMC Surfactant A) 10 V, C) 30 V, E) 50 V, and PAZO Surfactant B) 10 V, D) 30 V, F) 50 V.	132
Figure 86: FTIR analysis of BMO deposits using CMC (Left) and PAZO (Right). Comparative profiles of a) Pure polymer, b) Deposited polymer, c) Deposited Polymer + BMO.	133
Figure 87: XRD analysis of ball milled BiMn ₂ O ₅ with ZrO ₂ impurities.	134
Figure 88: Particle Size reduction of BiMn ₂ O ₅ powders through sedimentation in ethanol.	135
Figure 89: CV of BiMn ₂ O ₅ (Separated 1.00μm) at Left) 2, 5, 10 mV s ⁻¹ , Center) 20, 50, 100 mV s ⁻¹ . Gravimetric and areal capacitance (Right).	136
Figure 90: SEM images of LTO powders using CMC- (Left), and PAZO- (Right) assisted EPD, deposited at constant voltage of 10 V (A,B), 30 V (C, D), 50 V(E, F).	139
Figure 91: SEM images of LTO deposits at low magnification showing the formation of nodules due to agglomeration. A) CMC deposit at 50V, B) PAZO deposit at 50 V.	139
Figure 92: SEM images of LFPO powders using CMC- (Left), and PAZO- (Right) assisted EPD, deposited at constant voltage of 10 V (A,B), 30 V (C, D), 50 V(E, F).	140
Figure 93: SEM images of LMO powders using CMC- (Left), and PAZO- (Right) assisted EPD, deposited at constant voltage of 10 V (A,B), 30 V (C, D), 50 V(E, F).	141
Figure 94: SEM images of LMNO powders using CMC- (Left), and PAZO- (Right) assisted EPD, deposited at constant voltage of 10 V (A,B), 30 V (C, D), 50 V(E, F).	142
Figure 95: FTIR Profiles of Deposited CMC (Left) PAZO (Right) where: a) Pure Polymer, b) Deposited Polymer, c) LMO, d) LMNO, e) LTO, and f) LFPO.	143
Figure 96: Successful coating of LFPO-CB on Aluminium	145
Figure 97: Mass loading of LMO and LMNO cathodes as a function of deposition time.	146

Figure 98: Solution Depletion with each additional electrode deposited.....	146
Figure 99: Spallation of LTO-CB electrodes (copper) Left) CMC, Right) PAZO	147
Figure 100: Cell performance of LFPO cathode. Left) Cyclic Voltammetry at sweep rates of a) 0.1, b) 0.2, c) 0.4, d) 0.6, e) 0.8, and f) 1.0 mV s ⁻¹ . Center) Capacity with varying C-rates, Right) Potential Curve with varying C-rates.	149
Figure 101: Cycling of LFPO/C Cathode at charge-discharge current of C/10.....	149
Figure 102: Cycling of LMO/C Cathode at charge-discharge current of C/10.....	150
Figure 103: Cycling of LMNO/C Cathode at charge-discharge current of C/10.....	150
Figure 104: Capacity of LMO (Left) and LMNO (Right) with varying charge-discharge rates.	150
Figure 105-Appendix: Impedance characterization of Bulk BiMn ₂ O ₅ Electrode (Pre Milling, 2.65 μm). Top) Nyquist plots of complex impedance. Left) C', Right) C'' components of complex capacitance.....	171
Figure 106-Appendix: Impedance characterization of Bulk BiMn ₂ O ₅ Electrode (Milling to 1.28 μm). Top) Nyquist plots of complex impedance. Left) C', Right) C'' components of complex capacitance.	172
Figure 107-Appendix: Impedance characterization of Bulk BiMn ₂ O ₅ Electrode (Milling to 0.23 μm). Top) Nyquist plots of complex impedance. Left) C', Right) C'' components of complex capacitance.	173
Figure 108-Appendix: Impedance characterization of Thin Film BiMn ₂ O ₅ Electrode (Sedimentation separated to 1.00 μm). Top) Nyquist plots of complex impedance. Left) C', Right) C'' components of complex capacitance.....	174
Figure 109-Appendix: XRD Pattern for Sodium (ICSD: 44757), Silicon (ICSD: 51688), NaSi (ICSD: 409953), and Na ₄ Si ₂₃ (ICSD; 50796), used in NaSi powder characterization.	175
Figure 110-Appendix: XRD Pattern for FeSi (ICSD: 402781), Fe ₃ Si (ICSD: 412838), CrSi ₂ (ICSD: 96026), Na _{2.85} Si ₁₇ (ICSD: 248167), Na ₂ SiO ₃ (ICSD: 15388), and ZrO ₂ (ICSD: 85322) used in NaSi powder characterization.....	176

Figure 111-Appendix: XRD Pattern for Mn_2O_3 (ICSD: 159865), Bi_2O_3 (ICSD: 15072), and $BiMn_2O_5$ (ICSD; 169734), used in BMO powder characterization. 177

List of Tables

Table 1: Abundance of Elements commonly found in Lithium and Sodium Based Batteries [4].....	2
Table 2: Theoretical and practical specific energies of common secondary batteries [5] ..	3
Table 3: Ionic conductivity of β - and β'' -Alumina.....	8
Table 4: Changes in conductivity and activation energy due to ion exchange in β and β'' [9]	10
Table 5: List of Materials used in this work.....	43
Table 6: Composition by weight % of Glass Seals	51
Table 7: Terminal Velocities of Different Particles in Slip Casting Slurries.....	71
Table 8: Lines of Fit for BASE tube conductivity tests	76
Table 9: Bulk & Interfacial conductivities of solid BASE tubes	77
Table 10: Calculated interfacial resistance (χ) of Duplex BASE tubes using bulk resistance calculated by dense BASE tubes.	79
Table 11: Conductivity of NaSi	85
Table 12: Conductivity measurements of NaSi using chunks at room temperature	87
Table 13: Autoclave sample parameters	101
Table 14: Thermodynamic Properties of Na-Si phases.....	119
Table 15: $BiMn_2O_5$ Xerogel Synthesis Method	123
Table 16: Result of Calcination of $BiMn_2O_5$ Xerogel.....	124
Table 17: Stability of EPD Solution for Li^+ anode and cathode materials.....	137

List of Abbreviations and Symbols

Abbreviations

<i>BASE</i>	<i>β-Alumina Solid Electrolyte</i>
<i>BMO</i>	<i>Bismuth Manganese Oxide (BiMn₂O₅)</i>
<i>CMC</i>	<i>Carboxymethyl Cellulose, sodium salt</i>
<i>CNT</i>	<i>Carbon Nanotube</i>
<i>CTE</i>	<i>Coefficient of Thermal Expansion</i>
<i>CV</i>	<i>Cyclic Voltammetry</i>
<i>DSC</i>	<i>Differential Scanning Calorimetry</i>
<i>DTA</i>	<i>Differential Thermal Analysis</i>
<i>ECC</i>	<i>Electrochemical Capacitor</i>
<i>EDLC</i>	<i>Electrochemical Double Layer Capacitor</i>
<i>EES</i>	<i>Electrochemical Energy Storage</i>
<i>EIS</i>	<i>Electrochemical Impedance Spectroscopy</i>
<i>EMF</i>	<i>Electromotive Force</i>
<i>EPD</i>	<i>Electrophoretic Deposition</i>
<i>FTIR</i>	<i>Fourier-Transform Infrared Spectroscopy</i>
<i>HDPE</i>	<i>High Density Polyethylene</i>
<i>LFPO</i>	<i>Lithium Iron Phosphate (LiFePO₄)</i>
<i>LMO</i>	<i>Lithium Manganese Spinel (LiMn₂O₄)</i>
<i>LMNO</i>	<i>Lithium Manganese Nickel Spinel (1.5Ni_{0.5}O₄)</i>
<i>LTO</i>	<i>Lithium Titanate (Li₄Ti₅O₁₂)</i>
<i>PAZO</i>	<i>Poly[1-[4-(3-carboxy-4-hydroxyphenylazo)benzenesulfonamido]-1,2-ethanediyl, sodium salt]</i>
<i>PEEK</i>	<i>Poly(aryl-ether-ketone)</i>

<i>PEM</i>	<i>Proton-exchange membrane Polymer electrolyte membrane (In relation to Fuel Cells)</i>
<i>PMMA</i>	<i>Poly(methyl methacrylate)</i>
<i>PVB</i>	<i>Polyvinyl Butyral</i>
<i>SCE</i>	<i>Standard Calomel Electrode</i>
<i>SEM</i>	<i>Scanning Electron Microscopy</i>
<i>TGA</i>	<i>Thermogravimetric Analysis</i>
<i>YSZ</i>	<i>Yttria Stabilized Zirconia</i>
<i>w.r.t.</i>	<i>“With Respect To”</i>
<i>ZEBRA</i>	<i>Original name for Ni-Metal Chloride cells: “Zeolite Battery Research Africa” Renamed: “Zero Emissions Batteries Research Activity”</i>

Symbols

α	<i>Alpha, in relation to phase</i>
β	<i>Beta, in relation to phase</i>
ϵ_0	<i>Permittivity of vacuum ($8.85 \times 10^{-12} \text{ F m}^{-1}$)</i>
ϵ or ϵ_r	<i>Relative Permittivity of Dielectric</i>
σ	<i>Conductivity (S cm^{-1})</i>
η	<i>Viscosity ($\text{kg m}^{-1} \text{ s}^{-1}$)</i>
χ	<i>Interfacial Ionic Resistance ($\Omega \text{ cm}^2$)</i>
ζ	<i>Zeta-potential</i>
ρ_S or ρ_L	<i>Density of Particle or Liquid (kg m^{-3})</i>
A	<i>Area (cm^2)</i>
C	<i>Capacitance (Farad, F)</i>
d	<i>Diameter (m)</i>

E_a	<i>Activation Energy (eV)</i>
E_{cell}	<i>Electromotive Force (V)</i>
F	<i>Faraday Constant (96485 C mol⁻¹)</i>
g	<i>Force of Gravity (9.81 m s⁻²)</i>
k	<i>Boltzmann constant (1.3805x10⁻²³ m² kg s⁻² K⁻¹)</i>
L	<i>Length (m)</i>
m	<i>Mass (kg)</i>
Me	<i>Metal or Metal Ion</i>
N_R	<i>Reynolds number</i>
Q	<i>Charge</i>
r	<i>Radius (m)</i>
R	<i>Resistance (ohm, Ω)</i> <i>Gas Constant (8.314 J mol⁻¹ K⁻¹)</i>
S	<i>Slope Coefficient</i>
t	<i>Time (s)</i>
T	<i>Temperature (°C or K)</i>
v	<i>Velocity (m s⁻¹)</i>
v_s	<i>Settling Velocity (m s⁻¹)</i>
V	<i>Voltage (V)</i>

Declaration of Academic Achievement

This dissertation was used to fulfill the requirements of Ph.D. degree. The work falls under four projects: Duplex Electrolyte Characterization, NaSi Characterization, Electrophoretic Deposition of Lithium Ion Battery Materials, and Synthesis of BiMn₂O₅ Supercapacitor. The entirety of the duplex electrolyte characterization project was completed between January 2013 and January 2017. The majority of the NaSi project was completed between January 2017 and December 2018. The majority of the lithium ion and BiMn₂O₅ projects were completed between October 2017 and December 2018.

The work presented in this dissertation includes the contributions of Dr Simon Joshi and Dr Kaiyuan Shi. Dr Joshi contributed to the NaSi project by designing the high temperature four-probe conductivity experiment and gathering a portion of the conductivity values. Dr Shi contributed to the lithium ion battery materials project by testing the electrochemical performance of the coin cells at the National Research Council of Canada.

The duplex electrolyte characterization and NaSi characterization projects were used to submit industry reports to their respective sponsors. The lithium ion battery projects resulted in two papers, yet to be published.

1. **Michaud, X.**, Petric, A. “Fundamental Study of a Duplex β ’-Alumina Electrolyte,” *Industry Report*, McMaster University, Hamilton, 2013.
2. **Michaud, X.**, Joshi, S., Petric, A. “Characterization of the NaSi phase,” *Industry Report*, McMaster University, Hamilton, 2017.
3. **Michaud, X.**, Shi, K., Zhitomirsky, I. “Electrophoretic deposition of LiFePO_4 for Li-ion batteries,” *Materials Letters*, vol. 241, pp. 10-13, 2019.
4. **Michaud, X.**, Shi, K., Zhitomirsky, I. “Topic on the electrophoretic deposition of LiMn_2O_4 and $\text{LiMn}_{1.5}\text{Ni}_{0.5}\text{O}_4$ for Li-ion batteries,” *Unpublished*.

Additional contributions to peer reviewed work, not presented in this thesis, include the following publication:

1. Liu, Y., Luo, D., Shi, K., **Michaud, X.**, Zhitomirsky, I. “Asymmetric supercapacitor based on MnO_2 and Fe_2O_3 nanotube active materials and graphene current collectors,” *Nano-Structures & Nano-Objects*, vol. 15, pp. 98-106, 2018.

Chapter 1: Introduction

The energy demand across the globe has been continuously growing at a rate around 2% per year [1]. While most of this growth is accommodated by a broad range of fuel sources, renewable energy had the highest growth between 2016 and 2017, nearly 17% [1]. Renewable energy sources include hydroelectric power, biomass, and geothermal energy, but the most well known technologies are wind and solar power. One of the most recognized problems with renewable energy is its intermittent nature. The demand for power may not be satisfied during energy production down time. Electrochemical energy storage [EES] installations have been used for load levelling. There are other applications for EES, most commonly portable electrical devices and electrical elements.

There are several EES types which are classified as batteries, supercapacitors and fuel cells. Each of these has found various levels of success, but the biggest market is for batteries. Currently, lithium ion batteries are receiving tremendous attention, due to their overwhelming properties. However, the most commercialized lithium ion battery, $\text{LiC}_6/\text{LiCoO}_2$, makes use of scarce cobalt and lithium. Of course, other lithium ion batteries use other transition metals. Alternatively, batteries using other more abundant alkali metals like sodium or potassium have found success. Although sodium ion batteries have been the focus of recent study [2], liquid sodium metal batteries have been successfully commercialized [3]. Table 1 shows the percent abundance of commonly used elements found in the Earth's crust. Even though lithium ion batteries have better

performance, sodium based batteries can accommodate more of the energy storage demand simply by virtue of its abundance.

Table 1: Abundance of Elements commonly found in Lithium and Sodium Based Batteries [4]

Element	Abundance (%)	Battery Type
Lithium	1.8×10^{-3}	Li-B
Cobalt	2.9×10^{-3}	Li-B
Manganese	0.11	Li-B
Nickel	9.9×10^{-3}	Li-B, Na-B
Chlorine	1.24×10^{-2}	Na-B
Sulfur	3.40×10^{-2}	Na-B
Sodium	2.27	Na-B

However due to chemistry, as well as practical construction requirements, different battery systems will have their own theoretical and practical specific energies. Table 2 shows the different theoretical and practical specific energies of common rechargeable battery systems, as well as some systems currently being researched. These values can be compared to other EES systems and combustion engines. Theoretically, the specific energy of gasoline is approximately $13,000 \text{ Wh kg}^{-1}$, while compressed or liquid hydrogen for fuel cells have a whopping $40,000 \text{ Wh kg}^{-1}$.

The primary goal of this work is to find new production, testing, and synthesis of components used in sodium metal and lithium ion batteries, as well as other EES devices. Duplex structured sodium β -alumina solid electrolytes were produced to test the reduction of interfacial resistance in molten sodium metal batteries. Polymer-assisted electrophoretic depositions of Li-ion battery anode and cathode oxides were successful in producing stable electrodes. The synthesis of bismuth manganese oxide was done through sol-gel precipitation, and tested as a possible pseudocapacitive material. Additionally, the

sodium-silicon binary system has increased in interest due to the possible use of silicon in sodium or lithium battery anodes. A study of the system and the NaSi phase was undertaken.

Table 2: Theoretical and practical specific energies of common secondary batteries [5]

System	Anode	Cathode	Th. Sp. En. (Wh kg ⁻¹)	Pr. Sp. En. (Wh kg ⁻¹)
Lead-Acid	Pb	PbO ₂	171	20 – 40
Ni-Cd	Cd	NiOOH	219	20 – 40
Ni-MeH	MeH-alloy	NiOOH	~240	50 – 70
Na-S (≥300°C)	Na	S	754	~120
Na-MeCl ₂ (≥300°C)	Na	MeCl ₂ (Me=Ni,Fe,Cu)	787	~90
Li-ion	Li _x C ₆	Li _{1-x} CoO ₂	584	100 – 150
	Li _x C ₆	Li _{1-x} Mn ₂ O ₄	424	80 – 100
	Li _x C ₆	Li _{1-x} FePO ₄	398	80 – 100
	Li ₄ Ti ₅ O ₁₂	Li _{1-x} Mn ₂ O ₄	200	50 – 70
	Li _x C ₆	Li _{1-x} Mn _{1.5} Ni _{0.5} O ₄	493	—
Li-S	Li	S	~1168	—
Li-O ₂	Li	O ₂	1752-2691	—

Chapter 2: Literature Review

High Temperature Molten Sodium-Anode Batteries

Molten sodium-anode batteries are made possible by the use of solid electrolytes which act both as separator and ionic conductor. Sodium beta-alumina, first discovered in the early 1900s, received little attention until 1967, when Yao and Kummer showed rapid ionic diffusion in beta-alumina at elevated temperatures [6]. Interest in this phenomenon, spurred on by the possible applications in batteries, is seen as the origin of a new branch of science known as solid state ionics.

Two primary battery architectures exist; sodium sulfur, and sodium metal-halide. The sodium sulfur cell was first proposed in 1967 [7], while the sodium metal-halide cell was later introduced in 1978 as an alternative [8]. Significant research surrounding both of these battery types was performed until the early 1990s, when the demand for energy storage became less pressing. However, in recent years, a resurgence of interest in these systems has been seen across the globe.

Beta-Alumina Solid Electrolyte [BASE]

The β -alumina solid electrolyte refers not to a single compound, but rather a group of oxides which are characterized by their structure. These structures are alternating spinel blocks and conduction planes or slabs. The conduction planes are loosely-packed layers with mobile sodium ions. The sodium ions are free to move along the a-axis, but not the c-axis, when subjected to an electrical field. The oxygen in the conduction planes bond

the spinel blocks together, as these are immobile. The spinel blocks are formed from four (or more) layers of close-packed oxygen, with the aluminium ions found in both the octahedral and tetrahedral sites. Generally, the β -alumina phases referenced are the β - and β'' -alumina structures, albeit others exist under different circumstances. The differences in structure between β - and β'' -alumina are illustrated in Figure 1. One of the most prominent differences between β - and β'' is the number of conduction planes within the unit cell. β has one conduction plane between two spinel blocks, while β'' has two conduction slabs within three spinel blocks. In β the sodium ions lie directly on the same plane as the connecting oxygen ions. Due to the two-fold screw axis observed in β , the conduction plane acts as a mirror plane for the spinel blocks. In β'' however, no such mirror plane exists. Additionally, the sodium ions do not lie on the same plane as the linking oxygen ions, but rather slightly above and below.

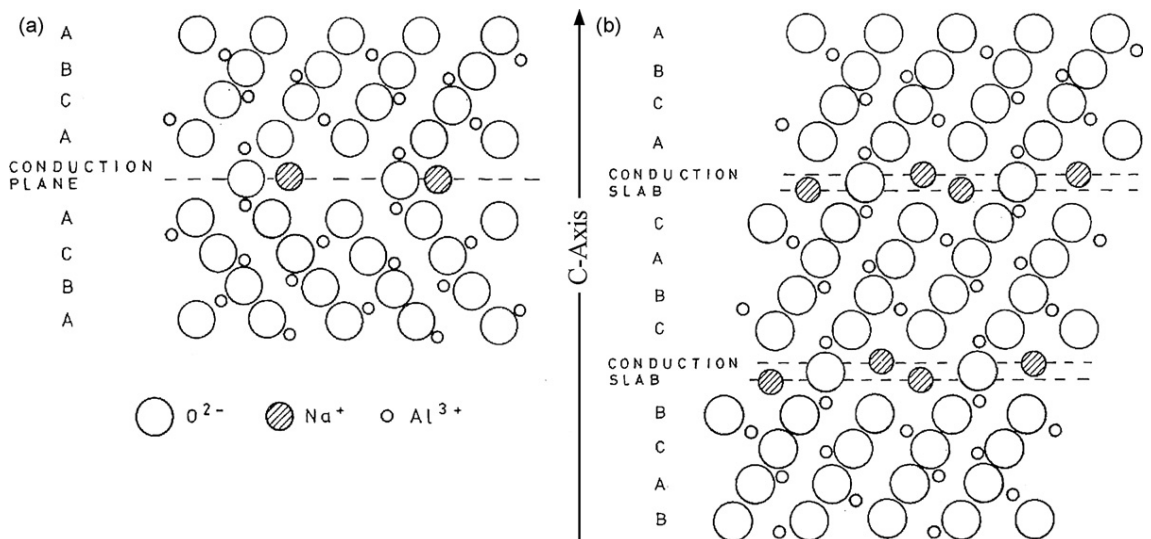


Figure 1: Idealized structures of Beta & Beta'' (Reproduced from [9])

β -Alumina has a hexagonal structure (P63/mmc) with a c-axis length of 22.61 Å, while β'' -alumina is rhombohedral (R3m) with a c-axis of 33.95 Å. The a-axis lengths are 5.59 Å for the former and 5.60 Å for the latter. The structures presented in Figure 1 are the idealized structures of β and β'' . The β structure presented has a stoichiometric formula of $(\text{Na}_2\text{O})_{1+x} \cdot 11\text{Al}_2\text{O}_3$, where $x = 0$. However, an excess amount of Na_2O is generally found in practice. This excess is usually between $x = 0.25$ and $x = 0.55$, but can be increased using dopant stabilizers. The idealized structure of β'' has a stoichiometric formula of $\text{Na}_6\text{Al}_{32}[\text{Vac}]_{\text{Al}^{3+}}\text{O}_{51}$. The idealized structure is not accommodated in the structure, and therefore must be stabilized using substitutions of the $[\text{Vac}]_{\text{Al}^{3+}}$. These substitutions must have a valence of +1 or +2.

Ionic Conductivity in BASE

The β -alumina group is especially interesting because of their high ionic conductivity. Ionic conductivity of β'' -alumina is higher than that of β -alumina. Single crystals of β'' -alumina have been shown to have ionic conductivities of 1 S cm^{-1} , while remaining electronically insulating. This high conductivity rivals the ionic conductivities of aqueous electrolytes at their respective working temperatures. However, unlike liquid electrolytes, many factors affect the conductivity of the BASE. The composition and microstructure of the BASE are the two primary factors.

The composition can be broken down into two components: the ratio of β and β'' present, and the concentration of stabilized sodium in their conduction plane. Figure 2 shows the decrease in resistance of samples with higher portions of β'' . It can be inferred that pure

β'' would be ideal. However, some issues with manufacturing and stability arise. In practice, a mixture of β and β'' is utilized. Finally, certain additives and impurities can negatively affect the conductivity of the BASE.

One such proposed additive is yttria-stabilized zirconia [YSZ]. YSZ was found to significantly improve the sinterability of β -alumina, as well as increase its mechanical strength by close to a factor of two [10]. However, this strengthening can come at the cost of decreased ionic conductivity, when doped above a certain threshold. Common impurities, like calcia and silica, offer no mechanical property improvement, but instead block the movement of sodium ions by forming secondary phases like calcium aluminate and sodium aluminosilicate glasses, thereby decreasing ionic conductivity.

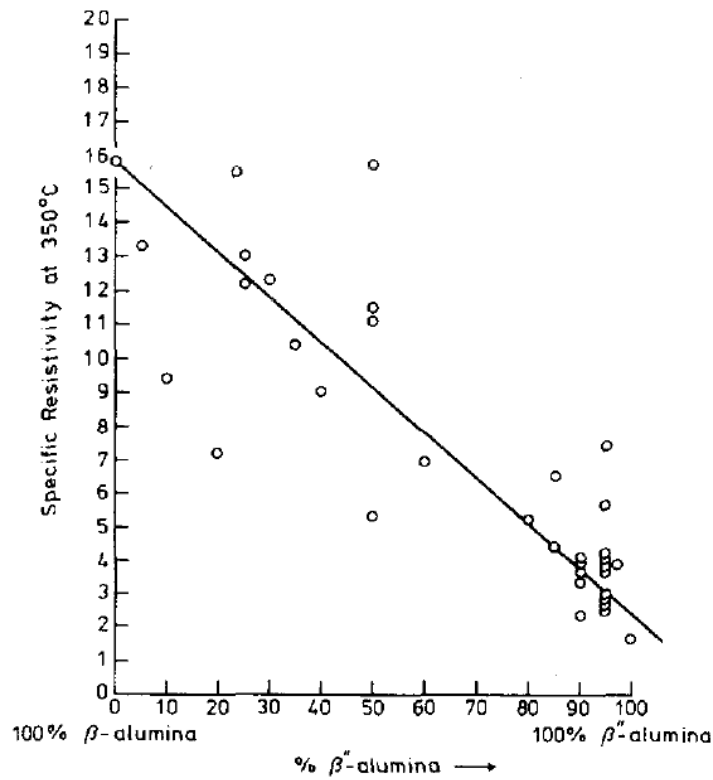


Figure 2: Effects of Mixed β/β'' on Resistivity [7].

Table 3 shows the ionic conductivity of single crystal and polycrystalline β and β'' . The ionic conductivity in single crystals is measured perpendicular to the c-axis of the crystal structure. It can be seen that the conductivity of single crystals is two to five times that of their polycrystalline analogues. AC spectroscopy measurements have shown that the increase in resistivity was primarily due to grain boundary resistances. As such, increasing the grain sizes of the BASE improve the conductivity. Large grains in β -alumina reduce its mechanical properties. Therefore, a balance between grain size and conductivity must be kept. Another microstructure aspect that affects conductivity is preferred orientation. Since the c-axis is non-conductive, the amount of grains with their c-axis pointed in the direction of the electric field will negatively affect the conductivity of a polycrystalline BASE [11].

Table 3: Ionic conductivity of β - and β'' -Alumina

Phase	$\sigma_{300^\circ\text{C}}$ (S cm ⁻¹)	E_a (eV)
Single Crystal β	0.21 – 0.27	0.13 – 0.17
Polycrystalline β	0.06 – 0.08	0.15 (>200°C)
Single Crystal β''	~1.0	~0.1 (>150°C)
Polycrystalline β''	0.2-0.4	0.15 – 0.26

The conductivity in BASE is a thermally activated process which follows Arrhenius law, as shown in Equation 2.1,

$$\sigma T = \sigma_0 e^{\left(\frac{-E_a}{kT}\right)} \quad \text{Eq 2.1}$$

where E_a is the activation energy to diffusion, k is the Boltzmann constant, and T is the absolute temperature. The values for σ_0 and E_a are determined from the plot of $\log \sigma T$ vs

1/T. Figure 3 shows the Arrhenius plot for both β and β'' . While β shows a linear dependence β'' has a shift in its slope. This is indicative of a change in two-dimensional ordering which affects the conduction mechanism.

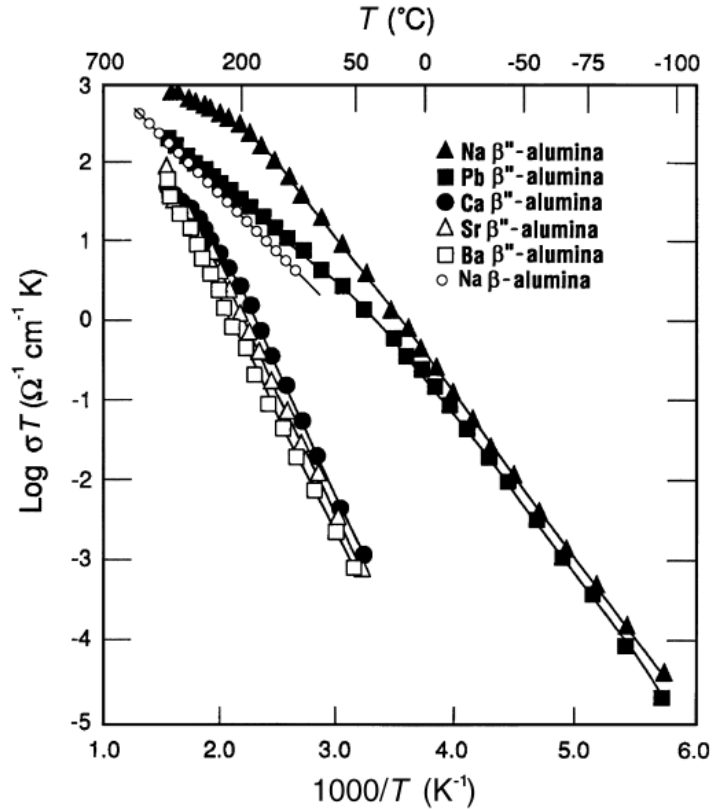
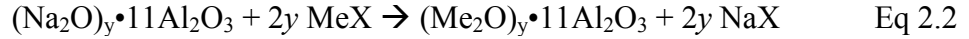


Figure 3: Arrhenius Plot of Conductivities of β and β'' [12]

Ion Exchange in BASE

One interesting “side effect” of the high sodium ion mobility is that ions can be exchanged without significant stresses to the overall crystal structure. The predominant method of exchanging sodium ions with a new cation is by ion exchange in molten salt baths. Here, the β powders, or crystals, are submerged in the molten salt. Equation 2.2 shows the conceptual equation for the process,



where MX is the metal halide that will replace the sodium ion. This process can be accelerated by using the BASE as an electrochemical cell. A wide range of cations have been exchanged using different methods. Figure 4 shows the original work by Yao and Kummer which started the intensive interest in solid state ionics. The amount of exchange is controlled by the amount of sodium halide exchanged into the bath. Therefore, to fully exchange the sodium ions with the new cations, a multi-bath process needs to be completed. The rate of exchange is dependent on the ionic mobility of the system. The exchange causes slight changes to the crystal structure, due to the difference in ionic radius, but also affects the conductivity and activation energy, as seen in Table 4.

Table 4: Changes in conductivity and activation energy due to ion exchange in β and β'' [9]

Cation (Radius)	β -Alumina		β'' -Alumina	
	Ea (eV)	σ_{RT} (S cm ⁻¹)	Ea (eV)	σ_{RT} (S cm ⁻¹)
Na ⁺ (0.97Å)	0.15	358	0.33	250
Li ⁺ (0.60Å)	0.24	30	0.30	50
K ⁺ (1.33Å)	0.28	1.6	0.15	1000
Ag ⁺ (1.26Å)	0.16	130	0.19	40
Rb ⁺ (1.47Å)	0.39	0.12	—	—

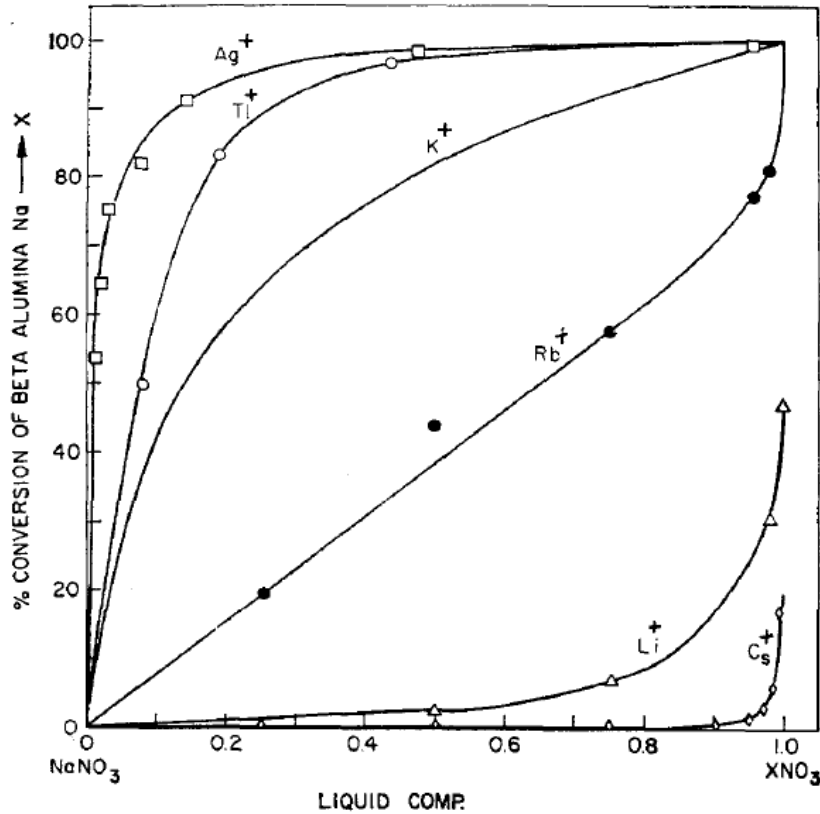


Figure 4: Ion exchange in BASE using molten metal nitrate bath [6].

BASE Synthesis & Production

There is a wide range of synthesis methods used to produce BASE. Some of the more conventional methods include solid state reactions [13], sol-gel [14, 15], and co-precipitation techniques. Other methods like flame spray pyrolysis of polymeric precursors [16] and freeze drying [17, 18] have been successful.

In solid state reactions, mixtures of α -alumina, sodium oxide precursor, and magnesium or lithium oxide precursors are ball milled and then fired at high temperatures. This generally produces a mixture of β and β'' , but also can cause the formation of NaAlO₂ due to β'' dissociation or loss of sodium will move the composition towards β -alumina or

Al_2O_3 . This NaAlO_2 increases resistance and increases the sensitivity of the BASE to humidity.

In wet chemical methods, like sol-gel and co-precipitation, precursors are dissolved and complexed with various agents. The primary benefits of wet chemical methods are increased homogeneity and purity in the final product. Depending on the process parameters, ultra fine particles [19], or large aspect ratio fibers [20] can be produced. Powders made through wet chemical methods are generally ready to use, reducing the amount of impurities introduced due to mechanical processing.

Depending on the cell design, the powders will be formed in either a disk or closed-end tube. There are many methods of producing these parts which include isostatic pressing, electrophoretic deposition, slip casting and extrusion. In both slip casting and electrophoretic deposition, the powder must be suspended in a solution. Not only do the suspension medium and any additives need to be compatible with the powders, the powders must be in a form that allow for a stable suspension to form. The similarities end there, however. In electrophoretic deposition, two electrodes are dipped into the solution. A field is applied between the counter electrode, and the working electrode (mandrel). The powders in suspension move towards the mandrel and deposit. Once the deposit reaches the desired thickness, the mandrel is removed and the part is slipped off. In slip casting, on the other hand, the suspension is poured into a mould which absorbs the suspension medium, forming the part on the inside of the mould walls. The suspension is poured out once the cast reaches the desired thickness. These methods both have the benefit of forming near-shape parts, but can be time consuming. Isostatic pressing, on the

other hand, is much more rapid while maintaining good dimensional tolerances. Raw powders are filled into a die made of a material like rubber, which is then sealed. The mould is then compacted hydraulically, which presses the powders into the wanted form.

Once formed, the BASE parts are sintered to a dense state. The sintering process depends on the many parameters including the feed powder chemistry and part production methods. However, negative effects of sintering must be taken into account. At elevated temperatures, soda loss can cause conversion of β , but also cause cracking. This can be prevented by encapsulating the part in β buffer, sealing it in magnesia or platinum crucibles, or by flash and zone sintering [21]. Sintering control is also important, as β forms a microstructure of large grains (up to 500 μm) in a matrix of fine grains. Undersintering the BASE parts may cause excessive porosity, which can manifest as higher resistances, decreased strength, and potential leakage.

Sodium Sulfur Cell

The first cell proposed was the sodium sulfur cell. Interest in these batteries comes from their energy densities (760 Wh kg^{-1}), abundance of both anode and cathode materials, and ease of fabrication. The design of the Na-S cell is shown in Figure 5. The anode (molten sodium) is separated from the cathode (molten sulfur) by the BASE tube. A carbon felt is placed within the tube to assist the wetting of sodium along the BASE and also acts as the current collector. The cell operates between 270°C and 350°C since the cathode must remain molten. The half- and full-cell reactions are outlined in Equations 2.3-2.5.

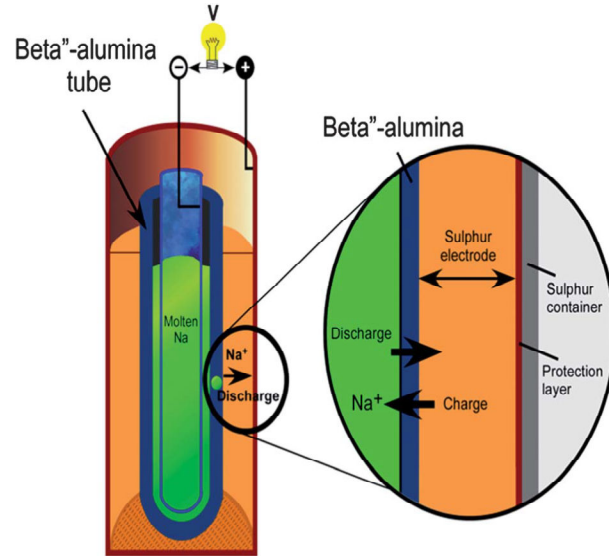


Figure 5: Na-S Battery Architecture [22]



The full cell reaction exhibits a range of equilibrium voltages. This is due to the fact that the Na_2S_x product (sodium polysulphide) is in liquid state, existing in a number of phases. Figure 6 shows the voltage profile during the discharging of a Na-S cell. When fully charged excess sulfur and Na_2S_5 coexist in an immiscible two phase region, giving a voltage plateau. As the cell discharges, the sulfur is consumed, and the cathode turns into a single phase liquid. By discharging beyond the liquidus boundary, the cell will enter the

two-phase region of liquid and Na_2S_2 , which gives a constant voltage. At this point, the operation of the cell is limited due to the solid Na_2S_2 .

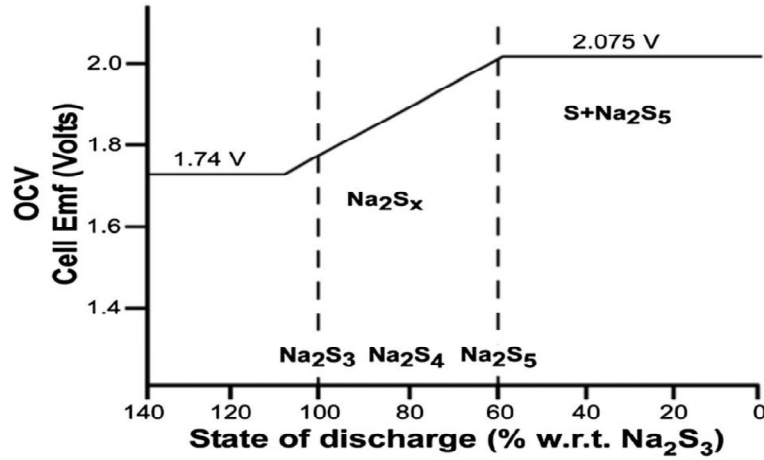


Figure 6: Voltage Profile during discharge of Na-S cell [22].

Figure 7 is the Na-S phase diagram in the sulfur-rich region. The blue arrow shows the path of composition change in the Na-S liquid as the cell is discharged. It can easily be seen that once the composition surpasses approximately 35% sodium by mole, the two phase Na_2S_2 -liquid region is stable, negatively affecting the cell.

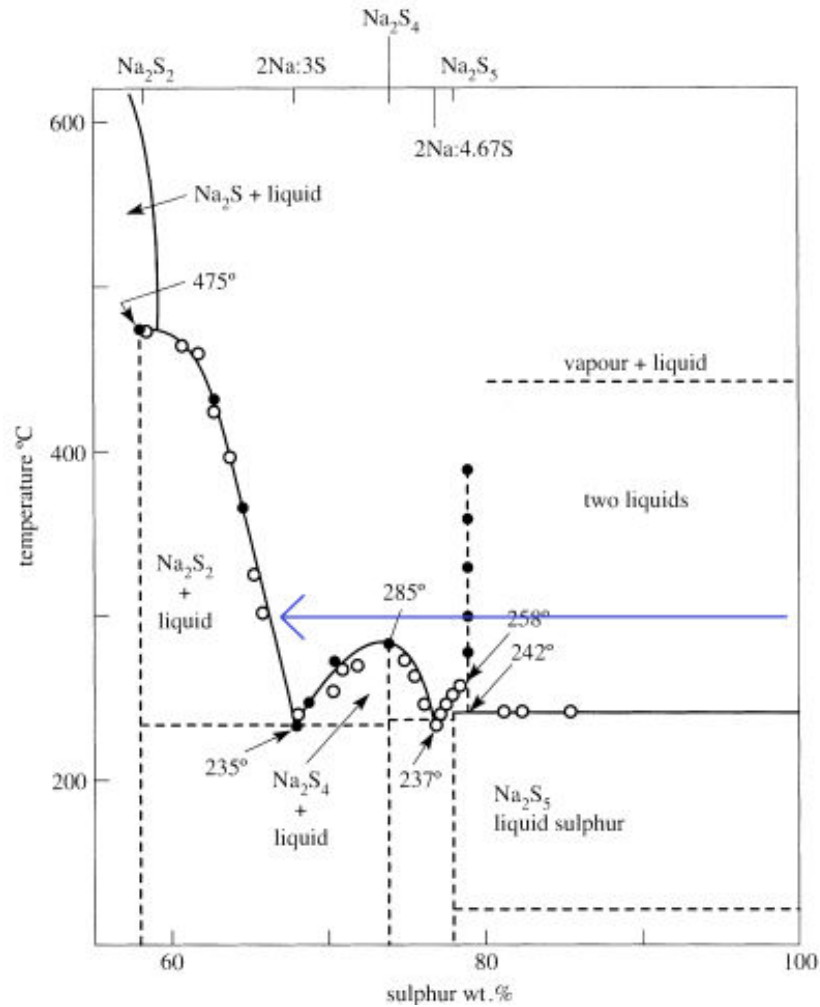
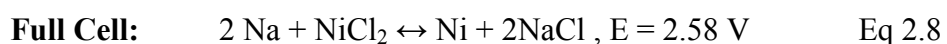
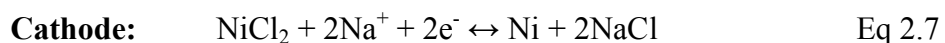
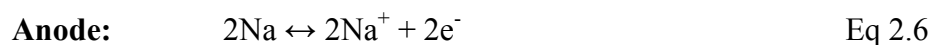


Figure 7: Na-S Binary Phase Diagram [23].

There are a few drawbacks to the Na-S battery, one of which is safety. At the elevated temperatures used in their operation, the sodium, sulfur and sodium polysulphides are all rather corrosive. The cells must be designed to withstand their effects so as to not fail. Additionally, the ceramic BASE must not crack, as the uncontrolled reaction between sodium and sulfur can be violent.

Sodium Metal Halide Cell

The sodium metal halide cell type is an alternative to the sodium sulfur cell. The first to be proposed was the ZEBRA cell which used NiCl_2 as the cathode. These cells generally operated between 300°C and 350°C . However, other metal chlorides have successfully been used. The ZEBRA cell has a similar architecture (Figure 8) to the Na-S cell, with the exception of a secondary liquid electrolyte that is added on the cathode side of the BASE. Equations 2.6 to 2.8 show the half- and full-cell reactions that occur during normal charging and discharging.



One of the more significant differences between the Na-S and ZEBRA battery is that the higher voltage of the ZEBRA cell remains constant within normal operation. During cell overcharging and overdischarging, the secondary electrolyte will accommodate the excesses, although it is not its primary purpose. The reactions are shown in Figure 9.

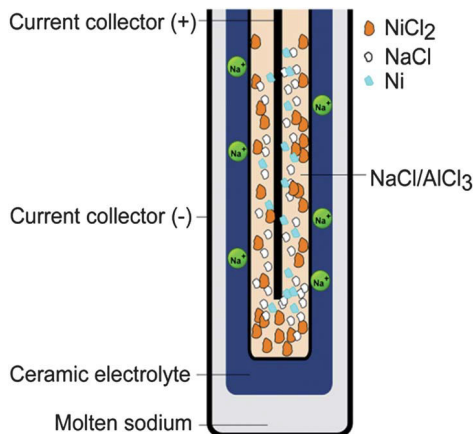


Figure 8: Na-NiCl₂ cell architecture with secondary electrolyte [22]

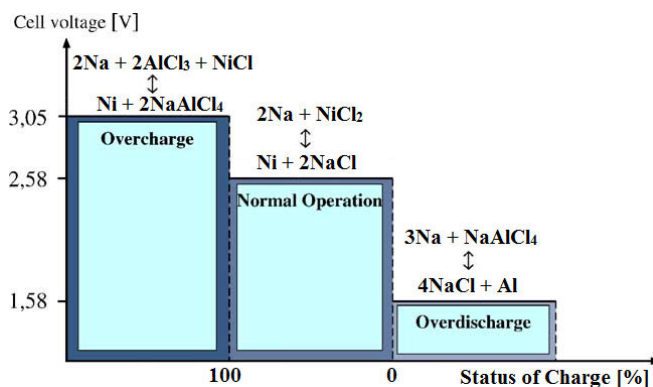


Figure 9: Na-NiCl₂ cell voltage profile during charge & discharge (Modified from [24])

The secondary electrolyte (NaAlCl₄) is added to the cell to enhance the battery kinetics, as it is a sodium ion conductor. Since most of the cathode is solid (NaCl, NiCl₂, Ni) during normal operation, sodium ion movement through the cathode material is inherently slow if NaAlCl₄ is excluded. However, NaAlCl₄ (m.p. 157°C) must remain in the molten state to be a rapid ion conductor.

As previously noted, other metal halide systems are possible. Figure 10 shows the open circuit voltages of various sodium metal chloride cells. Iron chloride is an effective alternative to nickel as it is more abundant [25]. Sodium-copper chloride [26, 27] and sodium-zinc chloride [28] cells have been successfully demonstrated. Doping of the cathode with other metal halides, and metal sulfides, has shown improvements in cell performance [29, 30, 31]. Lu et al. showed in 2013 that hybrid cells of NiCl₂ and sulfur cathodes show an improvement over the individual counterparts.

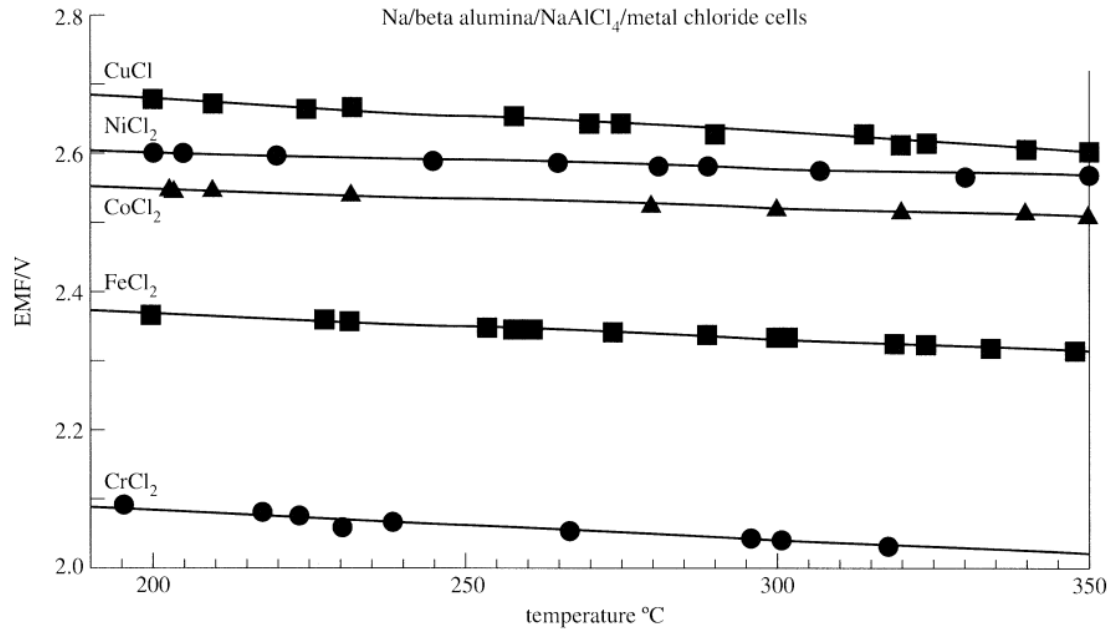


Figure 10: Open circuit voltages of various sodium metal chloride cells [23].

The ZEBRA cell is significantly safer than the Na-S cell. Even though both require the use of molten sodium metal anodes, the ZEBRA cell can be constructed in the discharged state ($\text{Ni} + \text{NaCl} + \text{NaAlCl}_4$). Additionally, during normal and taxed operation, the cell does not produce gaseous phases, preventing catastrophic failure. In the case that the BASE fails, the direct reaction between sodium and nickel chloride is much less aggressive. Additionally, since the product of the reaction is nickel metal, and potentially aluminium if the secondary electrolyte also reacts, the cell is still highly conductive. This means that a cell in a series would not significantly increase the resistance of the battery, which prevents overheating.

Planar Cells

Traditionally, sodium metal batteries used a tube or clover-shaped solid electrolyte. These cells are stable and simple to produce through various methods. However, one of the predominant drawbacks of these cells is that a significant amount of excess sodium is needed, reducing the power density of the batteries. Planar cells have been discussed since the early development of the batteries [9, 32] and are actively being pursued to this day [33, 34, 35, 36, 37]. The planar cells have the same general chemistry; however their architecture differs, as seen in Figure 11.

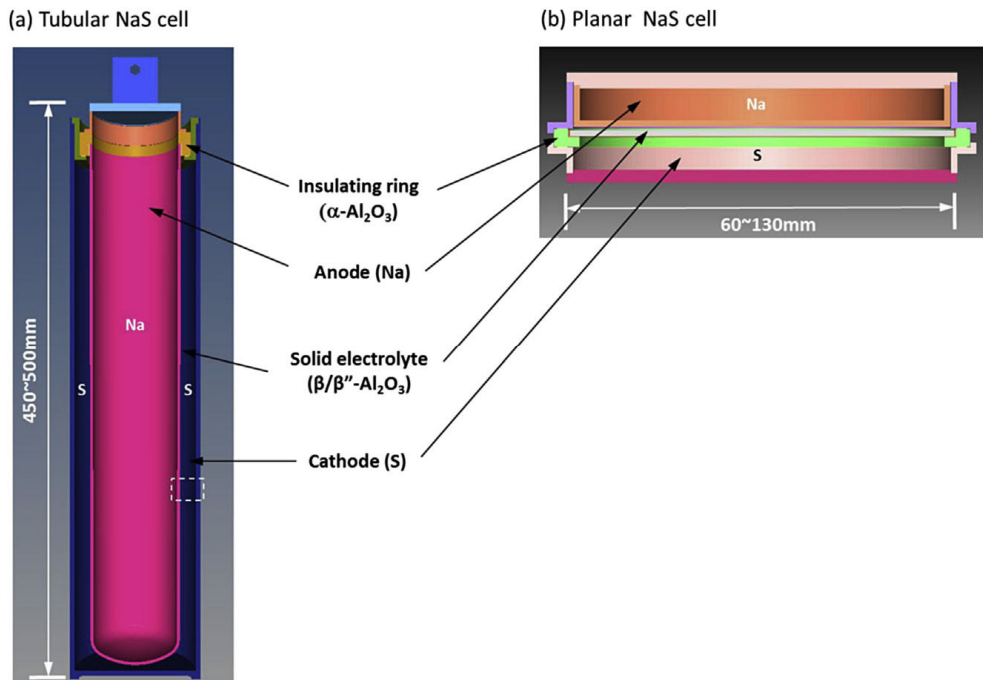


Figure 11: Similarities and differences between tubular (tradition) and planar (advanced) NaS cells [37].

There are many advantages and drawbacks to the planar design. Planar cells would allow their stacking, which in turn would increase the power density and temperature control. They could potentially decrease the cost of production due to reduced excesses. However, some of the difficulties with planar cells have prevented their use, until recently.

Two of the difficulties with the planar design are the structural integrity of the BASE disk during cycling [38], and preventing the disconnection of the anodes or cathodes from the BASE and current collectors. The latter has been investigated by including carbon felts at the anodes [37] or nickel meshes at the cathodes [33, 36]. The physical properties of the BASE disks have been improved by the use of a duplex BASE consisting of a thin dense layer and a porous substrate [39, 40]. The duplex structure has the added effect of improving the area specific resistance when compared to smooth planar electrolytes [39]. Another consideration is that the length of the joint connecting the BASE to the cell increases significantly. This makes the likelihood of seal failure much more prominent. The possibility of clamping the BASE between polymeric O-rings in an attempt to seal the cells, rather than using glass sealants, has been studied [34]. However, polymeric O-rings would require lowered working temperatures. This can be achieved by alloying sodium with other alkali metals [41], or moving to potassium based cells [42].

Lithium Ion Batteries

Lithium ion batteries have received widespread attention in the energy storage research community since the development of the first Li-ion intercalation materials. Applications of lithium ion batteries are far reaching, touching all aspects of modern society. However, like any electrochemical energy storage, it has its benefits and drawbacks. Their intensive use of lithium and scarce transition metals, primarily cobalt, has made the possibility that material shortages, or spikes in prices, may occur as demand increases. That said, the advantages provided by lithium ion batteries over other systems cannot be ignored. Lithium ion batteries have high gravimetric and volumetric capacities and power densities. This is primarily due to the chemistry of lithium. Lithium is the third lightest element, has a small ionic radius, and the highest cell potential.

Figure 12 shows the typical operation of a Li-ion battery using intercalation materials as both the anode and cathode. Although most commercialized batteries utilize intercalation materials, other anode and cathode materials exist. The electrolyte of lithium ion batteries can be a liquid, gel, or ionic polymer. The most common electrolytes are mixtures of lithium salts dissolved in organic alkyl carbonate solvents. Aqueous electrolytes are generally incompatible with one or both of the electrodes. Taking the example in Figure 12, the reactions in the cell are given in Equations 2.9 to 2.11.

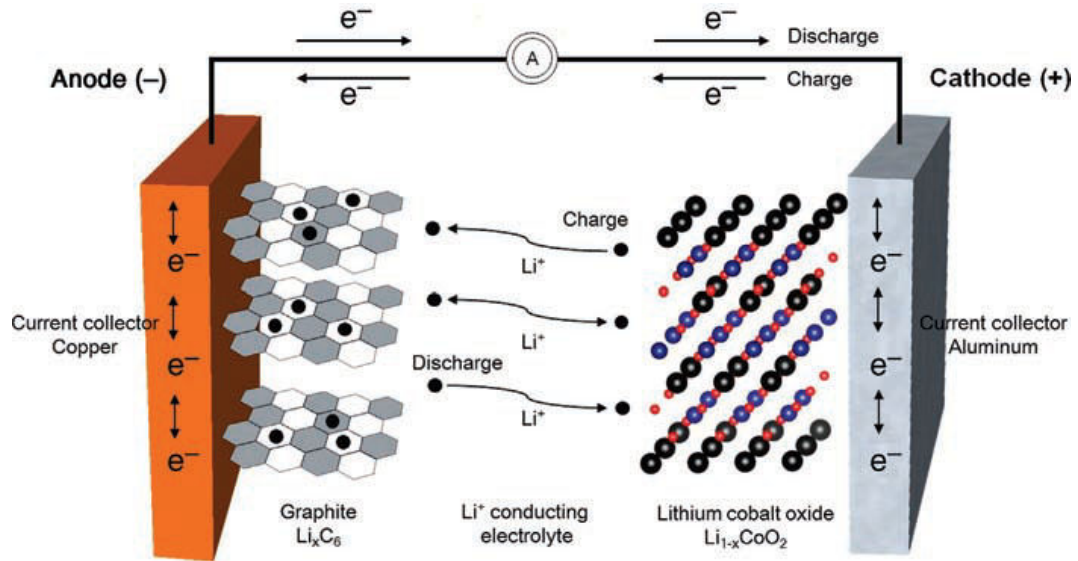
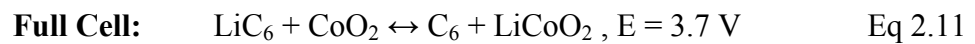
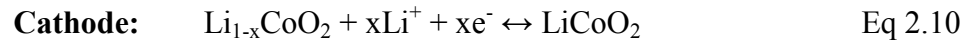
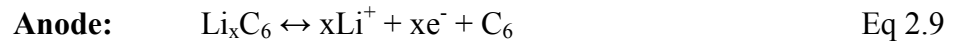


Figure 12: Schematic of Li-ion battery operation [43].



Cathode Materials

There are two categories of cathode materials used in lithium ion batteries; intercalation cathodes and conversion cathodes. Intercalation cathodes consist of compounds which act as a solid host network capable of storing guest lithium ions. Intercalations compounds include metal chalcogenides (LiTiS₂), transition metal oxide, and polyanion compounds. Conversion cathodes, on the other hand, undergo redox reactions during charge and discharge.

Intercalation Cathodes

Intercalation cathodes are classified according to their crystal structures. The largest group by far are layered structures, but significant interest has been seen in spinels, olivines and tavorites. Figure 13 shows the crystal structures of common cathode materials, with clear pathways for lithium intercalation. Figure 14 shows the specific capacity of different intercalation cathodes. The first and most successful cathode material, LiCoO_2 , can be seen to only be surpassed by its derivatives.

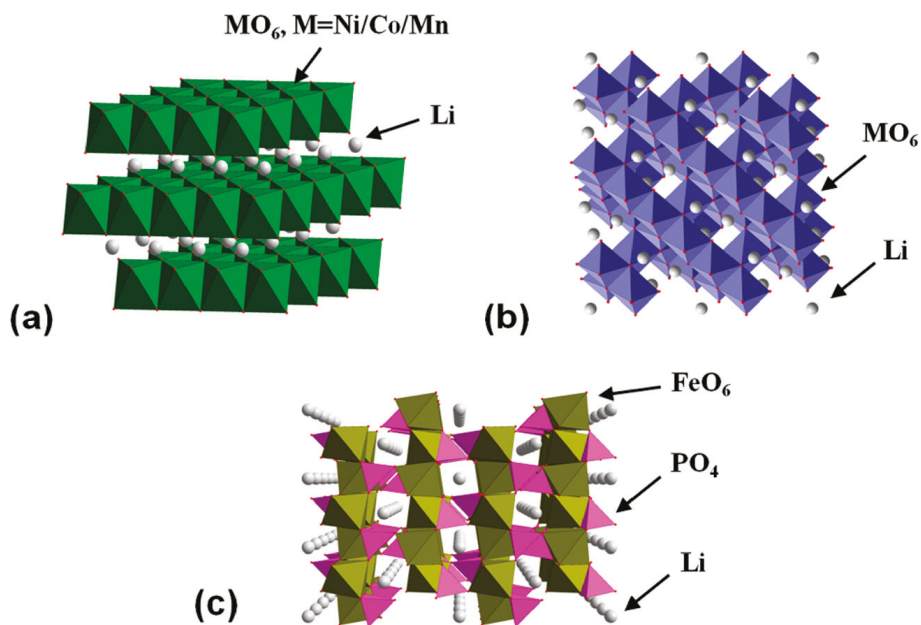


Figure 13: Crystal structures of a) layered (LMNCO) b) spinel (LMO) and c) olivine (LFPO) cathode materials [44].

LiCoO_2 has a theoretical capacity of 274 mAh g^{-1} , high discharge voltage (3.8 V) and excellent cyclability. However, the cobalt significantly increases the cost of the cathode. Additionally, its thermal stability is poor. This means that once heated to a certain point, it is likely to undergo a runaway reaction, releasing hot gaseous species. LiNiO_2 has the

same crystal structure, similar theoretical capacity and poor thermal stability. It does, however, have a significant cost advantage. Substitutions of nickel, aluminium, and manganese, into the cobalt lattice have proved advantageous.

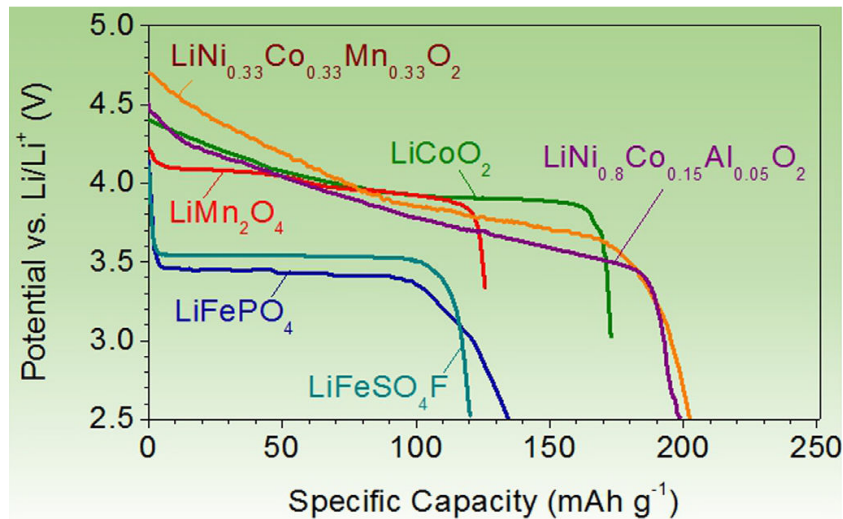
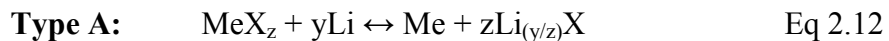


Figure 14: Specific Capacity of Intercalation Cathodes [4].

Unlike the layered materials, olivine cathodes have better thermal stability. However, the large polyanions $(\text{PO}_4)^{3-}$, which stabilize the structure, significantly reduce the theoretical specific capacity (170 mAh g^{-1}). The most common form of the olivine phase is LiFePO_4 , which has the lowest lithiation voltage of all the intercalation cathodes (3.4 V).

Conversion Cathodes

There are two types of conversion cathodes, based on the type of reaction that is occurring. These are Type A (Eq. 2.12) and Type B (Eq. 2.13). In Type A, MX is a metal halide, and the reaction is analogous to that seen in ZEBRA cells. Type B, on the other hand, is analogous to the Na-S cell, where X is commonly elemental S, but potentially selenium, tellurium or iodine.



The conversion cathodes generally have high theoretical and practical specific capacities, as shown in Figure 15. These are usually much higher than those for intercalation cathodes. Additionally, conversion cathodes generally make use of more abundant elements. However, three issues arise; low electronic conductivity, lowered open circuit voltages and volume expansion (2-30% in Type A, and 50-100% in Type B). Although none of these issues rule out conversion cathodes, additional care must be taken to prevent failure during operation.

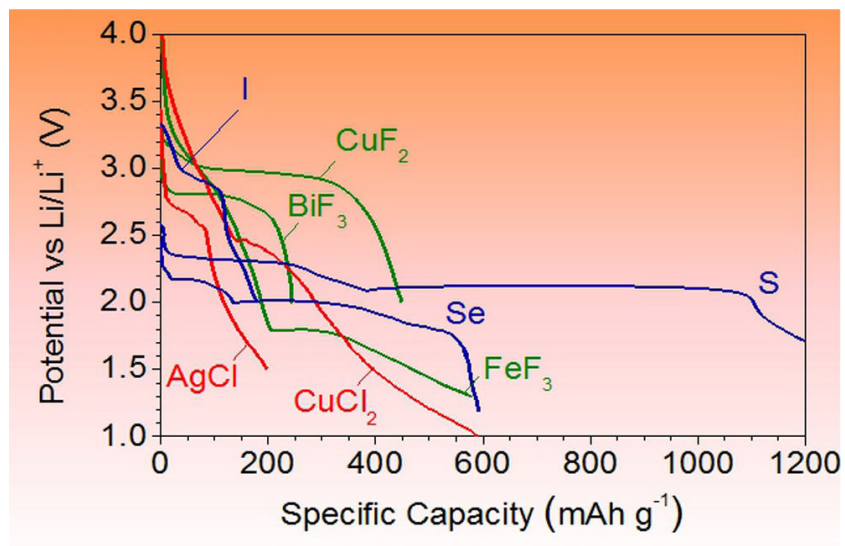


Figure 15: Specific Capacity of Li-ion conversion cathodes [4].

Anode Materials

Much like the cathode materials, anode materials can either be intercalation materials or conversion materials. Intercalation materials for anodes primarily focus on carbon based structures, as well as lithium titanate and its derivatives. Conversion anodes behave similarly to those of conversion cathodes, providing large specific capacities. The dominant conversion anode materials include silicon, tin and germanium. Like their cathode counterparts, their volume changes during cycling (>200%) are deterring [4].

Carbon-Based Anodes

The combination of good chemical and physical properties, combined with the low cost and abundance of graphite make graphitic anodes the more dominant anode used in commercial lithium-ion batteries. Graphitic anodes have large, ordered, graphite grains that can accommodate significant amounts of lithium. Ideally, a single lithium ion could be stored using six carbon atoms. Unsurprisingly, its practical capacity (280-300 mAh g⁻¹) approaches its theoretical capacity (372 mAh g⁻¹). It also has a high electronic conductivity and a low delithiation potential against Li/Li⁺ reference. This low potential is both a blessing and a curse, as it allows the cell to have very high voltage primarily driven by the cathode material. However, the low lithiation potential is close to that of pure lithium. The deposition of lithium metal, and the growth of lithium dendrites, is a dangerous possibility.

Alternatively to graphitic anodes, hard carbon materials have small, disordered, graphitic grains. Nanovoid defects within the grains mean that the volumetric change during

lithiation is reduced. The nanovoids can also increase the gravimetric capacity, but at the cost of the volumetric one. Hard carbon anodes also have low lithiation potential, and can potentially suffer from dendrite growth.

Lithium Titanate ($\text{Li}_4\text{Ti}_5\text{O}_{12}$) Anodes

One of the best alternatives to carbon, or metallic, anodes is lithium titanate [LTO]. At the cost of a lowered capacity (175 mAh g^{-1}), and increased lithiation potential (1.55 V), it is inherently safer than graphite. It also possesses long cycle life, predominantly due to its near-zero volumetric expansion during cycling. Because of its high potential, there are few side reactions with electrolytes used in batteries. Therefore, irreversible losses are mitigated. Additionally, this means that nanoparticles of LTO can be used. Nanoparticles help increase the anode's charge/discharge rates. Lastly, LTO's high lithiation potential makes it one of few anodes compatible with aqueous electrolytes, opening the gates to even safer batteries [45].

Capacitors

Capacitors are devices which are used to store energy as a reservoir of electric charge. The exact mechanism for storing a charge will be based on the type of capacitor. Capacitors can generally be separated into two types: dielectric (solid state) capacitor, and electrochemical capacitor.

In dielectric capacitors, the basic device consists of two conductive plates, connected to a power source, which are separated by an insulating dielectric material, as seen in Figure

16. The type of dielectric material depends on the application, but the amount of charge stored is based on Equation 2.14 and 2.15 when considering plate capacitors.

$$Q = C \times V \quad \text{Eq 2.14}$$

$$C = \epsilon_0 \epsilon_r \frac{A}{d} \quad \text{Eq 2.15}$$

Here Q is the amount of charge stored, C is the capacitance, and V is the voltage between the plates. The unit for capacitance is Farad (F). ϵ_0 is the permittivity of a vacuum ($8.85 \times 10^{-12} \text{ F m}^{-1}$), ϵ_r is the dielectric constant or relative permittivity of the dielectric, while A is the area of the capacitor and d is the distance between the plates. The total energy stored in a capacitor is defined by Equation 2.16.

$$E_{Total} = \frac{1}{2} CV^2 \quad \text{Eq 2.16}$$

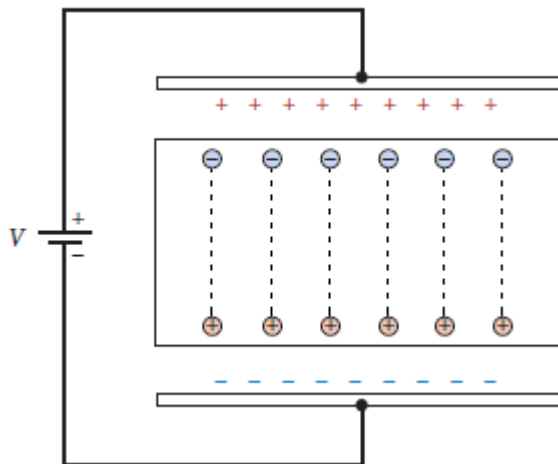


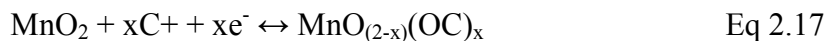
Figure 16: A simple dielectric capacitor.

Electrochemical capacitors (ECCs), often called supercapacitors, can be further broken down by mechanism. The two types of supercapacitors are electrochemical double-layer capacitors (EDLCs) and pseudocapacitors. Both types of ECCs have a higher capacity than dielectric capacitors, and can accommodate faster charge or discharge rates when compared to rechargeable batteries.

EDLCs store their charge electrostatically at the electrode-electrolyte surface, within the Helmholtz double layer. The thickness of the double layer is very small, on the order of angstroms. The double layer capacitance is dependent on the electrolyte composition and concentration, but is generally found to be between 5 and 20 $\mu\text{F cm}^{-2}$. Significant capacity can be achieved by using ultrahigh surface area electrodes, like activated carbons, where they can reach up to 300 F g^{-1} [46]. An additional benefit of EDLCs is that the surface storage mechanism does not have Faradaic reactions, meaning that unlike batteries, there are no volumetric changes during charging and discharging which allows for longer cyclability.

Pseudocapacitors make use of reversible redox reactions that occur at the surface of the active materials. Much like in EDLCs, a double layer is formed at the electrode-electrolyte interface. However, during polarization, an electron charge transfer occurs between the electrolyte ion (or molecule) and capacitor material. The reaction can be expressed as Equation 2.17, where C^+ represents solvated protons and alkali metal cations. The adsorbed ion is not chemically bonded to the electrode. Because of this, pseudocapacitors have a significantly higher capacitance than EDLCs, but can suffer cycling stability due to the redox reactions. Studies have shown different materials

exhibiting pseudocapacitance, including MnO_2 , Fe_3O_4 , Bi_2O_3 , RuO_2 . Even though these can present high theoretical capacitances (up to 1300 F g^{-1}) [47], they generally do not perform as well as EDLCs due to reduced kinetics.



Bismuth Manganese Oxide (BiMn_2O_5)

Bismuth manganese oxide [**BMO**] is a multiferroic material that exhibits ferroelectric and magnetic properties, as well as other functional properties [48]. Pyroelectric effects were reported in both single crystal and polycrystalline BiMn_2O_5 [49, 50]. BiMn_2O_5 consists of Bi^{3+} , Mn^{3+} , and Mn^{4+} ions. Mn^{4+} sits in Mn^{4+}O_6 octahedra, while the Mn^{3+} is found in Mn^{3+}O_5 square pyramids. The octahedra share edges, forming linear chains which are interconnected by the square pyramids. The Bi^{3+} is found inside large BiO_8 polyhedrons.

BiMn_2O_5 can be synthesized using multiple techniques. BMO and related compounds have been produced using high temperature solid state reactions [51, 52, 53, 54], hydrothermal synthesis methods [55, 56], and sol-gel or sol-gel precipitation techniques [57]. BiMn_2O_5 was reported to have a dielectric constant of $10^5 - 10^6$ at room temperature, making a likely candidate for capacitor material [58]. The multiple valence states of both manganese and bismuth further entices studying the material. With the exception of hydrothermal synthesis, BiMn_2O_5 particles have not been characterized as a super capacitor material [59]. The high density (7.15 g cm^{-3}) of BMO allows for a high mass loading to be achieved, proving beneficial in quadrupling the areal capacitance when compared to MnO_2 -MWCNT performance.

Electrophoretic Deposition

Electrophoretic deposition [EPD] is a method of depositing particles from a colloidal suspension onto a substrate. This differs from electrolytic deposition, or electroplating, where dissolved metal cations are reduced to form metallic coatings on an electrode. Generally, most EPD systems make use of water-based suspension medium; however non-aqueous systems can be used. Figure 17 shows that the charged particles from the suspension move toward the oppositely charged electrode when a DC electric field is applied. The electric field applied to a system is dependent on the wanted behaviour, but can be far above the limit for electrolysis of water, commonly reaching voltages above 100 V.

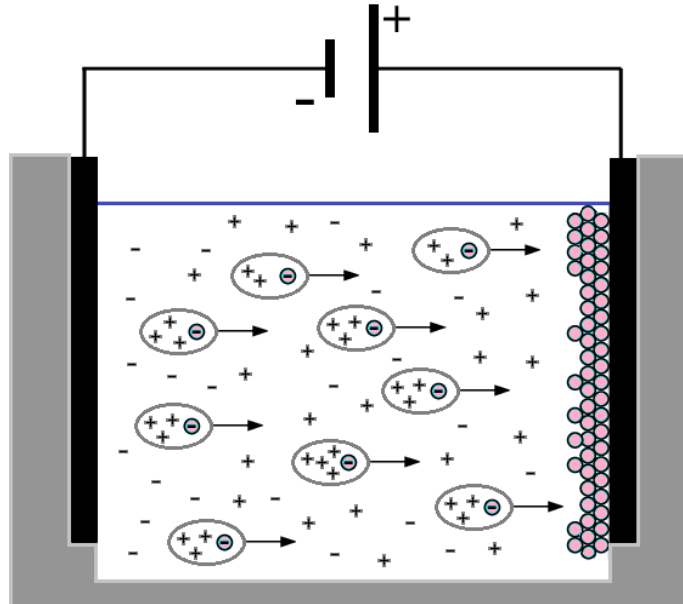
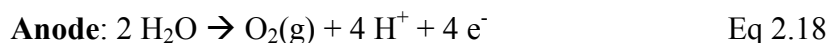
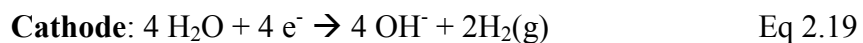


Figure 17: Schematic of anodic electrophoretic deposition.

The EPD process can be used to deposit material either on the cathode or the anode, depending on the state of the suspension. Anodic deposition occurs when negatively charged particles are deposited on the positively charged anode, while cathodic deposition is the mirror analogue. During anodic deposition, the particles are negatively charged from the salts of an acid, which are reacted with hydrogen ions generated at the anode from the electrolysis of water, as per the half cell reaction in Equation 2.18.



Similarly, in cathodic deposition, the particles are positively charged from the salts of a base. These protonated salts react with the hydroxyl ions generated at the cathode. The half cell reaction is presented in Equation 2.19. It is important to note that during deposition, both half cell reactions are occurring, even if particles are only depositing at one electrode.



EPD can be done using either a constant-voltage or constant-current operation. During constant-voltage operation, the electric resistance of the deposit at the electrode increases with deposit thickness. This increase in electrical resistance causes the electric field to decrease, which hinders particle motion and consequently lowers deposition rate. The velocity (v) of particles in a homogenous suspension is defined by Equation 2.20,

$$v = \frac{\varepsilon\varepsilon_0\zeta E}{\eta} \quad \text{Eq 2.20}$$

where ε is the dielectric constant of the liquid, ε_0 is the permittivity of free space, ζ is zeta-potential of the particles, E is applied electric intensity, and η is the dynamic viscosity of the liquid [60]. It can be seen from Equation 2.21 that the rate of deposition decreases exponentially with time,

$$\frac{dm}{dt} = m_0\alpha e^{-\alpha t} \quad \text{Eq 2.21}$$

where $\alpha = Av/V$, A is the area of the electrode, while m is the mass of the deposit, m_0 is the initial mass of particles in the suspension, and V is the volume of the suspension [60]. Equation 2.20 is the Helmholtz-Smoluchowski equation, and is generally only valid for systems where the particle is much larger than the thickness of the double layer around the particle.

The limited deposition observed in constant-voltage EPD is avoided when the process utilizes a constant current. The electric field is maintained by increasing the total potential as deposition proceeds.

To form high-density coatings, the colloidal suspension must be stable. Unstable solutions with agglomerated particles will form low-density films. However, in most cases, it can be expected that unaided colloidal suspensions will fall prey to flocculation.

This occurs during collisions between the suspended particles, where thermal vibrations are insufficient to overpower the attractive forces present.

Flocculation is generally avoided by increasing the repulsive forces between the particles. This can be done by three common methods; electrostatic stabilization, steric stabilization, and electrosteric stabilization. In electrostatic stabilization, the particles are repulsed based on charges on the particles surface which affect the electrical double layer around the colloids. Steric stabilization occurs when uncharged polymer chains are adsorbed on the particle surface. The interactions of these polymers repulse the particles through physical effects, where the polymers interpenetrate. This interpenetration can lead to either attraction or repulsion, but after a certain limit, the polymers become compressed, providing a repulsive force. Electrosteric stabilization utilizes charged polymers adsorbed on the surface of the particles. They possess both steric repulsion from the polymer chains, and double layer repulsion.

Sodium-Silicon System

The sodium-silicon system has remained relatively unexplored, with the majority of the focus on the silicon clathrates. These clathrate phases are categorized as Type I or Type II clathrates, where the former has a chemical formula of $\text{Na}_8\text{Si}_{46}$ and the latter $\text{Na}_x\text{Si}_{136}$. NaSi and NaSi_2 were two other sodium-silicon compounds reported for the system. However, NaSi_2 has not been corroborated [61].

The silicon clathrate materials having been scrutinized because of their cage crystal structures provide interesting properties. They have been shown to possess a wide range of electrical transport and thermal properties [62, 63, 64]. They also have been investigated for their thermoelectric [65, 66] and optoelectronic properties [67, 68, 69]. The Type I sodium silicon clathrate unit cell contains a lattice structure made up of 46 silicon atoms formed into two dodecahedra (Si_{20}) and six tetrakaidecahedra (Si_{24}). The eight sodium atoms reside within the polyhedra (Figure 18b). Likewise, the Type II sodium silicon clathrate contains 136 silicon atoms in sixteen dodecahedra and eight hexakaidecahedra (Si_{28}). In Type II clathrate, the silicon cages can be partially filled with a sodium atom, allowing for a composition of $0 \leq x \leq 24$ (Figure 18c). Although significant research has been undertaken on both types of clathrates, very few thermodynamic properties have been reported. However, both types of clathrates are not detected in the reaction of elemental sodium and silicon, but rather formed through decomposition of NaSi .

Currently, NaSi is primarily studied and used as a precursor to prepare the clathrate phases, either by high pressure [70] or in-vacuo processes [71] at elevated temperatures. NaSi, often written as Na_4Si_4 , is a Zintl phase with Si_4^{4-} tetrahedra isolated by Na^+ (Figure 18a). Recent works have shown NaSi to have potential applications in electrochemical energy storage. Other papers have explored the use of NaSi, and its liquid phase, to refine silicon crystals [72, 73] or deposit protective silicide coatings on rare-earth alloys [74]. Even less is known about NaSi than the clathrates, as it is primarily used as a means to an end. Additionally, the reactivity of both sodium and silicon at elevated temperatures, as well as a high sodium vapour pressure, complicate investigations of NaSi.

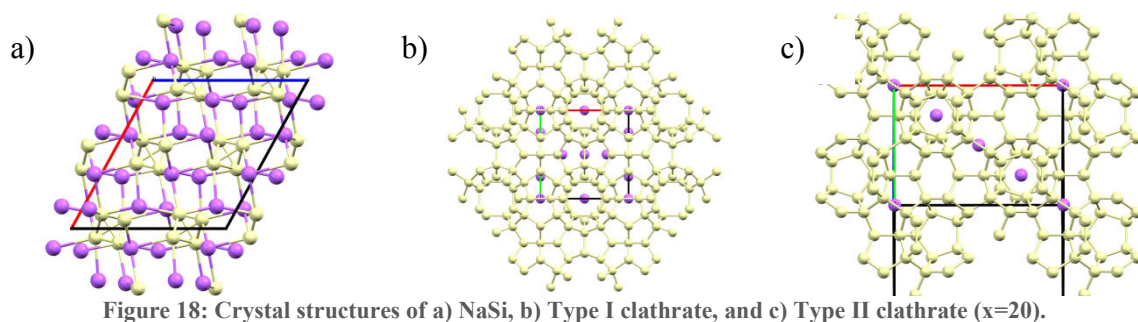


Figure 18: Crystal structures of a) NaSi, b) Type I clathrate, and c) Type II clathrate ($x=20$).

The most promising usage of NaSi is in the production of hydrogen for PEM fuel cells. In the reaction with water, it forms $\text{Na}_2\text{Si}_2\text{O}_5$ and produces hydrogen gas while releasing 175 kJ mol^{-1} of useable heat. NaSi production and use in fuel cells release significantly less CO_2 than other portable methods, with 81% of its carbon footprint coming from the production of silicon [75]. The energy density of NaSi for use in hydrogen technologies is 3 to 6 times higher than conventional hydrogen storage and battery energy systems [76]. Taking into account the long stability of NaSi in most conditions, with the fact that the

hydrogen is not stored in NaSi, it is inherently safer than hydrogen storage. NaSi-hydrogen supplied fuel cells are considerably less expensive in high volume usage, when compared to current disposable and rechargeable batteries [77].

Alternatively, NaSi could be potentially used in sodium-ion battery anodes. Much like silicon in lithium-ion batteries, the formation of NaSi at the anode has the potential of providing a capacity of 954 mAh g^{-1} . First principle calculations show sodiation voltages below 0.2 V [78]. Reversible sodiation of silicon nanoparticles has recently been successfully demonstrated to have a capacity of over 240 mAh g^{-1} after 100 cycles [79]. Others have reported improved capacity using mesoporous silicon microspheres [80].

Proposed Na-Si Phase Diagrams

Currently, there are two proposed phase diagrams. The first was proposed in 2009 by Morito et al. from a series of ten DTA measurements. Samples of pre-reacted NaSi were placed in an electric furnace, and the difference in thermocouple voltage between the sample and an empty standard were measured. This work identified a crystallographic phase change occurs in NaSi (LT-NaSi to HT-NaSi) at 612°C , and that pure NaSi melted congruently at 798°C [81]. This phase diagram is shown in Figure 19. A thermodynamic model of the Na-Si system was prepared by Hao et al. using first principle calculations, while attempting to match Morito's DTA data and crystallographic data for NaSi. However, the clathrate phases were not included.

The second phase diagram (Figure 20) was proposed by Mali et al. in 2013. The work attempted to refine the phase diagrams of Morito and Hao, by using electromotive force

measurements. Using glass sealed sodium beta-alumina galvanic cells the activity of sodium was measured for $\text{Na}_x\text{Si}_{1-x}$ from $X_{\text{Na}} = 0$ to $X_{\text{Na}} = 0.95$. Their results showed three distinctive sodium activity plateaus. These corresponded with three two-phase regions; $\text{NaSi-Na}_{(l)}$, $\text{NaSi-Na}_4\text{Si}_{23}$, and $\text{Na}_4\text{Si}_{23}\text{-Si}$. The EMF values in the sodium rich cells indicated little solubility of Si, assuming the liquid sodium exhibited Raoultian behavior. The solubility of silicon in molten sodium was calculated to be near 98% at elevated temperatures. The sodium activity of the $\text{NaSi-Na}_4\text{Si}_{23}$ and $\text{Na}_4\text{Si}_{23}\text{-Si}$ two phase regions was reported to be 2×10^{-3} and 2.12×10^{-5} at 550°C [82]. However, due to the lack of information on the HT-NaSi and Type II clathrate phases, they were left out of the model for simplicity.

The heat and entropy of formation for LT-NaSi were reported from the thermodynamic models and sodium vapour pressure experiments [83]. Wildly varying standard heats of formation were reported to be 5.3 [84], 53.7 [82], and 86 kJ mol^{-1} [83]. Similarly, the same authors reported the entropies of formation to be 12.1, 66.66, and 71 J K mol^{-1} , respectively.

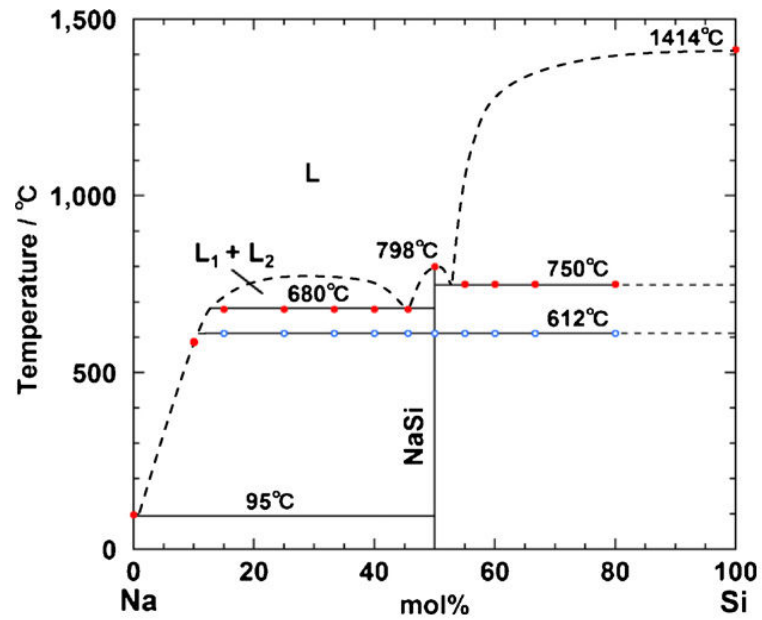


Figure 19: Na-Si Binary Phase Diagram by Morito et al.

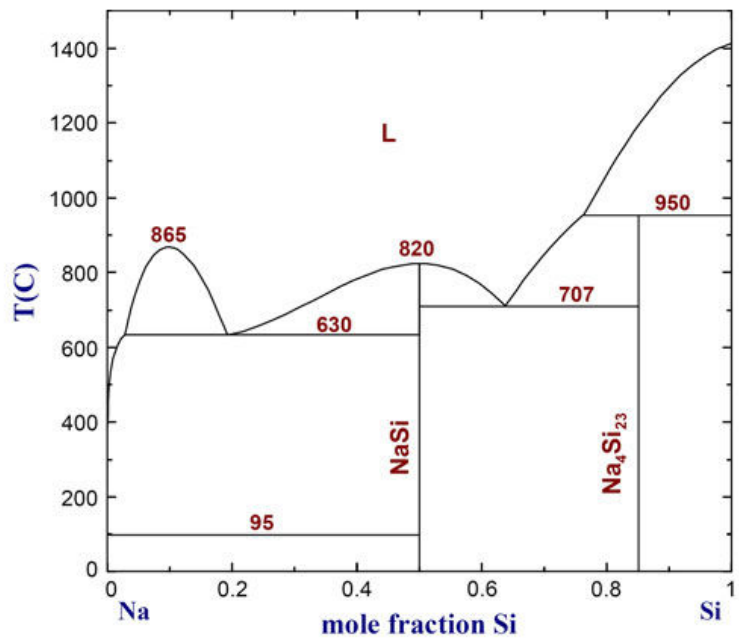


Figure 20: Na-Si Binary Phase Diagram by Mali et al.

Chapter 3: Problem Statement

Molten sodium metal batteries use a ceramic solid electrolyte tube. Although β -alumina is a fast ionic material, the electrolyte still represents a significant portion of the internal resistance of the battery. The resistance of solid electrolytes drop significantly with decreasing thickness. However, thin ceramic membranes are weak, but can be reinforced using a supporting membrane. Additionally, increasing the effective surface area using a porous duplex layer would significantly decrease the interfacial resistance. The objective for this project was to investigate the effects of porosity on the resistance of duplex BASE tubes. Rather than using EIS, a method using DC coulombic titrations was designed to separate the contributing effects of resistance. This method used multiple dense BASE tubes and tested their resistance while changing the exposed area to a sodium containing bath. A comparison of these tubes can be used to separate bulk and interfacial resistance of dense tubes. Repeating the test with duplex BASE tubes could be used to demonstrate a drop in interfacial resistance.

Sodium silicide, and the binary system it resides in, is relatively under researched, even though sodium silicide is a promising material in hydrogen gas production. Other than crystallographic information, and some chemical properties, very little is known about the phase. Development of an accurate sodium-silicon phase diagram would be advantageous for anyone using the system. The goal of this project was to characterize the phase at high temperatures, to gain a better understanding of the system. Several experiments are proposed in this work. These include analysis of the phase and its synthesis through the

use of DTA and DSC techniques, as well as high temperature XRD. Autoclaves are proposed for maintaining a sodium vapour atmosphere over the phase during high temperature melting experiments. A method of sealing sodium silicide for high temperature conductivity measures required of an inert atmosphere and reacting vessel.

BiMn_2O_5 is generally synthesized through bulk solid state processes or by expensive small batch hydrothermal methods. During solid state sintering at elevated temperatures, losses of bismuth due to volatilization becomes a problem. Significant post-synthesis processing is required to produce fine powders. On the other hand, hydrothermal processes produce powders with a good control over the composition and particle size distribution. However, in they generally have reaction times which often last several days. The approach taken by this work is to produce BiMn_2O_5 powders through a precipitation sol-gel synthesis. The powders can be quickly heat treated at various temperatures and time. These powders would then be tested for pseudocapacitance, and compared to those produced by hydrothermal processing. Sol-gel synthesis has the added benefit of scale. Increasing the batch size can be achieved with ease, and do not require specialized equipment.

The last project explored the production of lithium ion battery cathodes and anodes through electrophoretic deposition. Electrophoretic deposition is a potentially high throughput method of producing battery parts. The suitability of depositing films of LiFePO_4 , LiMn_2O_4 , $\text{LiMn}_{1.5}\text{Ni}_{0.5}\text{O}_4$, or $\text{Li}_4\text{Ti}_5\text{O}_{12}$ by usages of PAZO-Na or CMC-Na stabilized solutions was studied. Cells produced by this EPD process were to be tested as coin cells in a voltage window of 2.0 to 4.2 V vs Li/Li+.

Chapter 4: Experimental Procedure

This chapter details the procedures used in the synthesis and production of components tested during this study. Table 5 presents the materials used during synthesis and production, including their source and grade. This list is not exhaustive to all material used during the study, but represent those most used.

Table 5: List of Materials used in this work.

<u>Material</u>	<u>Provider</u>	<u>Grade or Purity</u>
Aluminium Nitrate Nonahydrate	Alfa Aesar	≥98%
Magnesium Nitrate Hexahydrate	Sigma Aldrich	≥99%
Sodium Nitrate	Caledon	≥99%
Bismuth Nitrate Pentahydrate	Sigma Aldrich	≥98%
Manganese Nitrate Hydrate	Sigma Aldrich	≥97%
Citric Acid Monohydrate	Caledon	≥99%
α-Alumina	Sumitomo Chemistry	AKP 50
Sodium Silicide	SiGNa Chemistries	—
Sodium	Alfa Aesar	99.8%
Silicon	Alfa Aesar	99.99% (-100+200 mesh)
Tin	Alfa Aesar	99.8%
Lithium Iron Phosphate	MTI Corporation	EQ-Lib-LFPO-S21
Lithium Manganese Spinel	NEI Corporation	Nanomyte BE-30
LiMn _{1.5} Ni _{0.5} O ₄ Spinel	NEI Corporation	Nanomyte SP-10
Lithium Titanate	Sigma Aldrich	≥99% (<200 nm)
Carbon Black	Alfa Aesar	Super P Conductive
Carbon Nanotube	Bayer Inc.	Baytubes C 150
Poly[1-[4-(3-carboxy-4-hydroxyphenylazo)benzenesulfonamido]-1,2-ethanediyl, sodium salt] [PAZO]	Sigma Aldrich	—
Carboxymethyl cellulose sodium salt [CMC]	Sigma Aldrich	—

Sol-gel synthesis of complex ceramics

Sodium β -Alumina Powders & Sodium-Aluminate Eutectic Seal

MgO-stabilized sodium β -alumina ($\text{Na}_{1.7}\text{Mg}_{0.35}\text{Al}_{10.65}\text{O}_{17}$) solid electrolyte [BASE] powders were synthesized through a modified sol-gel synthesis method unique to this study. Aluminium nitrate, sodium nitrate, magnesium nitrate and citric acid were dissolved together in de-ionized water. The citric acid was added at a molar ratio of 1:1 to the metal nitrates. This solution was then heated at 130°C until all water was evaporated. This formed an aerogel which was crushed into a fine powder. The crushed aerogel was rapidly heated on a hotplate to 220°C in an insulated Pyrex beaker. This caused the powder to ignite and convert to a mixture of oxides and carbon residue. The converted mass was calcined in an alumina crucible at 1100°C for 2 hours under flowing air. The resulting powder was ball milled in a 9 cm diameter ceramic jar for 5 to 7 days using zirconia milling media (0.5 cm) in anhydrous ethyl alcohol. The dried powder was then ready for use in slip casting slurries.

The sodium-aluminate powders used as the basis of the high temperature ceramic seal were synthesized using a similar procedure. The target composition corresponded to the eutectic of the $\text{Na}_2\text{O}-\text{Al}_2\text{O}_3$ system (35:65). Once calcined, these powders were ready to be used with a mixture of additives.

Bismuth Manganese Oxide Powder

Bismuth manganese oxide [BMO] powders were synthesized from a mixture of bismuth nitrate, manganese nitrate and citric acid. Manganese nitrate was added in so that Mn_2O_3

was in excess, but no more than 3 mass% of the final product. The metal nitrates were dissolved in nitric acid (1/3 dilution) and were added sequentially, fully dissolving prior to adding the next component. The ratio of nitric acid to metal nitrates was 4:1. Citric acid was added last, at a molar ratio of 1:1 to the metal nitrates. The solution was slowly heated at 90°C until the solution thickened into a dark orange-brown gel. It was then ignited at 220°C. The ignited powder was crushed and then calcined at temperatures between 450°C and 1100°C for up to 1.5 h. The resulting BiMn₂O₅ powders were confirmed by XRD analysis and ball milled for various amounts of time to achieve a desired final size which could be characterized by electrochemical methods.

Forming of Ceramic Parts

Pressing, Machining, and Sintering of α -Alumina caps

The electrochemical cells used in measuring solid electrolyte conductivity and sodium activity were made up of two parts; the BASE tube and an α -alumina cap. The cap was prepared by pressing 10 to 12 g of alumina in a 1/2 inch die under 24,000 lbs of pressure for 2 minutes. Alumina of 99.99% purity (*Sumitomo Chem.*) was mixed with 1.5 wt% polyvinyl butyral (PVB) binder prior to pressing. The green disks were heated at a rate of 3°C min⁻¹ to 1100°C and held for 2 h. The green-fired disks could then be machined with a WC drill and chamfer bit. The machined disks were then sintered at 1550°C for 4 h. The chamfer countersink was polished smooth, using a diamond burr, to provide the best finish for the mechanical seal. The design of the cap is presented in Figure 21. The alumina cap was machined to provide a hermetic seal to prevent sodium leakage.

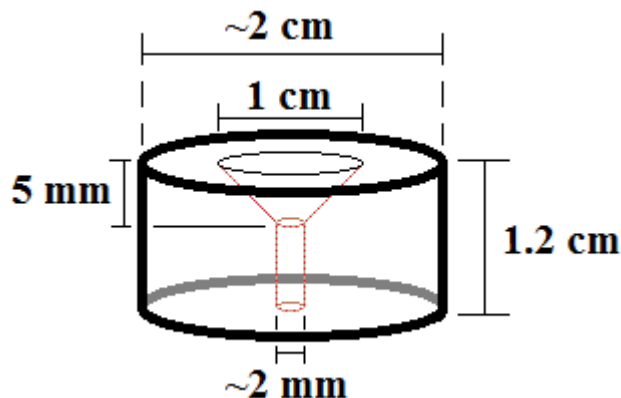


Figure 21: Schematic of α - Al_2O_3 cap used in BASE cells.

Slip Casting and Sintering of β -Alumina Electrolyte Tubes

Sodium β -alumina tubes were cast from slurries of BASE and methanol. The BASE powder absorbed moisture with time. This moisture, which would hinder the slip casting process, and produce cracked parts, was removed by dead-burning the powder at 1300°C for 5 h. The slurries were first concentrated to a mass ratio of 1:2 BASE powders to dehydrated methanol. This concentrated slurry was ball milled for 24 h to 48 h until the BASE powders reached a total surface area of approximately 2.8 – 3.2 m² g⁻¹. The surface area was measured using a Horiba CAPA-700 particle size analyzer. The slurry was then diluted with additional methanol to a solid content of 16-17 wt%, and ultrasonicated for 5 minutes to remove dissolved gas. The ultrasonicated solution was then ready to cast solid BASE tubes.

Alternatively, duplex tubes required two types of slurry. One portion was used as-is to cast the dense part of the duplex tube. For the other portion, spherical Poly(methyl methacrylate) [PMMA] powder (30 or 40 μm diameter) was added to a level of 45 wt% of the solid matter, with the total solid content in methanol remaining at 16-17 wt%. This

PMMA/BASE slurry was milled for an additional 5 minutes before ultrasonication to help homogenize it. The PMMA/BASE slurry was used to form the porous section of the duplex tube.

The moulds used in slip casting were made from pressed dyed-alumina powders. The mould powder was dyed by mixing < 1 wt% carbon into the alumina, which gave it a light gray colour. The mould cavity was formed by packing alumina powder around a mandrel. The mandrel was carefully removed so as to not damage the mould (Figure 22a). The mandrel used was a rounded cylinder with a diameter of 10 to 12 mm. This was sized to take into account sintering shrinkage of about 20%.

Dense BASE tubes were cast by slowly pouring the slip into the mould cavity until it was filled. The slurry was allowed to absorb for 5 to 30 minutes to achieve different thicknesses (Figure 22b). The slurry level was replenished as needed. After sufficient time, the slurry was poured out of the mould (Figure 22c), and the mould was then left upside down for several minutes to drain the remaining liquid (Figure 22f).

Duplex BASE tubes were cast in a similar manner to the dense tubes. They could be made to have porosity on either their inner tube surface, outer tube surface, or both. The outer surface porosity could be damaged during the cleaning of the tube or could remain clogged if improperly cleaned. Therefore, the inner tube configuration was the most convenient to produce. To make this duplex tube, the slurry without PMMA would be poured into the mould, and left to sit for 5 to 10 minutes. It would be poured out and then immediately replaced with the slurry that contained the PMMA pore former (Figure 22d).

This slurry would be poured out after 20 s due to the different settling rates of the PMMA and β'' -alumina (Figure 22e). Thicker porous sections could be achieved by repeating the 20 s casting step multiple times. The mould was then left upside down for several minutes to drain the remaining liquid (Figure 22f).

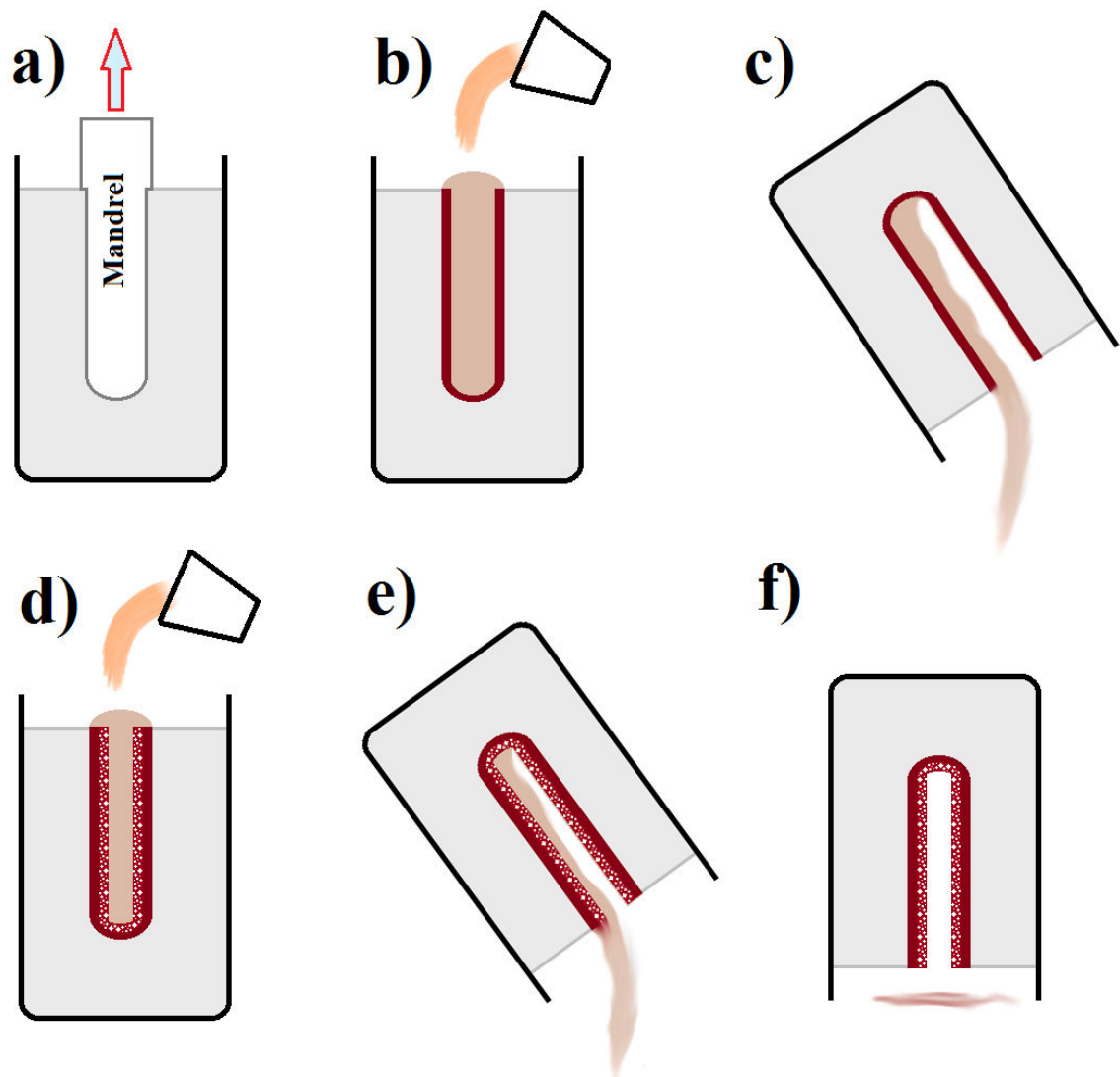


Figure 22: Slip Casting Process for Duplex BASE tubes with inner surface porosity.

Once cast, the moulds were covered and left to air dry for 24 h, followed by 12 h at 30°C in a convection drying oven. The casts were removed from the moulds by slowly removing the mould powder from around the parts. Once freed, the green parts were covered with a “thin” layer of gray mould powder. This layer was removed by carefully brushing off the gray mould powder until only the white beta part can be seen.

BASE tubes, whether of dense or duplex configuration, were sintered in the same two-step process to ensure the same grain-growth effects. The first step consisted of an intermediate temperature pre-sinter. The tubes were placed inside a sealed crucible and heated to 600°C, and held for 2 h, to burn out the PMMA and any other organics, followed by a strengthening step at 1300°C for 5 h (Figure 23). Once cooled, the part surfaces were lightly polished with 600 grit SiC paper. These polished tubes were then placed inside a closed crucible, which was filled with sodium oxide buffer (mixture of old BASE and 1% Na₂CO₃) for the second sintering step. The sealed crucibles were heated to 1650°C and held for 1 h for liquid phase sintering. This was followed by an annealing step at 1475°C, and held for 1.5 h, to remove internal stresses caused by the liquid phase sintering (Figure 24). Fully sintered cells were tested for through porosity using a liquid dye penetrant. Cells that leaked were crushed to be used as buffer material.

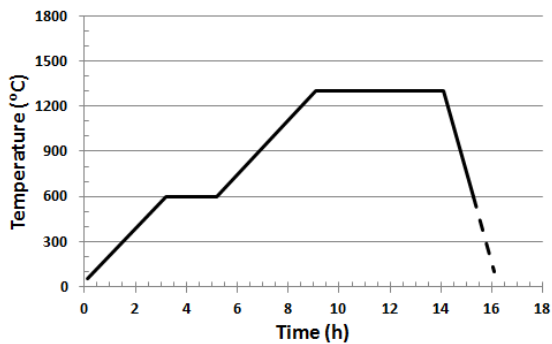


Figure 23: Pre-sintering temperature profile for BASE tubes.

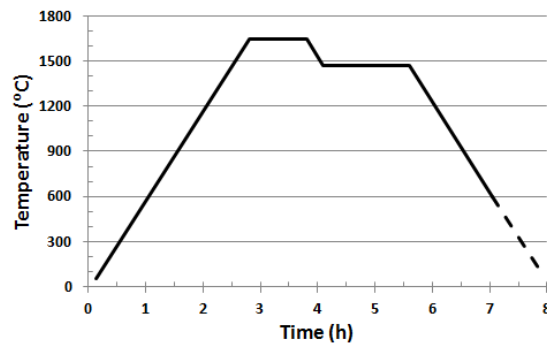


Figure 24: Sintering temperature profile for BASE tubes.

Sealing of β -alumina solid electrolyte tubes to Alumina Caps

BASE tubes were attached to alumina caps by a third material, either glass or an intermediate ceramic, which bonded with both components. The bonding agent was crushed to a fine powder in an agate mortar. The powder was mixed with screen printing oil in approximately a 1:1 ratio until a thick paste was obtained. The paste was applied over the flat surface of the alumina cap, and the open end of the BASE tube was lightly pushed into the thin layer of paste. The excess paste was pushed up against the tube edge for better wetting. The whole assembly was placed in a desiccating oven at 60 – 70°C for at least 2 hours. The assemblies could then be sintered based on the seal composition. The sealed cells were examined for defects and tested for leaks using the liquid dye penetrant.

Glass Seals

There were two primary glass seals used for lower temperature experiments. The Corning 1720 glass was suitable for temperatures up to 660°C, but required low sodium vapour pressure within the cell. Compounds with significant sodium activity would cause devitrification of the Corning glass. The alternative glass seal was more resistant to

sodium attack, but failed quickly above 450°C. Table 6 shows the composition of both glass seals.

Table 6: Composition by weight % of Glass Seals

	CTE	SiO ₂	Al ₂ O ₃	MgO	CaO	B ₂ O ₃	Na ₂ O	BaO	SrO
Corning 1720	4.2	57	20.5	12	5.5	4	1	—	—
Alternative Seal	5.6	46	10	—	3	26	4	6	6

Both the Corning 1720 glass and the alternative seals were sintered within a closed crucible without buffer because excess sodium oxide vapour would damage the seals. The sintering profiles for both seal are found below.

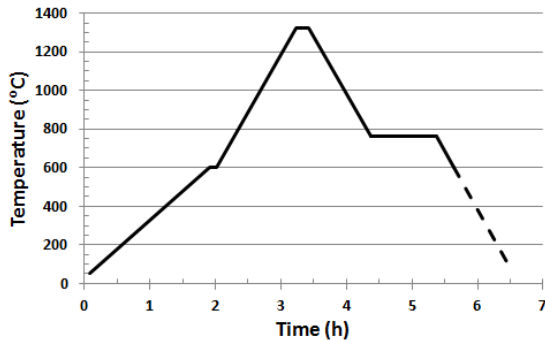


Figure 25: Temperature heating profile for Corning 1720 glass seal.

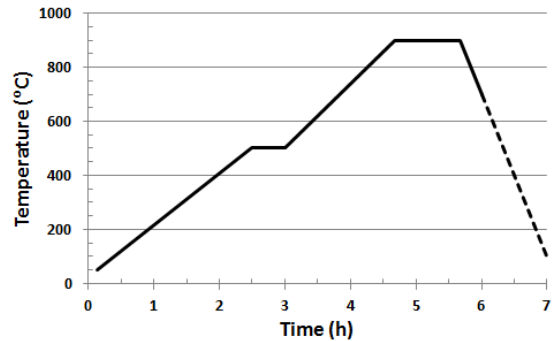


Figure 26: Temperature heating profile for the alternative seal

Ceramic Seals

Alumina-based ceramic seals would theoretically resist high sodium vapour pressures at elevated temperatures. The eutectic sodium-aluminate powder was used as the primary component of ceramic seals. Literature showed that it could be used by itself; however, the sealing capability was sporadic at best [85]. The sintering profile used for the eutectic sodium-aluminate powder included a dwell at 1650°C. Figure 27 shows a dwell time of

30 minutes, however, dwell times tested ranged from 6 minutes to 1 hour. To prevent sodium loss in both the seal and the BASE tube, the assembly was protected by buffer.

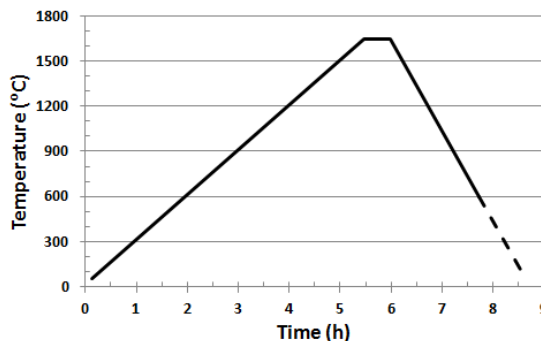


Figure 27: Temperature profile for eutectic composition ceramic seal.

One of the more promising ceramic seals was reported to be a mixture of CaO and Al₂O₃ [86]. At a mole ratio of 1:1, the melting point of the ceramic was 1415°C, which was promising for sealing BASE tubes to alumina caps. Other oxide and phosphate materials were used in an attempt to find a successful ceramic seal. These have been compiled in Appendix: Ceramic Compositions Used for Sealing BASE Tubes.

β-Alumina Solid Electrolyte Ionic Resistance Testing

The ionic bulk and interfacial resistance components of BASE tubes were calculated by measuring the overall resistance of cells while changing the amount of exposed surface. This was obtained by coulometric titrations through the cell wall, using an EG&G Model 173 Potentiostat/Galvanostat fitted with an EG&G Model 179 Coulometer as the current source. Two HP 34401 multimeters, connected to LabVIEW software, recorded the current and voltage during the experiments. The experiment used a three electrode test setup Figure 28, using two cells, one empty and the other filled with pure sodium. Nickel

or tantalum powder was added to the empty cells to complete the circuit, allowing pure sodium to be titrated into them. The metal powders did not affect the cell due to negligible solubility. Figure 29 shows the construction of the electrode assemblies. The counter electrode was a tantalum or steel wire. All three electrodes were placed into a liquid Sn-1.5 wt% Na bath to provide a supply of sodium. A low sodium bath was chosen to reduce the vapour pressure of sodium over the bath, which was open to the rest of the glovebox. A covered K-type thermocouple was also dipped in the bath for accurate temperature measurements.

The bath and electrode assemblies were all slowly heated together to 300°C, to prevent thermal shock of the ceramic parts. At this temperature, the bath was molten, allowing all the electrodes to be inserted to a depth of at least 2 cm. The initial sodium from the bath could be titrated into each cell at this time. This initial sodium diluted any impurities in the cell, and allowed for accurate OCV readings. The cells were left to equilibrate with the bath for another 24 to 72 hours, allowing the bath and sodium to properly wet their “relative” surface of the BASE. The equilibration was aided by titrating small amounts of sodium into and out of the cell at low currents. After the equilibration, the OCVs recorded were 0 mV, with less than a millivolt error, and the test could be performed. OCVs with excessive deviation from 0 mV indicated that a bad cell was in use. The most common errors were due to contact issues within the cell or between the cells and the bath. These were fixed by adding more metal powders into the cells and making sure they were dipped far enough into the bath. The other common issue was a cracked tube or seal.

These could be determined easily as the OCV of the sodium cell relative to the tin bath would quickly stabilize at a value around 600 mV. In this case, a new cell was needed.

The quantitative resistance tests were done by titrating sodium into the cell for at least 15 minutes at low currents (1 to 5 mA). The duration of the titration was based on the stability of the readings. When the titration ended, the cell OCV was allowed to stabilize. The cell was subjected to a titration in the opposite direction, pushing an equivalent amount of sodium out of the cell. Once this titration was completed, the cell would be allowed to stabilize and then pulled up slightly by 2 – 4 mm for another run. This procedure was repeated at least 5 times. The resistances for a single cell were plotted versus the area exposed to the bath. The slope of the line described the resistance profile of the cell. Multiple cells were tested to find the bulk and interfacial resistances. The procedure is further explained in Chapter 5: Duplex Solid Electrolyte.

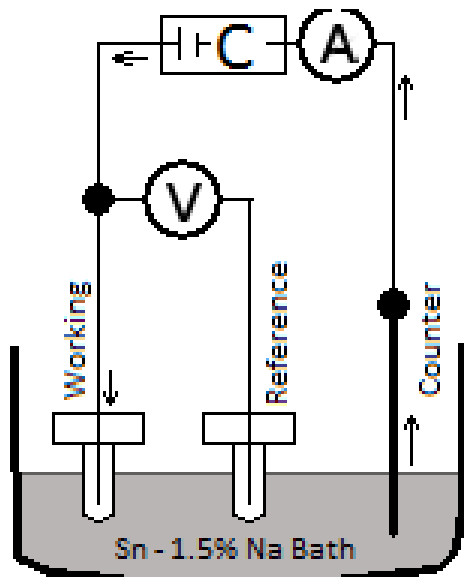


Figure 28: Schematic of coulometric bath. The arrows indicate the electron flow during titration into the cell [85].

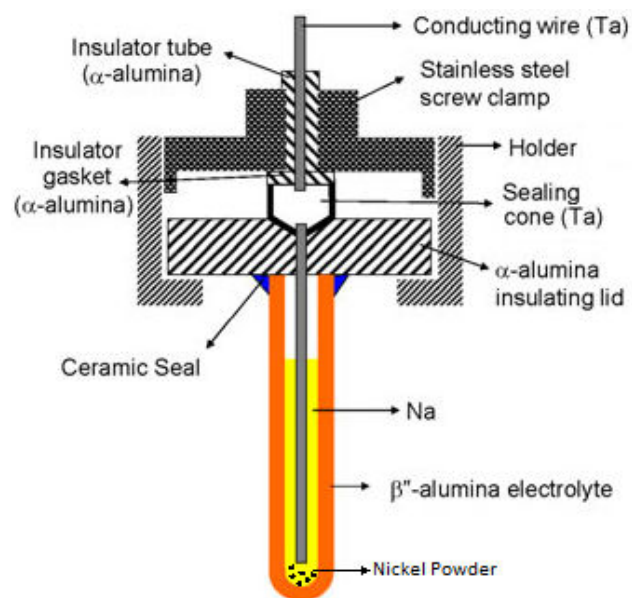


Figure 29: Working and reference (no nickel powder) electrode construction [85].

Sodium Silicide Characterization

Thermodynamic Study of Na-Si System

The thermodynamic study of the Na-Si system made use of the same BASE cells as used in the conductivity measurement. However, since most transition metals react with silicon, only tantalum could be used as a connective material. It should be noted that traces of $TaSi_x$ could be detected by XRD after significantly long tests.

Conductivity of NaSi experiment

The conductivity of NaSi was determined by 4-point experimentation methods. Unfortunately, due to its mechanical properties, high reactivity, and instability, NaSi cannot be machined into shapes convenient for conductivity testing (ex: rods, rectangular prisms). A method of testing NaSi was devised. A rectangular boat was fitted with four

electrodes (Figure 30) and filled with silicon powder and sodium at an approximate 1:3 mass ratio. This boat was enclosed inside a larger crucible and capped with alumina wool (Figure 31). The whole assembly was then placed inside a tube furnace and flushed with argon before heating it to up to 550°C , where the sodium would dissolve the silicon. Higher temperatures were used to evaporate excess sodium. The voltage drop across the assembly was measured at constant current while the excess sodium evaporated. Once the reading stabilized, the sample was cooled while measurements continued. The NaSi would crack due to thermal contraction, so a single sample could not be reheated once formed.



Figure 30: 4-probe crucible for NaSi conductivity

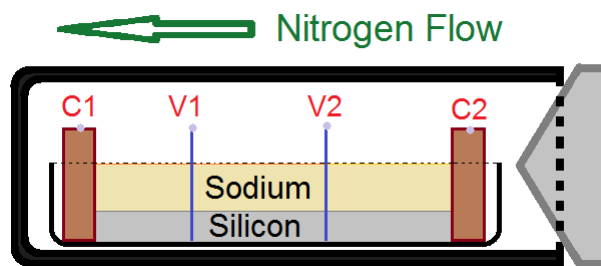


Figure 31: Schematic for sealing of NaSi 4-probe system

An alternative method of measuring the conductivity was to manually chisel a piece of NaSi into an approximate rectangle. Steel electrodes were attached to opposite ends using

a small dab of sodium metal, ensuring electrical contact. However, this could only be used for temperatures below the melting point of sodium.

DTA / DSC Characterization

Thermochemical analysis of NaSi was first performed by DTA as a qualitative measurement for comparison with literature. The cells used in the DTA were bulky, but could sustain experimental temperatures up to 1100°C. These DTA experiments were performed using a Netzsch STA 409 PC. The cells used for DSC experiments were refined from the original design, moving away from a screw seal to an interference fit cap. The interference fit produced a mechanical seal when pressed in a WC die using 5000 pounds of force. These cells were safely operated up to 650°C without observable mass loss on a scale with microgram accuracy. The DSC experiments were performed on a Mettler TGA/DSC 3+. The design of both the high temperature DTA cells (Figure 32) and high precision DSC cells (Figure 33) are shown below.

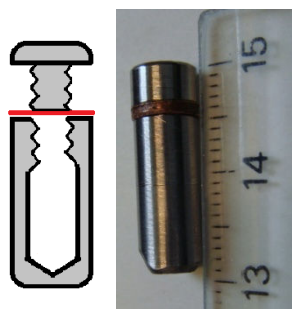


Figure 32: DTA cell. Made from 300-series steel and screw (Mass >3000 mg). Chamber allowed ~100 mg NaSi.

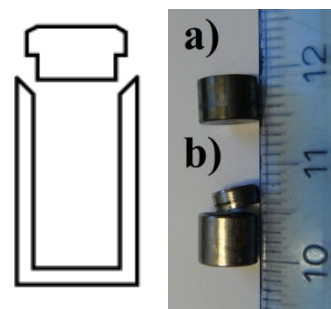


Figure 33: DSC cell. Made from 300-series steel (Mass ~800 mg). Chamber allowed for ~40 mg NaSi.

The limitations on the Mettler device required the use of a reference that was mismatched to the test cell. A small alumina crucible (~200 mg) was used. This caused significant signal discrepancy which needed to be taken into account. A cell with a silver standard was tested to obtain a background of the system, and a nickel standard was tested to calibrate the curve. For the Netzsch device, a 3 g slug of steel was used as the reference.

Determination of NaSi Melting Point

The melting of NaSi was attempted using multiple methods. These methods included high temperature XRD analysis, high temperature autoclaves for bulk samples, as well as DTA testing mentioned above. All these tests utilized NaSi powders from SigNa Chemistries.

The high temperature XRD analysis required that the NaSi powder sample be loaded into a quartz capillary. This capillary was evacuated to high vacuum and flame sealed. Additionally, a calibration capillary was filled with MgO in the same manner. The heating stage was calibrated by heating the MgO capillary and calculating the length of the lattice constant. This was compared to literature values, providing an accurate temperature profile ($\pm 2^\circ\text{C}$) for the device. The NaSi sample was measured at multiple temperatures, up to the device's maximum temperature of 770°C . Both the calibration and NaSi samples were mounted to the heating stage as seen in Figure 34. The silicon wafer was placed under the NaSi in case of rupture.

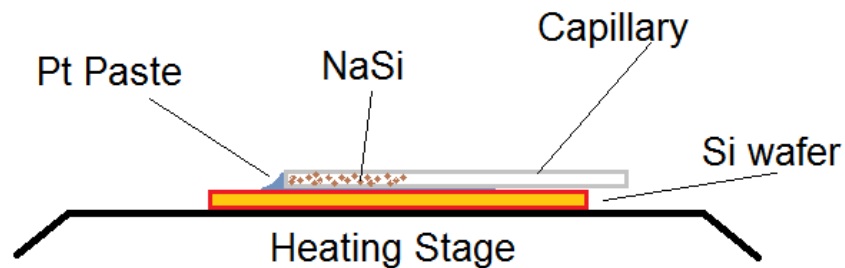


Figure 34: Mounting of capillaries to the heating stage for high temperature XRD.

One of the many issues with NaSi was its instability at high temperature. At elevated temperature, the sodium vapour pressure over the phase was significant, causing it to decompose to sodium-poor clathrates. To combat this problem, and effectively melt NaSi, an autoclave was designed to withstand temperatures up to 1000°C without losing a high sodium vapour atmosphere. The autoclave was constructed from Swagelok® parts and tubes. The NaSi was placed inside a thin alumina crucible, which was placed inside the autoclave. A small amount of sodium was placed in the crucible, but not in contact with the NaSi, to supply the sodium vapour atmosphere. The assembly was heated in a box furnace and allowed to equilibrate. It was then opened destructively once cooled, and the alumina crucible cracked open to visually inspect for signs of melting.



Figure 35: Swagelok® autoclave design, with long alumina crucible.

Production of Electrochemical Electrodes using Ceramics for Energy Devices

Electrophoretic Deposition of Ceramic Materials

Electrophoretic deposition was used to deposit various formed ceramic powders on metallic electrodes. The ceramic powders investigated were $\text{Li}_4\text{Ti}_5\text{O}_{12}$ [**LTO**], LiMn_2O_4 [**LMO**], $\text{LiMn}_{1.5}\text{Ni}_{0.5}\text{O}_4$ [**LMNO**], LiFePO_4 [**LFPO**], BASE, and BiMn_2O_5 [**BMO**]. These powders would be suspended in a solution by ultrasonication. The solutions primarily used were 1 g L^{-1} PAZO in 25Water-75Ethanol, and 1 g L^{-1} CMC in 30Water-70Ethanol. Other suspensions were also attempted for certain ceramics; primarily BASE and LTO as they were the most difficult to deposit. The solutions were prepared prior to adding the ceramic powders.

For the purpose of characterizing the coating quality by SEM and FTIR analysis of polymer-ceramic bonding, the ratio of ceramic to polymer in solution was kept to 2.67:1 by mass. The powders were deposited on steel coupons (4 to 6 cm^2) at voltages of 10, 30, and 50 V for 10, 5, and 3 minutes, respectively. Small squares from the center of the electrode were cut and prepared for SEM imaging, while the remainder of the coating was harvested for FTIR testing.

The lithium oxide ceramics were used as anodes (LTO) or cathodes (LMO, LMNO, LFPO) in button cell battery tests. As such, these were deposited on aluminium (cathodes) and copper (anodes) substrate films with a 25 cm^2 surface. The ceramic

powder to polymer was reduced to a 9:1 ratio. Additionally, carbon black was added at a 9:1 ceramic/polymer to carbon ratio. The voltages and polymers used to prepare each of the 25 cm² electrodes were determined from the coating quality tests. The deposition time was experimentally determined to produce cathodes with mass loading of 4 to 6 mg cm⁻² and anodes of 7 to 9 mg cm⁻². Once dried, the anodes and cathodes were ready for button cell testing.

The bismuth manganese oxide powder was coated onto steel electrodes for use as thin film capacitors. PAZO and CMC solutions were prepared such that the polymers were 10% of the total deposit mass. The BMO and CNT were mixed in a mass ratio of 4:1. The steel electrodes were masked to produce a coating around 2 cm by 2 cm. The BMO-CNT materials were electrophoretically deposited at 30 V for up to 20 minutes to produce mass loadings between 1 and 2 mg cm⁻². Once dried, the electrodes were placed in a vacuum for 12 hours, and then rolled to prevent contact resistance. It was then mounted on a copper lead, and all edges and excess steel substrate were covered in epoxy.

BiMn₂O₅ Loaded on Nickel Foam Electrode

The bismuth manganese oxide material was placed in a nickel foam electrode. BMO and CNT were mixed in a mass ratio of 4:1 in ethanol solutions and ultrasonicated. Once dispersed, they would be filtered and dried. The BMO-CNT powder would be crushed and mixed with 3 wt% PVB from a 1 wt% ethanol solution. The nickel foam would be filled using the above mixture, covering an area of 1 cm², while periodically drying the foam. Once the electrode was loaded with approximately 55 mg of BMO-CNT, it would

be rolled to 80% of its original thickness. It was then mounted on a copper lead, and all edges and excess nickel foam were covered in epoxy.

Testing of Electrochemical Electrodes

Bismuth manganese oxide was tested for pseudocapacitance using a PARstat 2273. The electrodes were placed in a 0.5 M Na₂SO₄ solution, and tested using a 3-probe assembly, as shown in Figure 36. The counter electrode was a platinum mesh, and the reference was a standard calomel electrode. Prior to testing, the electrodes were activated by running one hundred 20 mV s⁻¹ cyclic sweeps until the response was stabilized. The electrodes were then tested at rates of 2, 5, 10, 20, 50, 100 mV s⁻¹ to characterize its capacitance. The voltage window for cyclic sweeps was from 0 to 800 mV. Finally, the electrode was tested by EIS.

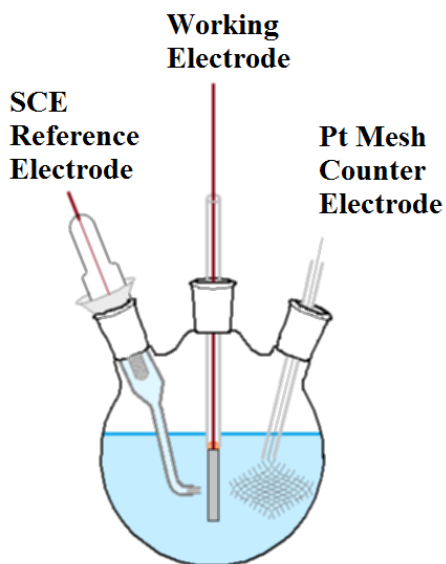


Figure 36: Three-electrode cell for testing capacitance of BiMn₂O₅.

Lithium ion oxide material anodes and cathodes were sent to National Research Council Canada for performance testing. The electrochemical tests were performed using 2325 coin cells, with an electrolyte of 1 M LiPF_6 solution in ethylene carbonate:diethyl carbonate mixed solvent (3:7 volume ratio). The cathode and anode were separated by a 30 μm polymer film (Celgard 2500). Galvanostatic measurements were carried out on a multichannel Arbin BT2000 battery cycler. Cyclic voltammetry tests were conducted using a Solartron SI 1287 potentiostat.

Chapter 5: Duplex Solid Electrolyte

This study explored the use of a porous layer to reduce the interfacial ionic resistance of β -alumina solid electrolytes. BASE tubes with (duplex), and without (dense), the porous layer were slip cast using sol-gel synthesized $\text{Na}^+ \beta/\beta''$ -Alumina. The porous layer was produced by slip casting a mixture of BASE and PMMA powders. The resistance profile of individual tubes was measured by a series of coulometric titrations through the cell walls while changing the area exposed to a Sn-1.5% Na bath.

A total of ten dense and two duplex tubes were successfully tested using this method. Using comparative methods, the average bulk conductivity and interfacial resistance of the dense cells were found to be $8 \times 10^{-2} \text{ S cm}^{-1}$ and $3.4 \text{ } \Omega \text{ cm}^2$. Using the bulk conductivity of dense cells, the interfacial resistance of the duplex cells was calculated to be $0.83 \text{ } \Omega \text{ cm}^2$.

Experimental Considerations

Assumptions and Mathematical Derivations

The experiments performed to determine if a reduction of interfacial resistance had occurred, as a result of adding a porous layer to BASE tube surfaces, required that multiple cells of different thickness be compared. Certain assumptions were expected to hold true for comparison of the cells to be valid. These assumptions fell into three categories: the properties of β -alumina, the symmetry of the BASE tubes, and experimental procedures.

In terms of assumptions based on the properties of β -alumina, it is important to recall that the β -alumina used in all experiments was produced by small batches of 15 g, which was sufficient to produce four BASE tubes. Even though different batches were produced in an identical method, variability in the final product was expected. This variation could manifest as compositional changes due to sodium loss during high temperature processing, or as differing grain size profiles. It was assumed that this would not affect the ionic transport properties of the tubes, such that the internal resistivity of cells would be identical, as well as the surface properties for dense tubes. Additionally, it was assumed that sodium ions would only travel in a linear fashion through BASE boundaries that were in contact with both sodium and tin-sodium melts.

The cells were also assumed to be perfect hemisphere capped-cylinders, with uniform wall thickness. However, due to the nature of slip casting and sintering processes, the cylinders would have slightly thicker walls near the closed-end than the open-end. This would also cause a slight narrowing of the external diameter. Slight warping of the circumference of the tube could sometimes occur due to the liquid state sintering. It was assumed that this minor shape deviation would not affect the results of the test.

Finally, the tests were performed within a sealed chamber in a glovebox, which was heated using an external furnace. The temperature of the bath could only be controlled to $\pm 5^\circ\text{C}$. This was due to a response delay in temperature control of the apparatus. All cells were tested at 360°C . It was assumed that the temperature error would not significantly affect the results.

The assumptions above allowed for Equation 5.1 to be true for all dense tubes. From the assumptions, $\sigma_{Electrolyte}$, or the bulk conductivity of the dense portion should remain constant for all cells. t_{Dense} was the thickness of the dense portion of the electrolyte, both for duplex and dense cells. χ_{Solid} and χ_{Porous} were the interfacial area specific resistance of the solid and duplex cells, respectively. The area of contact, $A_{Contact,S}$, was determined by Equation 5.2. It also represents the internal surface area of the dense portion of duplex cells.

$$R_{Total} = \frac{1}{A_{Contact,S}} \left(\chi_{Solid} + \frac{t_{Dense}}{\sigma_{Electrolyte}} \right) \quad \text{Eq 5.1}$$

$$A_{Contact,S} = 2\pi r_{in} \left((L_{Dip} - r_{out}) + r_{in} \right) \quad \text{Eq 5.2}$$

Where r_{in} is the internal radius of the BASE tube, r_{out} was the external radius of the BASE tube, and L_{Dip} was the distance the cell was dipped into the tin bath for a specific resistance reading. The resistance is calculated by Equation 5.3, where the difference in voltage between titration (V_I) and open circuit (V_{OCV}), is divided by the current passed through the BASE wall.

$$R = \frac{V_I - V_{OCV}}{I} \quad \text{Eq 5.3}$$

Several readings of the cell resistance were taken by changing the depth of immersion. These were plotted against the inverse of the surface area, providing a linear relationship. The slope of the line included the effects of the bulk conductivity and surface resistance,

as per Equation 5.4. Theoretically, the y-intercept of the graph was expected to cross at the origin; however, this was rarely the case. The magnitude of the deviation from the origin likely reflects the quality of the data, but the exact cause could not be determined. Ideally, the slopes of the line between dense cells should only vary due to the differing cell wall thicknesses.

$$Slope = \chi + \frac{t}{\sigma} \quad \text{Eq 5.4}$$

The slopes of two cells of different wall thickness could then be compared to resolve the bulk conductivity and interfacial resistance of cells made with this β -alumina. Multiple pairs of cells were analyzed using Equation 5.5 and 5.6 to increase the accuracy of the analysis.

$$\sigma = \left(\frac{t_1 - t_2}{S_1 - S_2} \right) \quad \text{Eq 5.5}$$

$$\chi = \left(\frac{S_2 t_1 - S_1 t_2}{t_1 - t_2} \right) \quad \text{Eq 5.6}$$

Wettability of BASE Tube

In high temperature sodium metal batteries, the solid electrolyte is smooth. The introduction of a porous system increased the difficulty of wetting the BASE tube surface. Sodium metal had to be embedded into the pores to provide the highest possible effective surface area. Considering the low wettability of sodium on β -alumina, as well as the high surface tension of liquid sodium metal, it was unlikely that sodium would infiltrate the

pores without assistance (Figure 37). The ideal method was to titrate sodium through the electrolyte into the pores. However, for sodium to form inside the pores, it needed to be reduced from Na^+ to its metal form. This required a conductive coating inside of the pores to complete the circuit. Without this coating, the sodium metal would form on the outermost edge of the tube. A thin coating of graphite was introduced into the pores to provide the conductive pathway (Figure 38). The graphite was added using a slurry of graphite and methanol. The total amount of graphite introduced was less than 100 mg. It was assumed that this graphite coating would have negligible effects on the ionic conductivity of the BASE. However, it is known that carbon lowers the contact angle of metal sodium on BASE surfaces [87]. Therefore, all dense and duplex cells were treated this way.

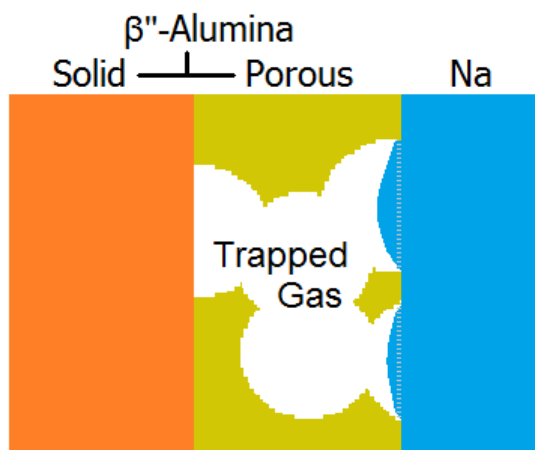


Figure 37: Inability to embed sodium metal into the porous layer of duplex cells.

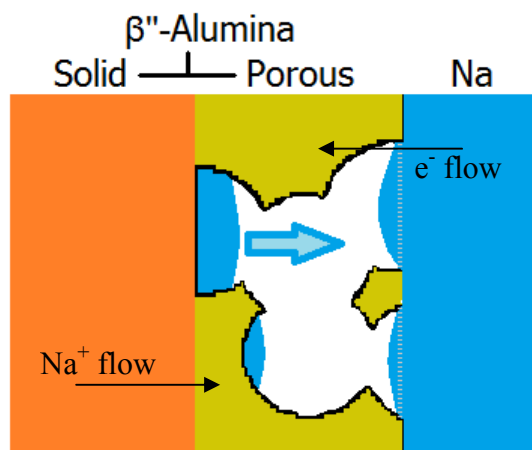


Figure 38: Effects of carbon coat on titration through porous layer of duplex cell.

PMMA vs Carbon Powder as Pore Formers

Two pore forming materials were used in the casting of duplex tubes; carbon powder and uniform PMMA spheres. The pore forming material, regardless of composition, was added to the slurry such that it accounted for 45% of the solid mass. Taking into account the densities of PMMA and carbon powders, this corresponded to 69% and 55% void volume of the porous portion of the duplex part, respectively.

The carbon powder created tortuous paths of narrow channels within the porous section. These channels were on the order of 10 μm in diameter (Figure 39). One of the primary benefits of the carbon powder was that it mixed and cast well with beta alumina. However, due to the nature of the pores, it was difficult to calculate total surface area provided by the porous section. Additionally it was difficult to infiltrate sodium into the narrow pores.

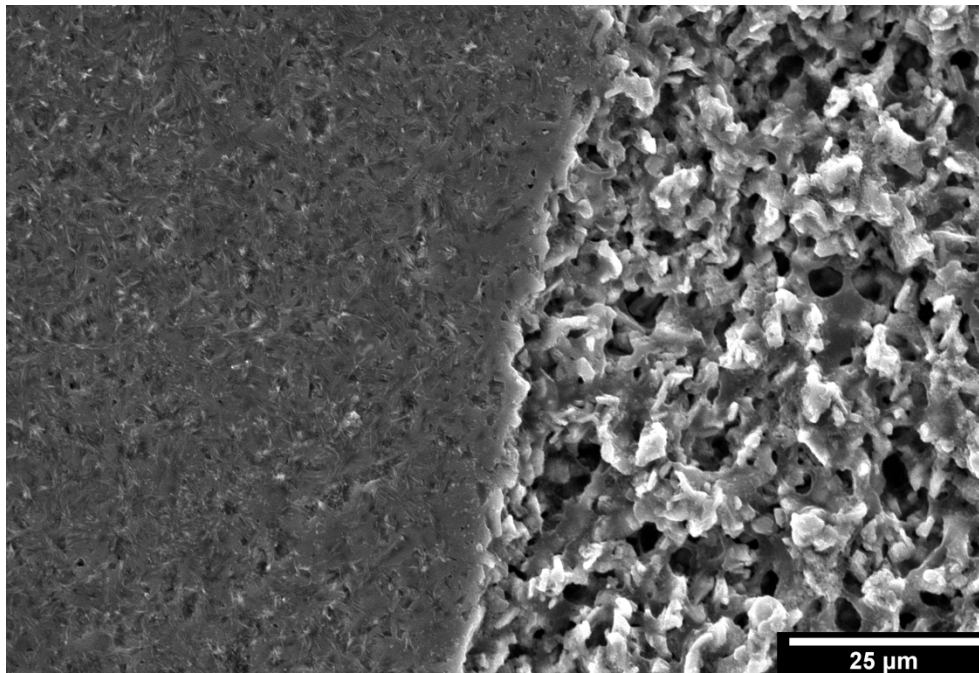


Figure 39: Duplex BASE tube using graphite as a pore former. The left side is the dense layer, and the right side is the porous layer.

The alternative, PMMA spherical powders, provided uniform spherical pores of 40 μm. These cast with a consistent settling pattern, which allowed for a mathematical approximation of the pore surface area (Figure 40). It should be noted, that even though the pores from the PMMA powders were significantly larger than that of carbon, there was less interconnectivity between pores. An additional issue with the PMMA spheres were that they settled much faster than beta-alumina or their carbon counterpart. This is evident by calculating their settling velocities in methanol (Table 7), using Stokes equation (Equation 5.7). Ultimately, the PMMA spheres provided a more consistent result and were used for the majority of the work.

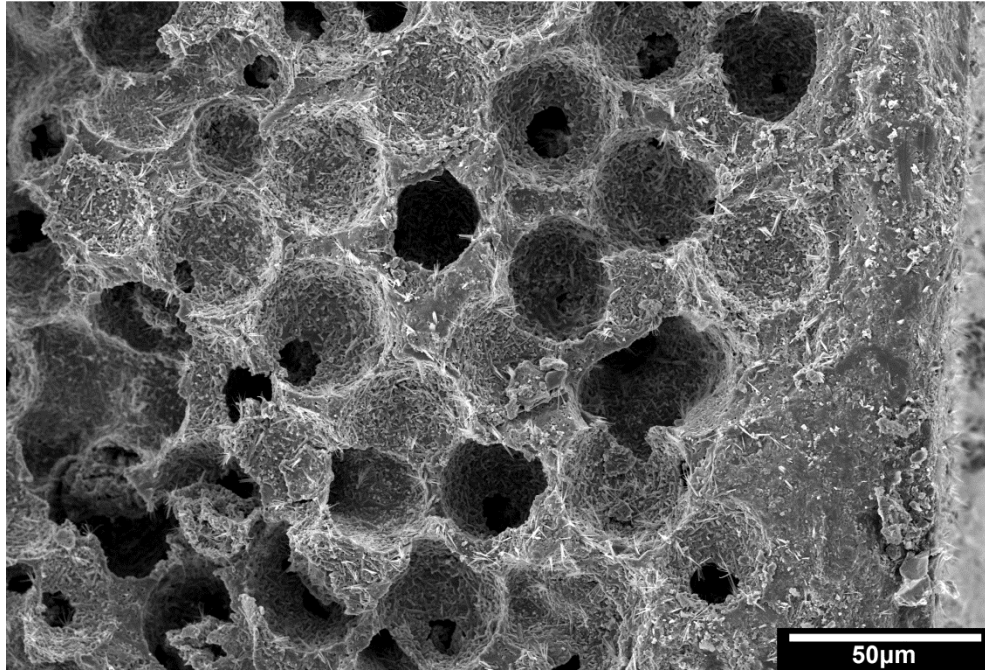


Figure 40: Duplex BASE tube using PMMA as a pore former. Large interconnected spherical pores (left) with a thin (~50 μm) dense layer (right).

Table 7: Terminal Velocities of Different Particles in Slip Casting Slurries.

	BASE (Fine)	BASE (Coarse)	Graphite	PMMA
Particle Diameter (μm)	1	10	10	40
Material Density (g cm^{-3})	3.3	3.3	2.27	1.18
Reynolds number	3.7×10^{-12}	3.7×10^{-9}	2.2×10^{-9}	3.7×10^{-8}
Settling Velocity ($\mu\text{m s}^{-1}$)	2.5×10^{-3}	2.5×10^{-1}	1.5×10^{-1}	6.3×10^{-1}

Stokes Law, and therefore Stokes equation, is limited to particle movement under laminar flow. It also assumes that collisions, or interactions between suspended particles, do not occur. It can be determined if a particle is experiencing laminar flow, by determining the Reynolds number (N_R) using Equation 5.8. Laminar flow occurs when the Reynolds number is less than 0.2, while turbulent flow occurs when the Reynolds number is greater than 0.2. All particles used in slip casting were under laminar flow, and their settling velocity can be compared. It is seen in Table 7 that graphite and coarse BASE powders

have similar settling velocities, meaning that the suspension is not expected to segregate during slip casting. On the other hand, the PMMA powders are expected to significantly separate from the BASE powders during the casting process.

$$v_s = \frac{d^2(\rho_s - \rho_L)g}{18\eta} \quad \text{Eq 5.7}$$

$$N_R = \frac{vd_Lx}{\eta} \quad \text{Eq. 5.8}$$

In both Equations 5.7 and 5.8, v_s is the settling velocity (m s^{-1}), d is the particle diameter (m), ρ_s and ρ_L the densities of the particle and liquid (kg m^{-3}), g is the acceleration due to gravity, and η is the viscosity of the liquid ($\text{kg m}^{-1} \text{s}^{-1}$). In Table 7, methanol was assumed to be at 20°C, where the viscosity is $0.594 \text{ kg m}^{-1} \text{ s}^{-1}$, and its density is 790 kg cm^{-3} . It should be noted that rheological properties of methanol vary significantly with temperature, which will affect not only the stability of the slurry, but the casting rate during slip casting.

Internal Porosity vs External Porosity

The porous portion of the duplex tubes could be positioned either on the inside or outside of the tube. There were advantages and disadvantages to both options.

In the case of external pores, a thick porous section could be cast first, allowing for an ultra thin ($< 100 \mu\text{m}$) dense section to be subsequently cast. This was due to Darcy's Law, where the growth rate reduced with cast thickness. However, this casting method had a

few major flaws. Firstly, the PMMA particles from the porous layer could become resuspended during the dense section casting step (Figure 41). These particles could then resettle and cause a pore within the dense section. Additionally, since the parts were cast in a pressed α -alumina powder mould, residual alpha powder would stick to the porous section. If this residual layer was not removed completely, it would convert to β -alumina at the surface, but would block the porosity of the tube, resulting in excessive resistance (Figure 42). This was tested, and confirmed, by casting a “triplex” part with the porous section sandwiched between two dense sections, and titrating sodium through the cell. Lastly, the porous section of the tube would not be in contact with pure sodium, but rather the tin-sodium bath. This meant that infiltrating the pores of the external tubes would be even more difficult than for internal porosity.

On the other hand, the internal pore configuration had the reverse issues. Since the dense section was cast first, the chance of defects due to PMMA impurities was reduced. However, the dense sections produced were much thicker than 100 μm , usually around 0.5 to 0.9 mm. This had to be done to protect the dense section from being polished away during the cleaning step. An aggressive cleaning regime would damage a thin dense section, cracking or eroding it away. A thick dense section impedes the process of producing thicker porous sections.

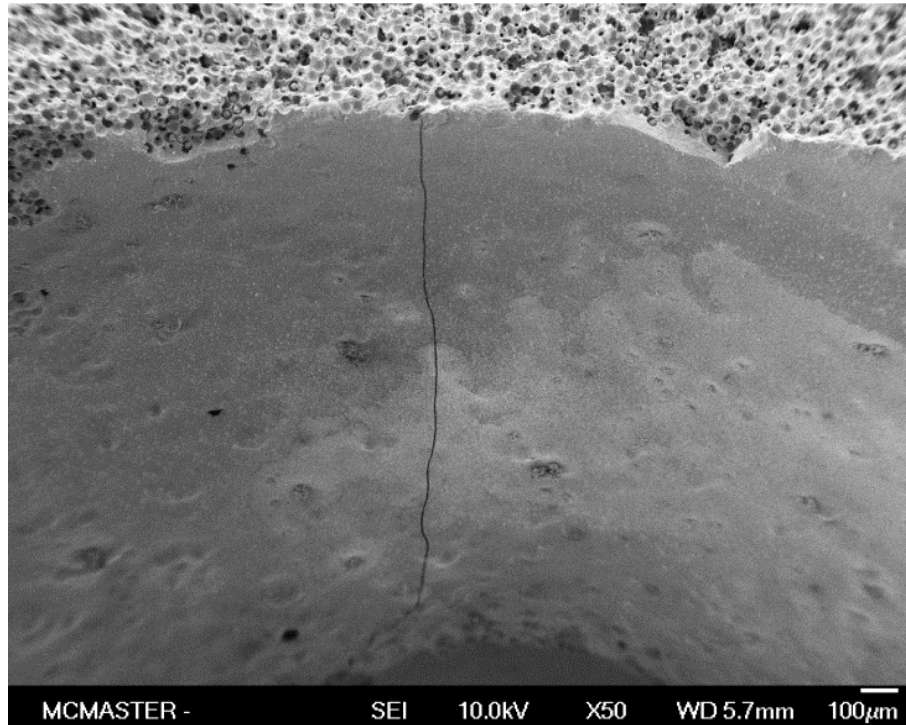


Figure 41: Porosity within dense layer of duplex BASE tubes due to the resuspension of PMMA powders during casting of dense slurry.

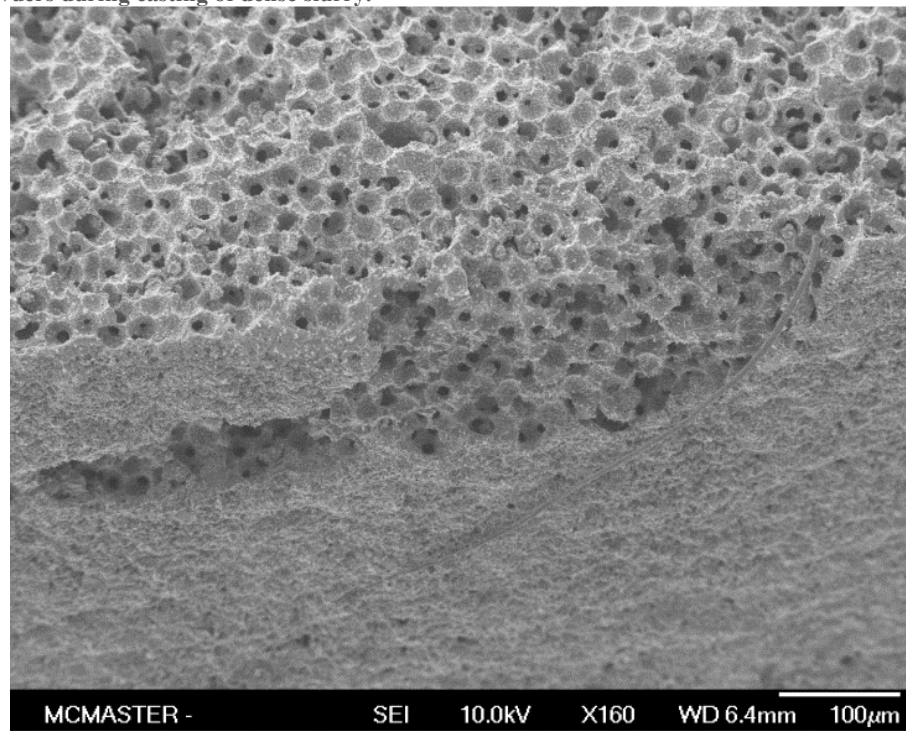


Figure 42: Blocked porosity due to improper cleaning of alumina mould powder.

Conductivity Measurements of Cells

Several cells were tested using the method outlined. The results were considered successful if the test cells, and their reference, showed no signs of sodium leakage during testing. When aggregating all the tests, it can be seen in Figure 43 that porous cells have a significantly lower resistivity profile than dense cells.

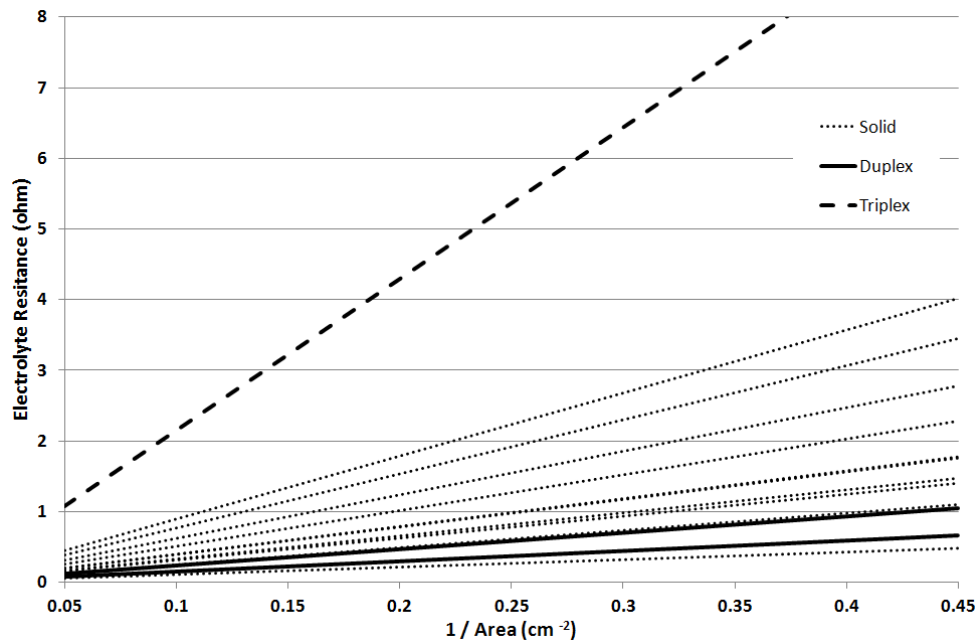


Figure 43: Resistivity profiles of BASE tubes as an inverse function of area.

Dense Electrolyte Cells

This section describes the experiments to distinguish the bulk and interfacial resistances of dense electrolyte cells with a thickness ranging from 0.8 to 1.25 mm. This range was chosen due to production considerations. Cells with a thickness of less than 0.8 mm were prone to damage and failure during the process of cleaning residual α -alumina, while cells thicker than 1.2 mm could crack, from internal stresses, at any step during the production

process. A total of 10 dense cells were successfully tested, providing an unusually broad distribution of resistivities. The results are tabulated in Table 8, alongside the cell thickness.

Table 8: Lines of Fit for BASE tube conductivity tests

Cell ID	Cell Thickness [cm]	Best Fit Slope (Intercept)
Tb 179	0.080	7.410 (+ 0.952)
Tb 193	0.092	2.979 (- 0.302)
Tb 181	0.094	2.431 (- 0.074)
Tb 192	0.094	1.723 (+ 0.169)
Tb 185	0.108	3.787 (+ 0.072)
Tb 197	0.108	3.811 (+ 1.588)
Tb 176	0.111	8.684 (- 0.478)
Tb 174	0.116	7.970 (- 0.549)
Tb 187	0.120	4.919 (+ 0.471)
Tb 186	0.125	3.155 (+ 0.362)

Using Equations 5.5 and 5.6, each cell was compared to all others to resolve the bulk conductivity (σ) and interfacial resistance (χ) of tubes made by the sol-gel process. In many cases, the interfacial resistance calculated when comparing different cells resulted in a negative number. However, four cell couples returned positive values for both χ and σ . Additionally, the bulk conductivities calculated were within 1 order of magnitude of bulk conductivities reported in literature.

The four cell couples that provided positive results were 174/179, 176/179, 181/186 and 186/193. In the case of 174/179, the interfacial resistance was found to be 6.17 ohm cm² with a bulk conductivity of 6.43x10⁻² S cm⁻¹. This represented the highest calculated area

specific interfacial resistance, as well as the lowest bulk conductivity. The cell couple 186/193 had the highest bulk conductivity ($1.88 \times 10^{-1} \text{ S cm}^{-1}$), but not the lowest interfacial resistance ($2.59 \text{ } \Omega \text{ cm}^2$). The 181/186 couple had the lowest interfacial resistance (0.24 cm^2). The results are found in Table 9. All other cell couples provided either a positive σ with a negative χ , or vice versa, and were not used.

Table 9: Bulk & Interfacial conductivities of solid BASE tubes

Cell Couples	$\chi \text{ (}\Omega \text{ cm}^2\text{)}$	$\sigma \text{ (S cm}^{-1}\text{)}$
174/179	6.17	6.43×10^{-2}
176/179	4.12	2.43×10^{-2}
181/186	0.24	4.28×10^{-2}
186/193	2.49	1.88×10^{-1}
Average	3.38	7.99×10^{-2}

Using the average bulk conductivity, the interface resistance of all the other dense cells were calculated. This resulted in a range of interfacial resistances from 0.55 to $7.29 \text{ } \Omega \text{ cm}^2$. The average interfacial resistance was calculated as $3.38 \text{ } \Omega \text{ cm}^2$ with a standard deviation of $2.46 \text{ } \Omega \text{ cm}^2$.

Figure 44 shows the plots of two cell couples. It is important to notice that the error, both in the X-axis and the Y-axis, generally increased as the area of contact decreased. The error in the Y-axis was due to an amplitude increase of the noise level during the test. The error in the X-axis was primarily due the uncertainty in the dipping of the electrode into the bath.

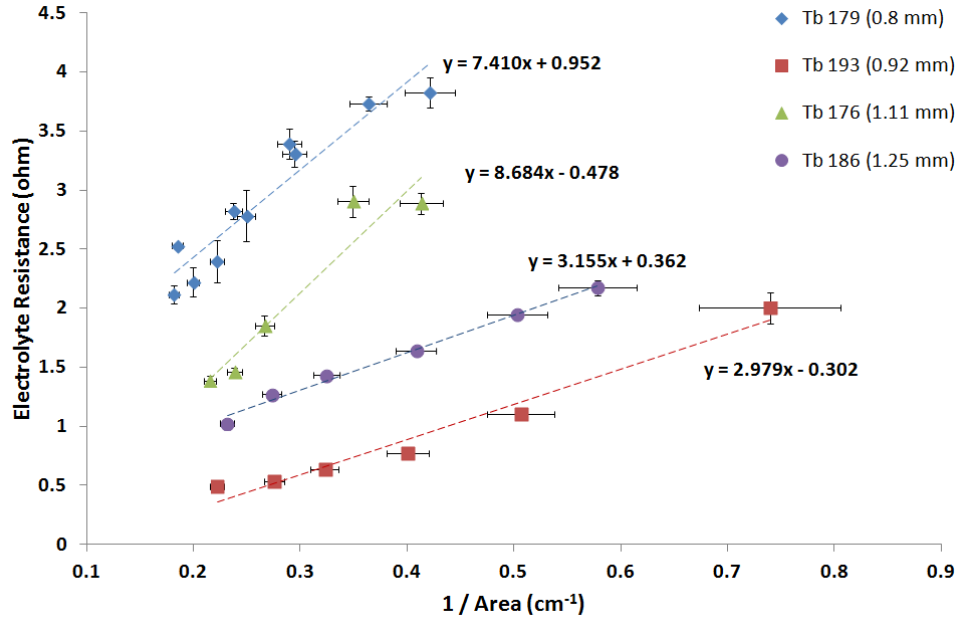


Figure 44: Resistance profiles of dense tubes as a function of area submerged into tin-sodium bath.

Duplex Electrolyte Cells

The duplex cells were tested identically to the dense cells. Of the twelve duplex cells successfully produced by slip casting, only two produced linear relationships, as these cells were just as prone to failure as dense cells. These two cells are presented in Figure 45. The slopes of both cells were significantly lower than the dense cells, with the exception of the dense cell Tb 192. Using the bulk conductivity values from the dense electrolyte, the interfacial resistances of the duplex cells were calculated (Table 10). The thickness of the dense layer in both duplex BASE tubes was approximately 0.8 mm. For the average σ of $7.99 \times 10^{-2} \text{ S cm}^{-1}$, the average interfacial resistance of the duplex cells was found to be $0.83 \text{ } \Omega \text{ cm}^2$. This represents a reduction of the interfacial resistance by 75%.

Tape cast duplex cells produced by Kim et al., using a different pore former, showed a reduction of interfacial resistance of 43%, when compared to traditional cells [39].

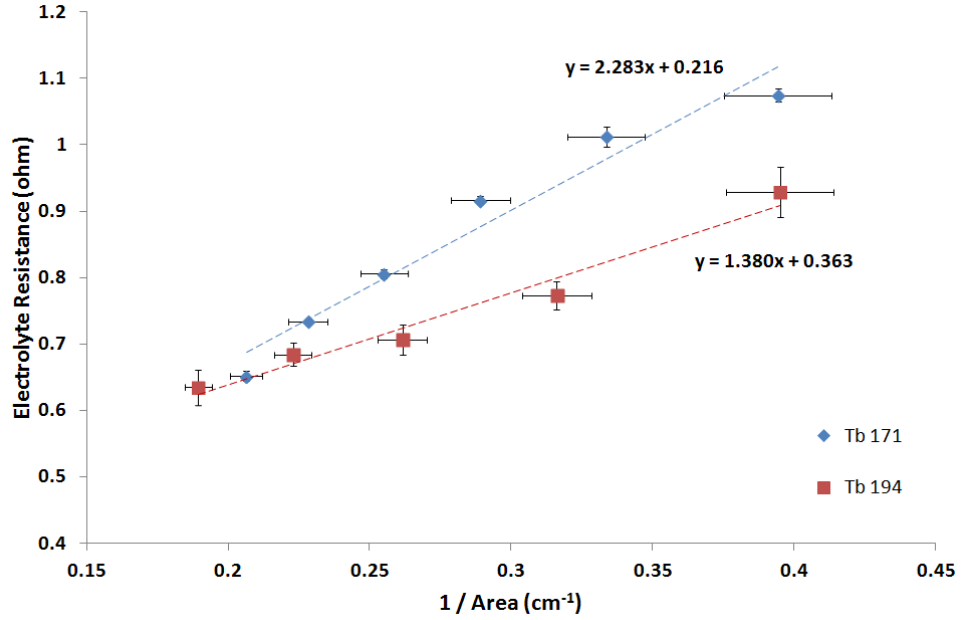


Figure 45: Resistance profiles of duplex tubes as a function of area submerged into tin-sodium bath.

Table 10: Calculated interfacial resistance (χ) of Duplex BASE tubes using bulk resistance calculated by dense BASE tubes.

Cell ID	Cell Thickness Dense [cm]	Best Fit Slope (<i>Intercept</i>)	Calculated χ from σ				
			2.43×10^{-2}	4.28×10^{-2}	6.43×10^{-2}	1.88×10^{-1}	7.99×10^{-2}
Tb 171	0.08	2.283 (+ 0.216)	-1.01	0.41	1.04	1.86	1.28
Tb 194	0.08	1.380 (+ 0.363)	-1.91	-0.49	0.14	0.95	0.38

Experiment Design Failures

A large amount of the errors encountered during this project were due to the nature of β - and β'' -alumina, as well as some experimental considerations. The assumption that the batch sol-gel process would produce consistent β - and β'' -alumina was, at best, misguided. Literature had shown that the conductivity of BASE could vary significantly between cells of identical composition. One major contributor to this variance was the grain size of the final products. Significant error was introduced here due to ball milling required to reduce the particle size of the BASE powder such that it could be suspended in methanol. The particle size of the powder was difficult to control, and ball milling introduced an unknown amount of ZrO_2 into the tubes.

Experimentally, a significant number of design flaws worsened the quality of the data. Firstly, working within a glovebox added significant errors. The cells needed to be lowered approximately 40 cm into a recessed chamber. Combining this with the fact that the exact height of the tin-sodium bath was difficult to measure, the depth of the dip had a significant error. This error also had to take into account the wetting angle of the tin-sodium bath on the BASE tube. The tubes were only a few centimeters in length, and were immersed to depths of 1 to 2 cm, with an error of 0.5 mm.

Lastly, due to the limitations of slip casting with the sol-gel material, cells with wall thicknesses between 0.8 and 1.2 mm were produced. This narrow range of wall thicknesses could be considered too narrow to be experimentally significant. This is

especially important in determining the χ and σ . This could be avoided if much thicker (2 mm or more) cells were produced, allowing for the expressions to hold true.

Conclusion of β -Alumina Solid Electrolyte Conductivity Testing

Surface modification of the BASE through porous support was shown to reduce the effective interfacial resistance when compared to the fully dense cells. This reduction was calculated to be approximately 75% of the resistance of a cell with a smooth interface. This reduction in resistance, combined with the thinning of the dense portion, could be used to produce ultra-thin duplex cells with very low interference.

Chapter 6: Sodium Silicide and Na-Si Binary System

The properties of sodium silicide have not been well defined in literature. This was primarily due to the near-universally reactive nature of its components. The crystal structure of sodium silicide has been well documented to be monoclinic (C2/c space group) at room temperature and below. The theoretical density of this phase is 1.746 g cm⁻³. An allotropic transformation occurs at 612°C, however, no further examination of this phase has been done to date. At this time, no other physical or thermodynamic properties have been reported, with the exception of an EMF study of the Na-Si system by Mali et al. in 2013.

This work explores the NaSi phase to characterize it further. The conductivity of NaSi was tested from room temperature to 750°C, by using a 4-point technique to measure resistance during the synthesis of NaSi. An autoclave was designed to provide a stable sodium vapour atmosphere, to allow for the phase to melt rather decompose. High temperature XRD analysis was attempted to find and characterize the change in crystal structure. The heat of formation of NaSi from elements was also measured using DSC in a customized cell. At the same time, the heat of transformation during the allotropic phase change was measured. The EMF from Mali et al. was revisited to confirm the low sodium activity reported. Finally, from the data above, a new Na-Si phase diagram was modelled using FactSage.

Electronic Conductivity

The conductivity of NaSi was measured for a sample made by reacting sodium and silicon in situ, as all attempts of melting pre-reacted NaSi were unsuccessful. As stated in Chapter 3, the conductivity was measured by a 4-point method, using a handcrafted vessel. Silicon and sodium were loaded into the crucible in two ways to determine the better one. In the first, sodium was placed at the bottom of the crucible, with silicon on top (synthesis cell) in stoichiometric amounts to form NaSi. In the second configuration, excess sodium was placed on top of the silicon (reverse cell).

The synthesis cell produced a NaSi slab bridging a void the length of the vessel. Additionally, the slab was prone to have large pores and cracks where sodium globules were present at the beginning of the synthesis. This made conductivity measurements more erratic as an unknown number of unseen surfaces increased the uncertainty of the sample geometry, as well as increasing the chance of breakage during temperature changes (Figure 46). The reverse cell configuration (Si on the bottom) was used for subsequent tests.

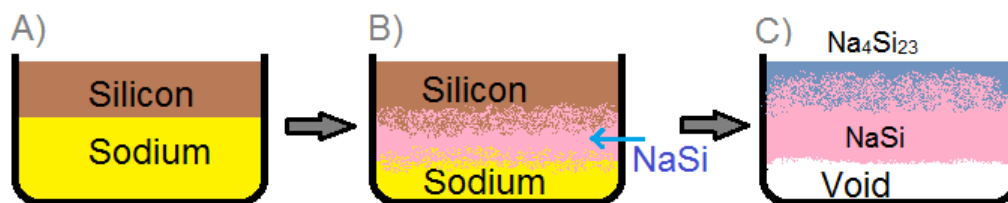


Figure 46: Reaction of sodium and silicon to form NaSi in a "synthesis" cell.

In the reverse cell, the silicon was placed beneath an excess amount of sodium ($x_{\text{Na}} \sim 60$ to 80 at%). This prevented the formation of the void and produced only one uncontrolled interface. Additionally, from an interrupted cell, it was seen that the silicon dissolved readily in the excess sodium. This Na-Si liquid was concentrated through sodium evaporation (Figure 47). The downside of this configuration was that the sodium needed to be evaporated, prolonging the tests. Using this configuration, contiguous slabs of NaSi were produced, and conductivity data were gathered.

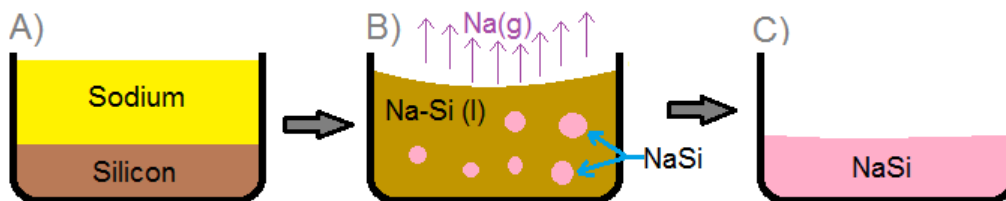


Figure 47: Reaction of sodium and silicon to form NaSi in a “reverse” cell.

Table 11 contains the measured conductivities of NaSi at five different temperatures over the course of three successful tests. The conductivity measurement at 750°C was estimated during a fourth successful test. However, the reading was highly unstable due to the rapid decomposition of NaSi at temperatures above 600°C. The conductivity values were calculated, using Equation 6.1, by taking the resistance of the NaSi at a stable plateau at each individual temperature. It was assumed the slab produced by the reverse configuration was uniform in shape, and that the NaSi had very low porosity ($\rho_{\text{NaSi}} = 1.7 \text{ g cm}^{-3}$).

$$\sigma_{\text{NaSi}} = \frac{L_{\text{Probe}}}{A \times \left(\frac{V_I - V_{\text{OCV}}}{I} \right)} \quad \text{Eq. 6.1}$$

$$A = \frac{\left(\frac{m_{\text{Si}}}{\text{MW}_{\text{Si}}} \times \frac{\text{MW}_{\text{NaSi}}}{\rho_{\text{NaSi}}} \right)}{L_{\text{Crucible}}} \quad \text{Eq. 6.2}$$

Here L_{Probe} is the distance between the voltage leads, V_I the voltage while current (I) is applied, and A the cross section of the NaSi slab, as derived by Eq. 6.2. V_{OCV} was taken to be 0 V. L_{Crucible} is the length of the containing crucible. The entire length is considered, as the Na-Si liquid is expected to fill the full length of the crucible before NaSi starts forming.

Table 11: Conductivity of NaSi

Temperature (°C)	Conductivity (S cm ⁻¹)
280	0.393
330	0.470
430	0.700
550	6.21
650	21.1
750	48.1

The results of the conductivity measurements showed temperature dependence characteristic of semiconductors. The exponential nature can be reported in the form $\ln(\sigma)$ vs $1/T$ to provide a linear plot (Figure 48). This linear dependence was obeyed for all but the lowest temperatures. There are two possible explanations for the deviation at lower temperatures. The first was the uncertainty of the measurement. The second was a change

in the transport properties of NaSi. Unfortunately, neither possibility could be substantiated with further experimentation.

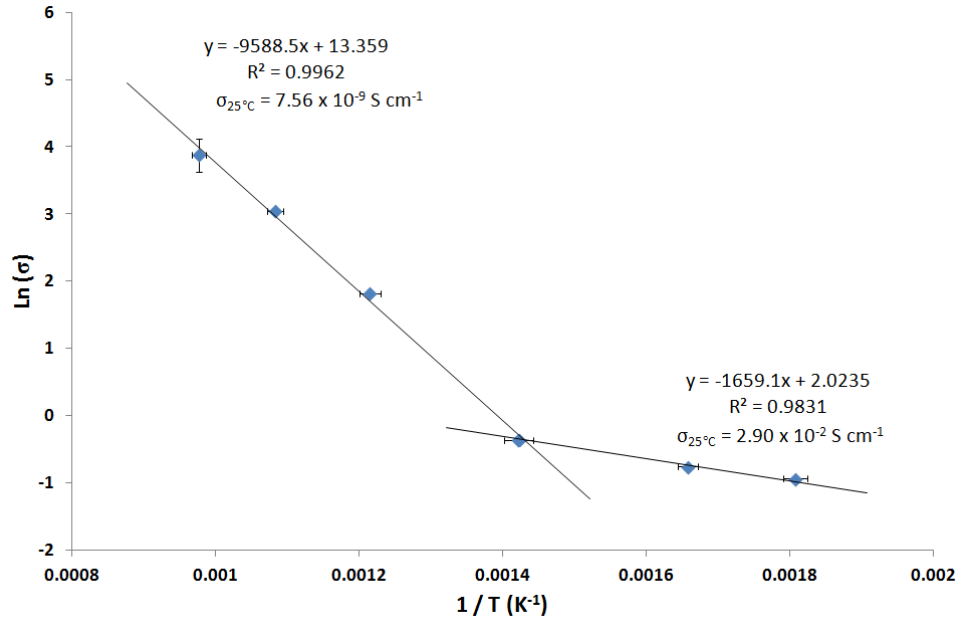


Figure 48: Conductivity of NaSi as an inverse function of Temperature.

Assuming that the low temperature readings were errors, and therefore ignored, the other four points were used to calculate the projected room temperature conductivity. The calculated conductivity using the linear fit, found in Figure 48, was on the order of 7×10^{-9} S cm⁻¹. This is inordinately low, similar to the conductivity of insulators. The similar compound, LiSi, has a conductivity of 1 S cm⁻¹ at room temperature [88].

The possibility of a change in the transport properties of NaSi is based on similar behaviour occurring in LiSi. In NaSi, the shift occurred somewhere between 330°C and 430°C, while it is observed closer to 180°C in LiSi [88]. The three coldest temperatures produced a high quality linear fit. Extrapolating this fit to room temperature gave a

calculated conductivity of $2.9 \times 10^{-2} \text{ S cm}^{-1}$. Room temperature resistance measurements of NaSi chunks showed conductivity between 10^{-2} and $10^{-1} \text{ S cm}^{-1}$.

The room temperature experiments were designed such that probes (diameter = 0.5 cm) were connected to parallel faces of NaSi chunks of differing thickness, as seen in Figure 49. Unfortunately, due to the reactive nature of the NaSi, machining was not possible. There was a possibility of electron scattering outside of the probe contact area. This scattering would be expected to be greater in thicker samples than thinner ones, reducing the conductivity of the sample. Additionally, defects such as faults and cracks were more common in thicker chunks, further reducing their apparent conductivity. As such, the resulting conductivities found in Table 12, have a high degree of error. The best estimate places the conductivity at room temperature within a range of 10^{-2} to $10^{-1} \text{ S cm}^{-1}$. The 2 mm thick sample showed an increased conductivity (1 S cm^{-1}) at low currents, but break down occurred at higher currents (Figure 50).

Table 12: Conductivity measurements of NaSi using chunks at room temperature

Sample Thickness	Conductivity (10 mA)	Conductivity (40 mA)
2 mm	1.1 S cm^{-1}	—
6 mm	0.12 S cm^{-1}	0.11 S cm^{-1}
15 mm	0.03 S cm^{-1}	0.025 S cm^{-1}

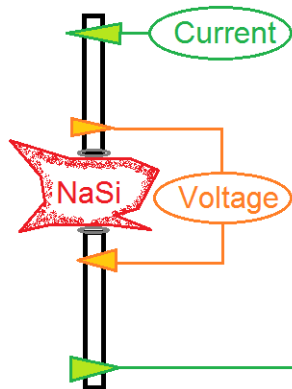


Figure 49: Four-point conductivity setup for room temperature measurements of NaSi

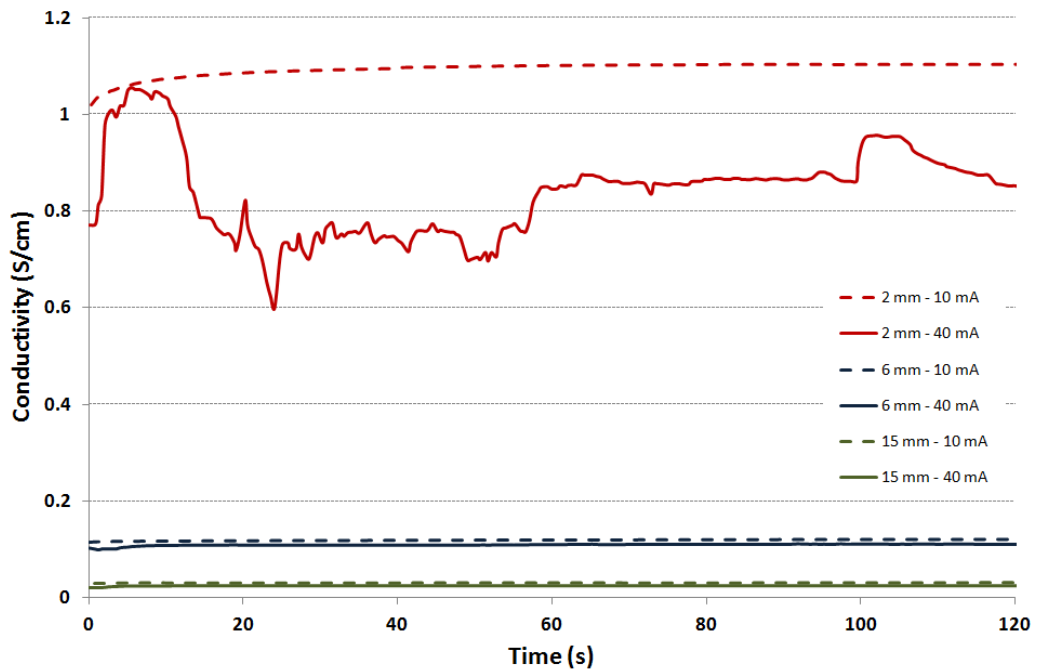


Figure 50: Conductivity of NaSi at room temperature using 0.5 cm metal probes.

The stability of NaSi made it difficult to obtain reproducible data. Due to the crude nature of the experiment and the reliance on sodium evaporation to produce pure NaSi, temperature control was critical. Figure 51 shows the result of the first successful conductivity test. It was expected that a plateau in conductivity would occur when the

sodium had fully evaporated, leaving NaSi behind. However the optimal temperature for this process to occur had not yet been determined. After nearly 20 hours at 550°C without any change in conductivity, the sodium vapour pressure was deemed too low to complete the process. The temperature was increased to 650°C, and the conductivity was seen to quickly drop as the excess sodium evaporated. The first plateau was observed at around 46 h. This plateau likely corresponded to the conductivity of pure NaSi. The test was continued, as at the time, the stability of NaSi was not yet known. Multiple new plateaus were shown, which were attributed to the continuous decomposition of NaSi to a NaSi-Na_xSi₁₇ mixture (52 – 57 h) and then further decomposition to a mixture of NaSi-Na_xSi₁₇-Si (57 – 67 h).

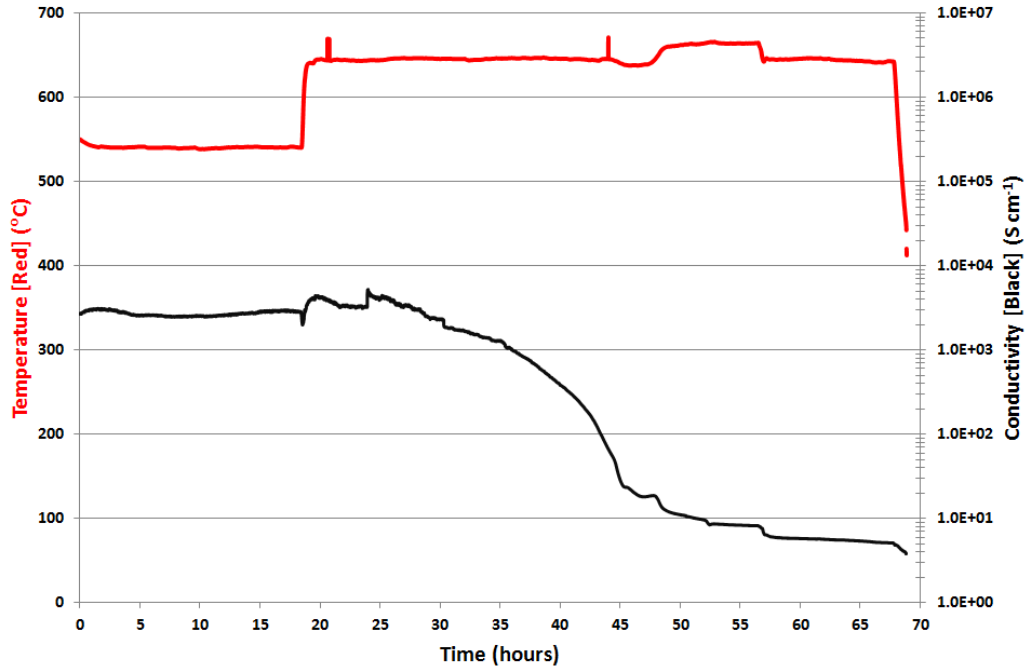


Figure 51: Conductivity measurements of NaSi at elevated temperatures (650°C).

The boat was removed from the tube furnace, and a sample of the product was transferred to the glovebox to prepare it for XRD analysis. The product was crushed and placed into a glass capillary, which was then sealed with vacuum grease. The XRD phase analysis showed that the sample had indeed partially decomposed to NaSi, $\text{Na}_x\text{Si}_{17}$, and Si. TOPAZ was used to quantify the amount of each phase based on peak intensity. It was found that it was composed of approximately 72% NaSi, 26% $\text{Na}_x\text{Si}_{17}$ and less than 2% elemental silicon.

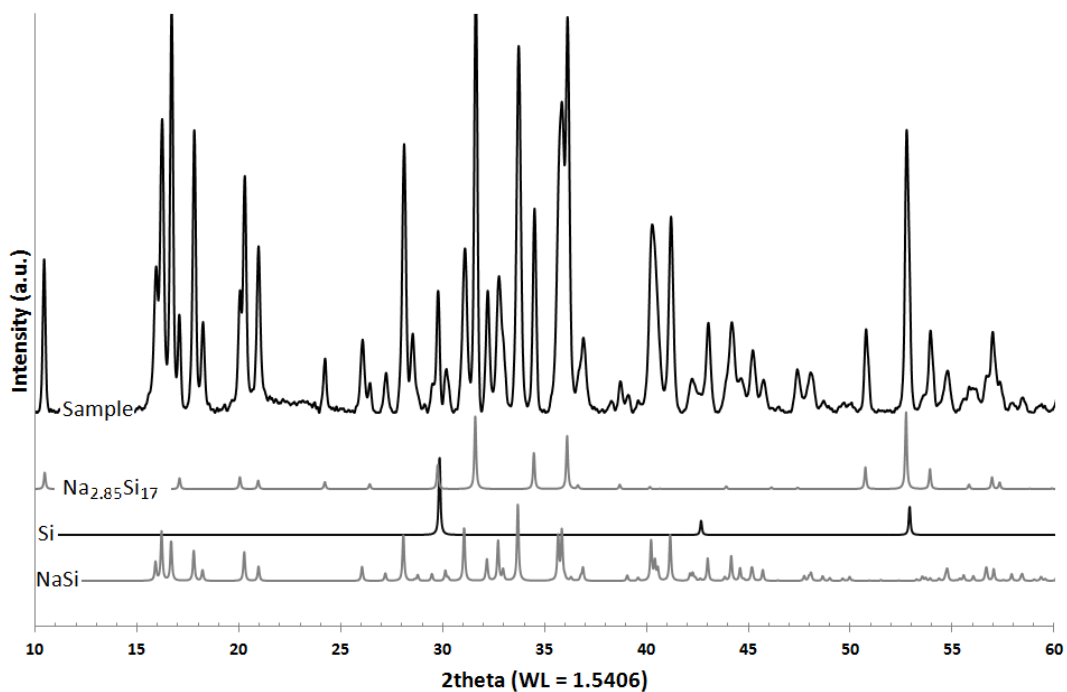


Figure 52: XRD phase analysis of resulting powder from first 650°C NaSi conductivity experiment.

The next successful test was an extended reaction at 550°C. The purpose of this test was to ascertain both the conductivity of NaSi at 550°C, and to determine an upper temperature at which NaSi was stable for an extended period of time. Much like the

previous experiment, the evaporation of sodium was slow. However, unlike the previous experiment, the plateau at the end of the test was stable for approximately 7 hours (Figure 53). The XRD analysis showed that NaSi was the dominant phase, with fewer than 2% of excess sodium (Figure 54). This temperature was taken as the stability limit to form NaSi within the experimental setup. Extended testing at temperatures below 550°C was deemed safe and reliable.

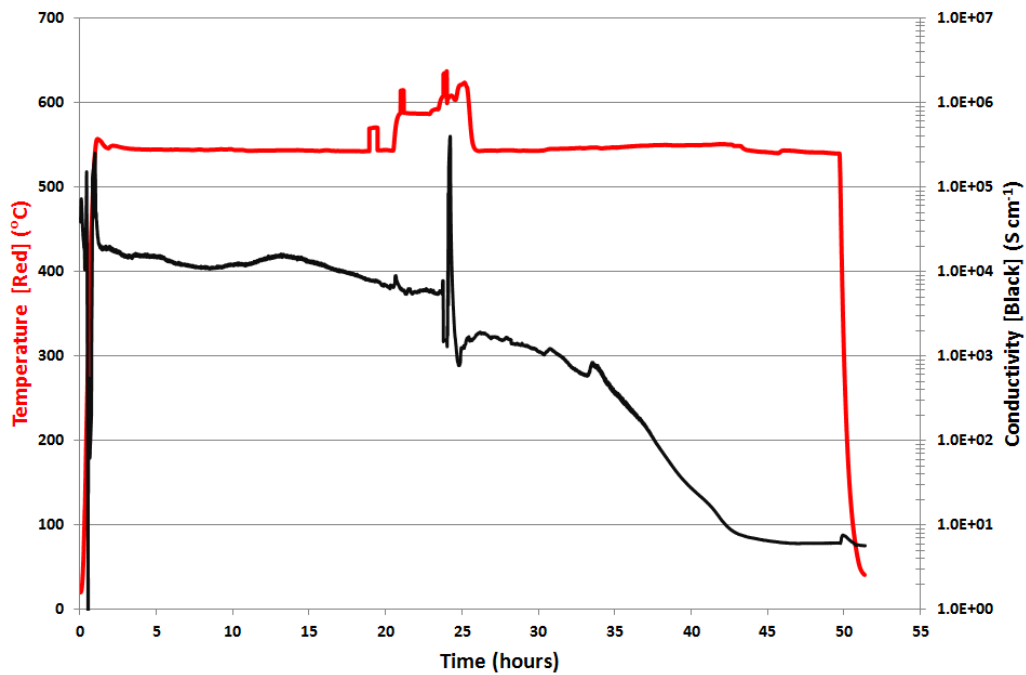


Figure 53: Conductivity measurements of NaSi at elevated temperatures (550°C).

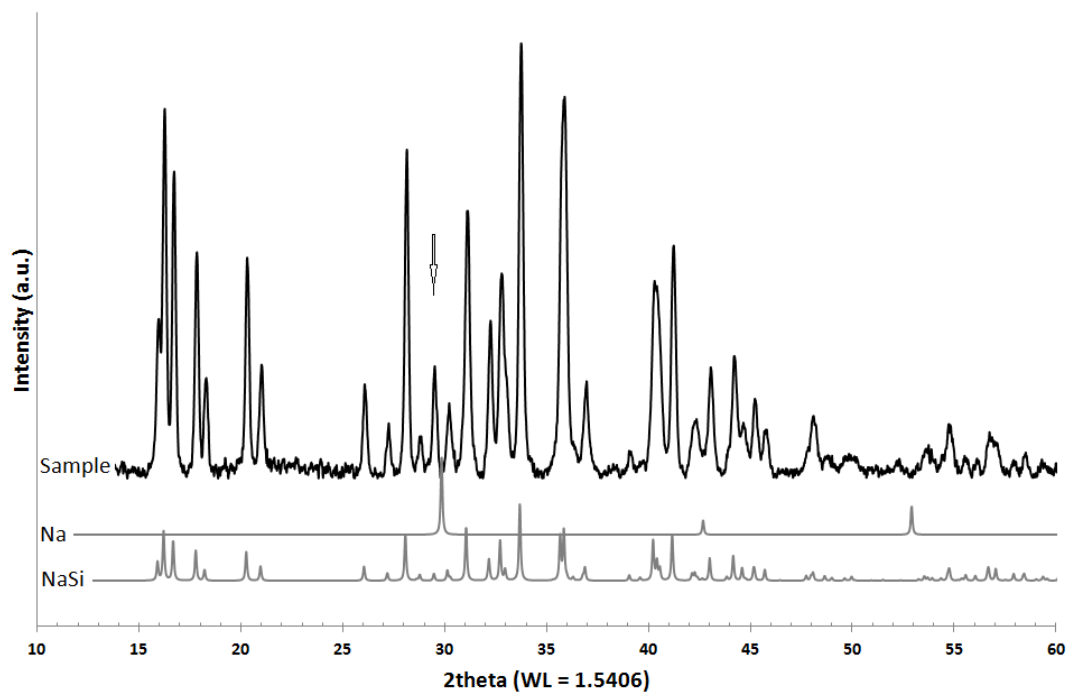


Figure 54: XRD phase analysis of resulting powder from 550°C NaSi conductivity experiment.

The previous two experiments provided the required understanding to continue with the test that provided the majority of the data. In this test, the sodium-silicon mixture was heated at 650°C until the plateau appeared. It was held for approximately 1 hour, and then furnace cooled to 430°C where NaSi was expected to be stable (Figure 55). Stable conductivity plateaus at different temperatures at or below 430°C were achieved (Figure 56). The XRD analysis confirmed that the process produced NaSi without detectable excess sodium, silicon or silicon clathrates (Figure 57).

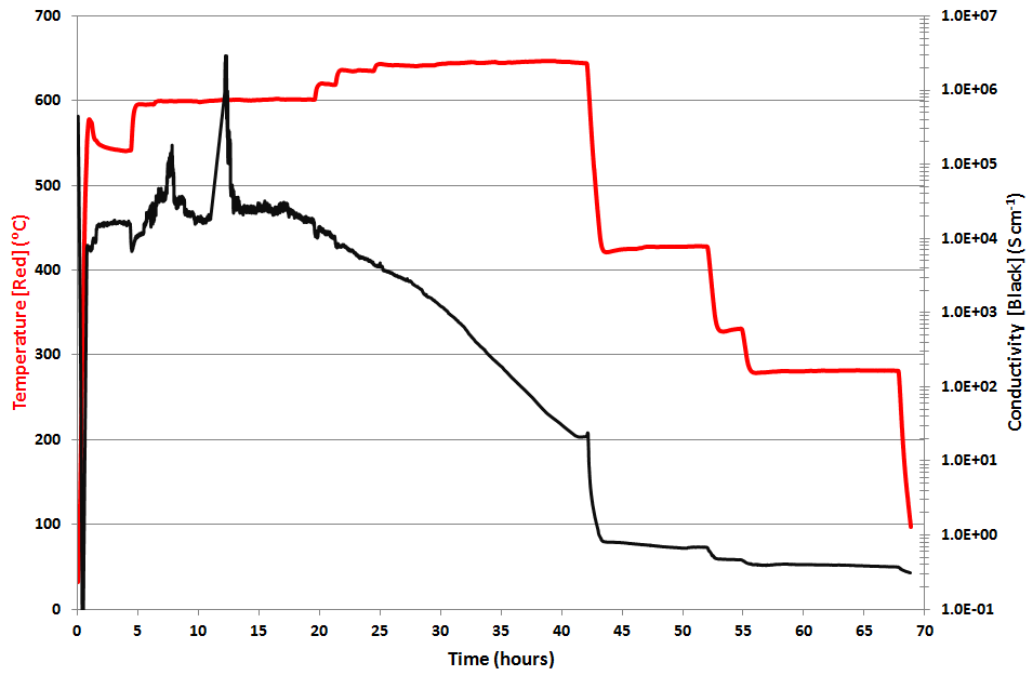


Figure 55: Conductivity measurements of NaSi at elevated temperatures; reacted at 650°C and cooled down for multiple measurements.

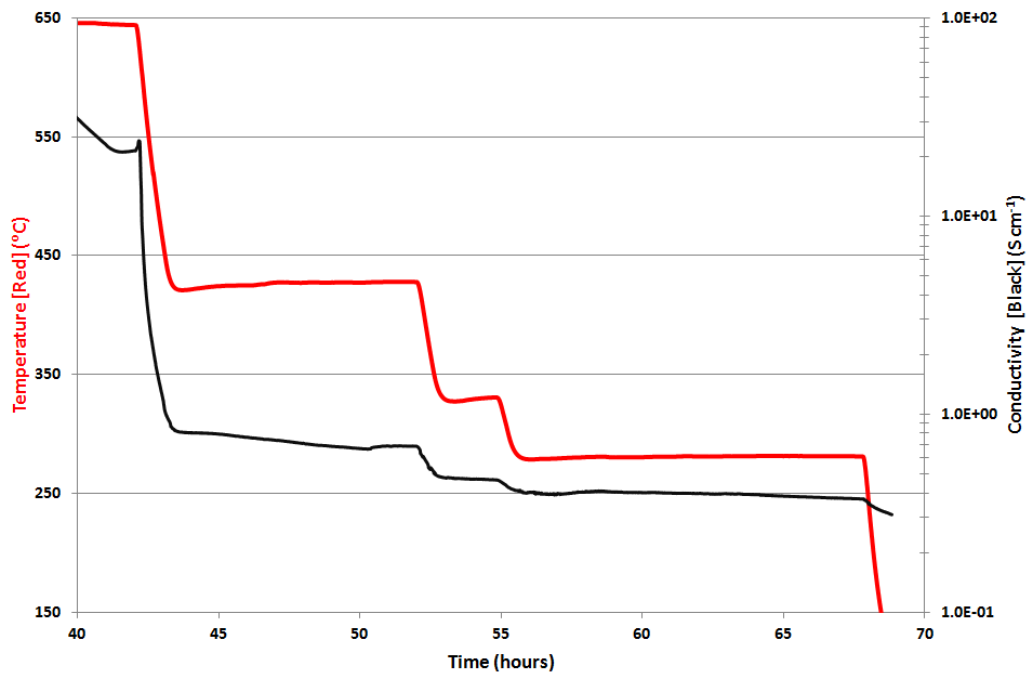


Figure 56: Close up of stability plateaus for step-down cooling of NaSi.

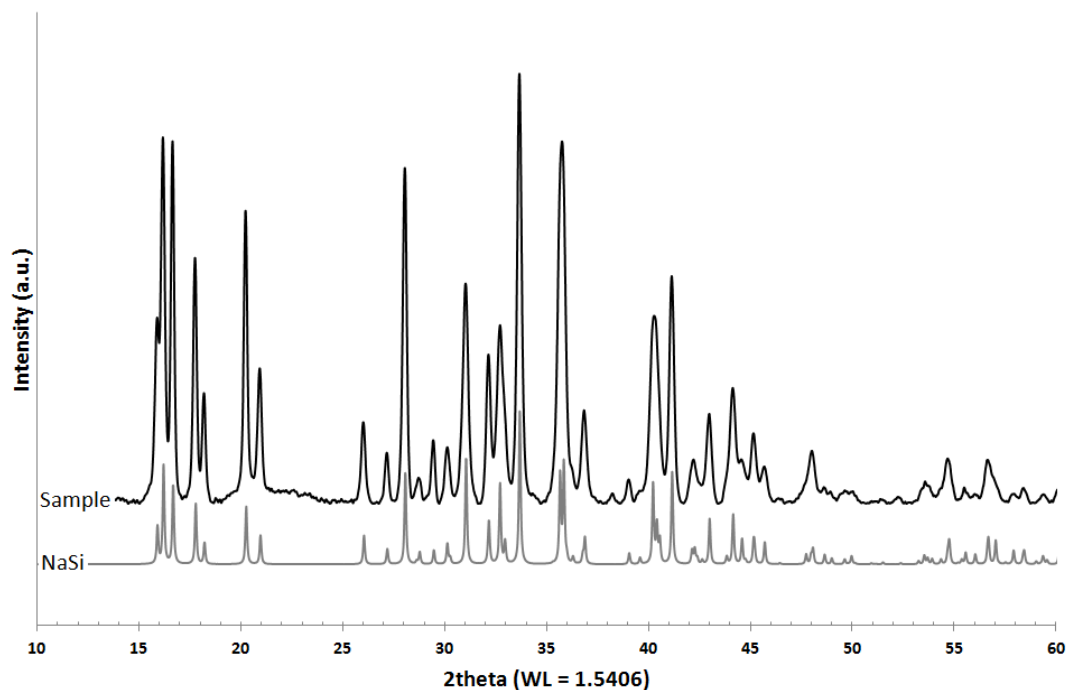


Figure 57: XRD phase analysis of resulting powder from NaSi conductivity experiment with cooling steps.

A final test was done in an attempt to determine the conductivity of NaSi at an elevated temperature. At 750°C, the vapour pressure of sodium is significant (28.5 kPa) and sodium will rapidly escape. As such, the cell was heated to 600°C for approximately 24 hours to allow for a complete reaction of sodium and silicon. The cell was heated to 750°C and the conductivity recorded until a plateau was detected (Figure 58). This plateau should occur once the excess sodium was evaporated, but it was not expected to be stable for very long since NaSi was already known to decompose to either elemental or silicon clathrate form.

After 34 hours, the first sudden shift in the slope was detected, with a second shift occurring about 30 minutes later. The first shift was due to the evaporation of sodium, where the sodium-silicon liquid bath transitions to solid NaSi and sodium liquid. The second shift in the curve occurred when the sodium was completely evaporated and the NaSi started to decompose into elemental Si or clathrate phases. The last plateau at the end of the test was attributed to the remnants of the reactions, which were stable at 750°C. The conductivity of NaSi at 750°C was estimated to be somewhere between the first and second shift in conductivity (Figure 59).

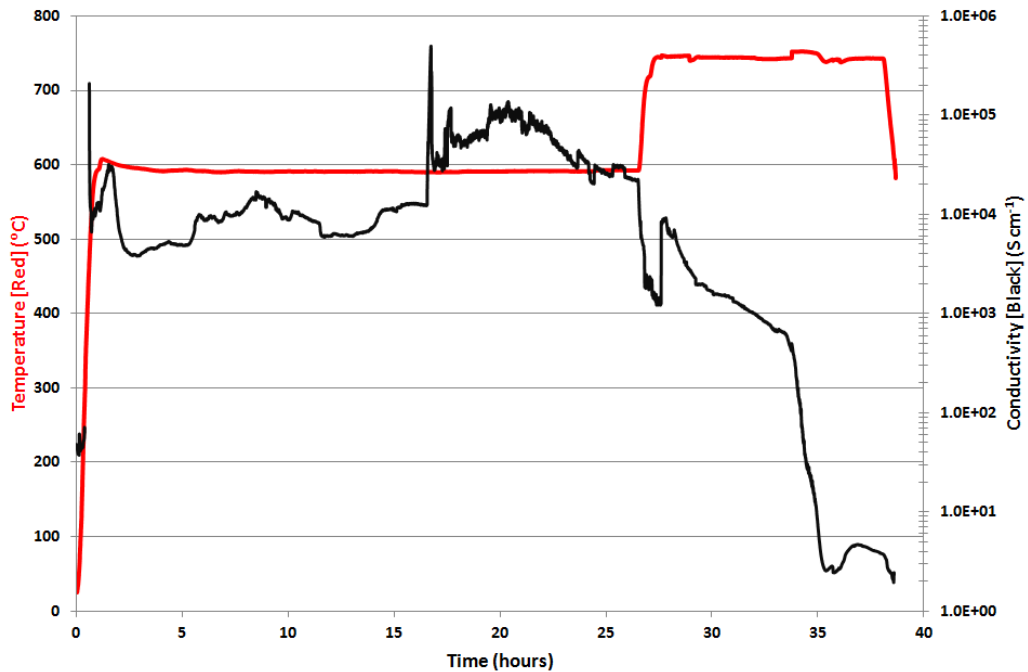


Figure 58: Conductivity measurements of NaSi at elevated temperatures (750°C).

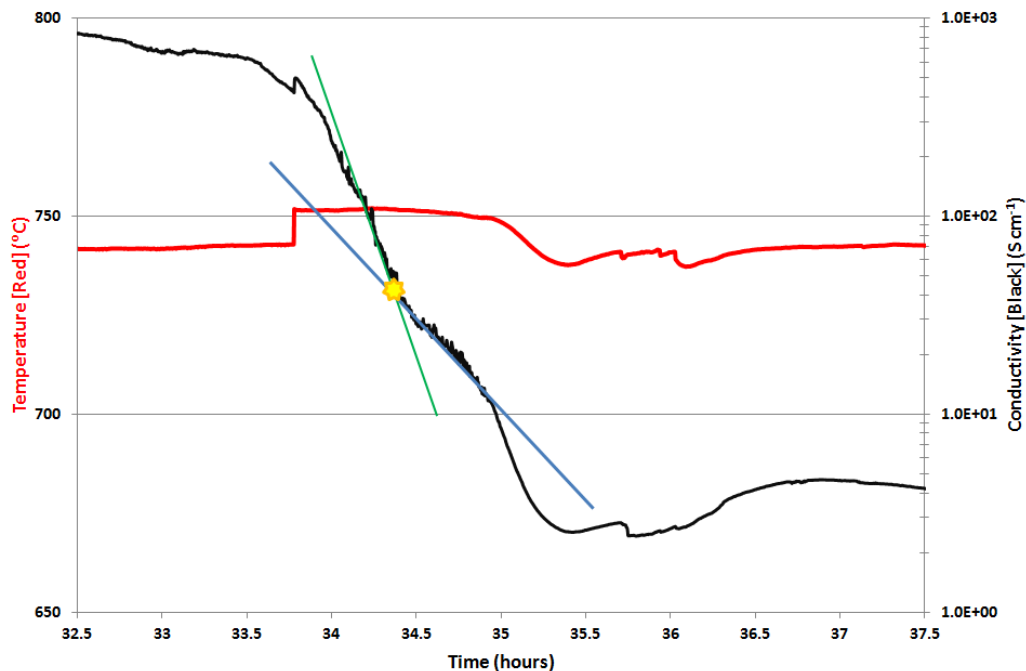


Figure 59: Estimation of the conductivity of NaSi at 750°C, based on the shift in slope during the conductivity measurement.

Shortcomings of Conductivity Measurements

The NaSi conductivity measurements were complicated due to material incompatibility issues. Although the boat itself was resistant to NaSi and its base elements, much of the circuitry was susceptible to reaction. Copper and steel wiring, as well as the current collectors reacted with silicon. The presence of chromium and iron silicides was confirmed by XRD analysis of the NaSi around the current collectors (Figure 60). Circuitry failures were the primary reason for termination of individual conductivity tests.

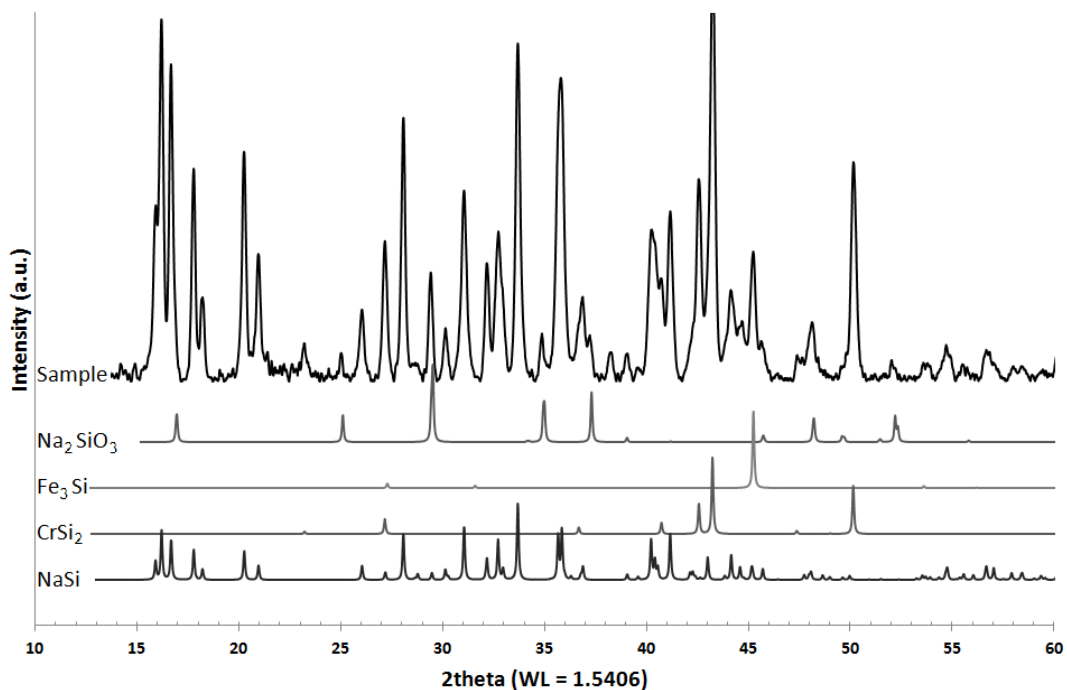


Figure 60: XRD phase analysis of NaSi near electrode (stainless steel or chromium).

Autoclave Melting

The purpose of the autoclave experiment was two-fold. The first was to melt NaSi into cylindrical rods for conductivity measurements, while the second was to help determine the melting point of NaSi. The NaSi granules were placed inside thin alumina crucibles, which isolated it from the steel autoclave. The crucibles were backfilled with argon gas at normal temperature and pressure. The volume of the autoclave was approximately 15 cm³, which can hold 3.6 mg of sodium vapour, when the partial pressure of sodium over the NaSi was 1 atm. Filled autoclaves were heated to temperatures between 1073 K and 1173 K, and held for at least 30 minutes to equilibrate. At these temperatures, the pressure

inside the autoclave increased up to 5 atm: 4 atm from the argon, and 1 atm from sodium vapour. The experimental parameters are found in Table 13.

The sample A1, which was heated to 850°C, exhibited partial melting. Figure 61 shows a portion of the NaSi powder seemed to have formed a liquid. The experiment was repeated from 800°C (A2) to 840°C (A6) in an attempt to identify the melting point. These samples did not seem to exhibit significant signs of melting compared to A1. Sample A7 was heated to 880°C in an attempt to fully fuse the NaSi. Unlike A1, the NaSi did not melt. Therefore, the melting point of NaSi could not be identified as the sample retained its original shape and porosity. The likely explanation for the melting seen in A1 was that significant excess unreacted sodium remained in the material used, as it is reported by the manufacturer.

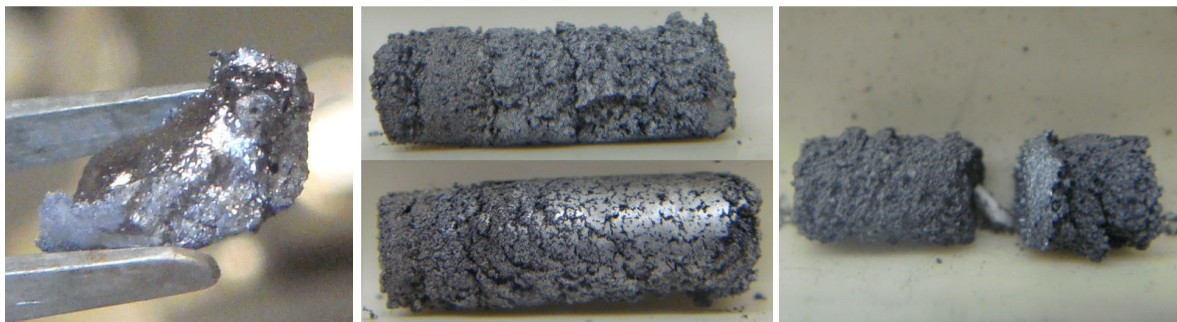


Figure 61: Image of autoclave samples Left) A1, Middle) A6, and Right) A7.

Samples A8 and A9 were tested using a mixture of powders and small granules of NaSi. The granules of NaSi were several millimeters in size. These were placed at the bottom of the alumina crucible and the powder was placed on top. The rationale was that if NaSi powder decomposed prior to the chunks of NaSi at the bottom, they would provide a

sufficient sodium atmosphere to stabilize the NaSi phase for the larger chunks. However, as seen in the Figure 62, the NaSi chunks show no sign of melting.



Figure 62: Sample A9, post autoclave heating at 875°C.

In the last sample, A10, the atmosphere was buffered by introducing excess sodium outside of the crucible, such that vapour pressure of sodium over the NaSi would be much higher than that naturally found from NaSi alone. This, in principle, would have reduced the tendency of NaSi from decomposing. This sample was inserted into the furnace, preheated at 900°C and held for 30 minutes. The Figure 63 shows that the NaSi chunks, again, exhibited no signs of melting.



Figure 63: Sample A10, post autoclave heating at 900°C.

Samples A2 (800°C), A6 (840°C) and A7 (880°C) were extracted and tested by XRD analysis, presented in Figure 64. All three samples showed signs of decomposition, where

the initial composition of pure NaSi powder resulted in a mixture of NaSi, elemental silicon and Na₄Si₂₃. Approximately 31% of the NaSi decomposed to elemental silicon in A2, while only 27% of the NaSi decomposed for sample A7. Sample A6, on the other hand, decomposed to a mixture of 80.5% NaSi, 12.5% Na₄Si₂₃, and 7% elemental silicon. This, combined with the lack of physical evidence for melting, showed that NaSi was not stable at elevated temperatures, where it melted incongruently, or simply decomposed rather than melted. The discrepancy in the compositions can be explained by sampling errors. The NaSi near the free surface would decompose more rapidly than the NaSi near the bottom of the autoclave, as all of the sodium vapour would be supplied by the material at the surface. The exact position of the sampling was not recorded when XRD was performed. The phase analysis of the products was done using TOPAZ.

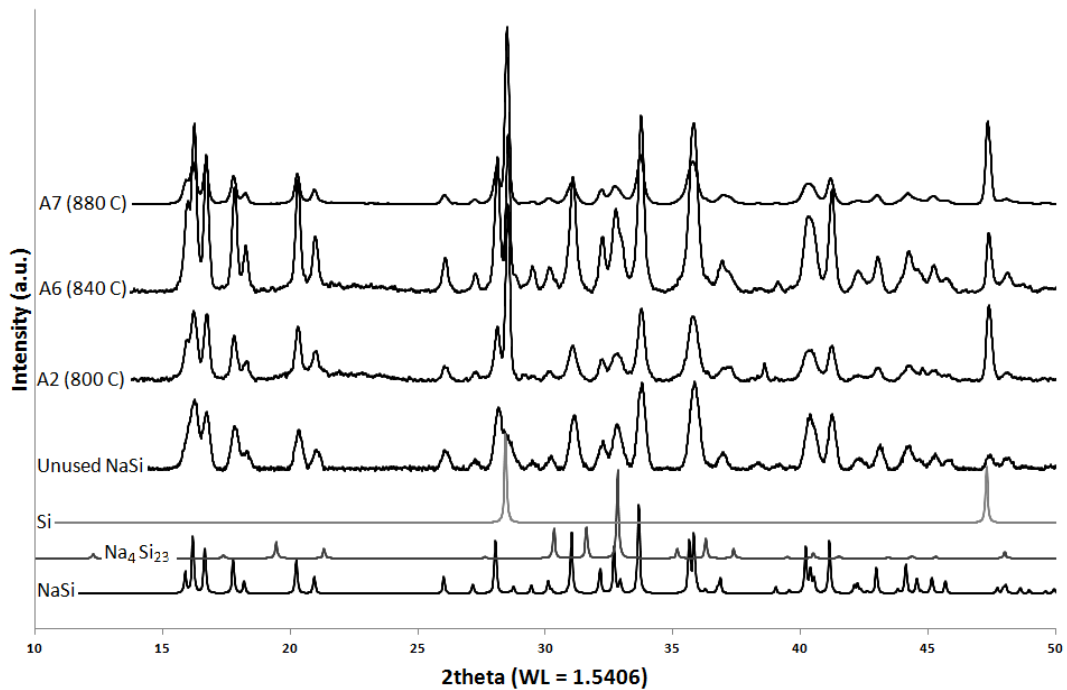


Figure 64: XRD analysis of NaSi powder prior and after autoclave heating (A2, A6, A7).

Table 13: Autoclave sample parameters

Sample #	Composition	Heating Profile	Experiment Notes
A1	~1 g NaSi	~25 C/min ramp to 850°C 15 min @ 850°C	Powder
			Melting
A2	0.494 g NaSi	~25 C/min ramp to 800°C 60 min @ 800°C	Powder
			No Melting
A3	0.495 g NaSi	~25 C/min ramp to 810°C 60 min @ 810°C	Powder
			No Melting
A4	0.502 g NaSi	~25 C/min ramp to 820°C 60 min @ 820°C	Powder
			No Melting
A5	0.525 g NaSi	~25 C/min ramp to 830°C 60 min @ 830°C	Pure Powder
			No Melting
A6	0.516 g NaSi	~25 C/min ramp to 840°C 60 min @ 840°C	Powder
			No Melting
A7	0.510 g NaSi	~25 C/min ramp to 880°C 60 min @ 880°C	Powder
			No Melting
A8	0.8 g NaSi	~25 C/min ramp to 820°C 60 min @ 820°C	Powder / Pieces
			No Melting
A9	0.75 g NaSi	~25 C/min ramp to 875°C 60 min @ 875°C	Powder / Pieces
			No Melting
A10	0.645 g NaSi 12 mg Na	Placed directly at 900°C 30 min @ 900°C	Powder / Pieces
			No Melting
A11	0.328 g Na 0.292 g Si	~25 C/min ramp to 880°C 60 min @ 880°C	57.8 at% Na

Synthesis of NaSi inside the Autoclave

It was determined that melting NaSi was not feasible inside the autoclave. As such, NaSi was synthesized from its elements inside the autoclave (A11) with the goal of producing cylindrical NaSi rods for use in conductivity measurements. It can be seen in Figure 65

that the reaction of Na and Si within the autoclave was successful, where the excess molten sodium dissolved the silicon to form a liquid mixture. However, the solidified NaSi strongly adhered to the alumina walls (Figure 65). Attempting to remove or machine the NaSi from the alumina damaged it. The NaSi prepared was too brittle to be useful.



Figure 65: Autoclave sample A11. Elemental silicon and sodium were reacted to produce cylindrical NaSi slabs.

High Temperature XRD Analysis

The high temperature XRD experiment was performed with two goals in mind. The first was to confirm the melting point of NaSi, as it is only experimentally quantified by DTA/DSC methods. Second, insights into the structure of HT-NaSi could be gleaned from this experiment. The filled quartz capillary was tested from 200°C to 770°C using a Bruker D8 Davinci diffractometer. A total of 20 readings were taken. A poly(aryl-ether-ketone) [PEEK] dome was used to contain the atmosphere and provide better temperature equilibrium. However, this polymer dome interfered with the scan, adding strong PEEK peaks which overlapped and masked the NaSi signals (Figure 66). The blue profile, and the corresponding blue spectral lines, was from the PEEK dome. Some of the unexpected

peaks ($2\theta = 19.5^\circ, 21.5^\circ$) were present at room temperature, but would disappear with heating. The PEEK dome, with the unexpected peaks, prevented efficient analysis of the sample, especially at low angles, since the polymer profile must be removed from our data.

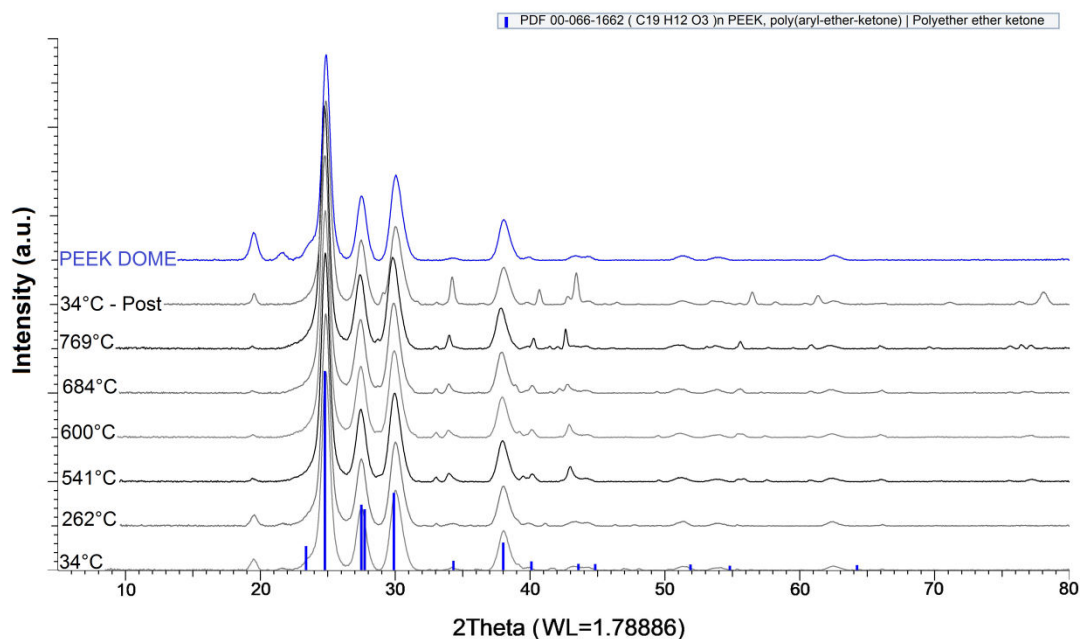


Figure 66: High Temperature Analysis of NaSi in Capillary. The PEEK protective dome significantly interferes with the sample signal. The peak at $2\theta = 19.5^\circ$ is an artifact of the dome, but not from the polymer itself.

The polymer dome profile could be removed at high angles (greater than 33°), with minor artefacts ($2\theta = 38^\circ$). Figure 67 shows the high angle peaks for selected temperature profiles. From the figure, the primary conclusion that can be made was that NaSi started to breakdown before reaching a temperature of 540°C . The breakdown of NaSi was facilitated by the low atmosphere within the capillary, as any sodium vapour could be absorbed by the quartz tube. The absorption of sodium into the capillary tube might have

caused it to rupture. Silicon and a number of unknown phases remained at high temperature. These were likely oxides of sodium and silicon.

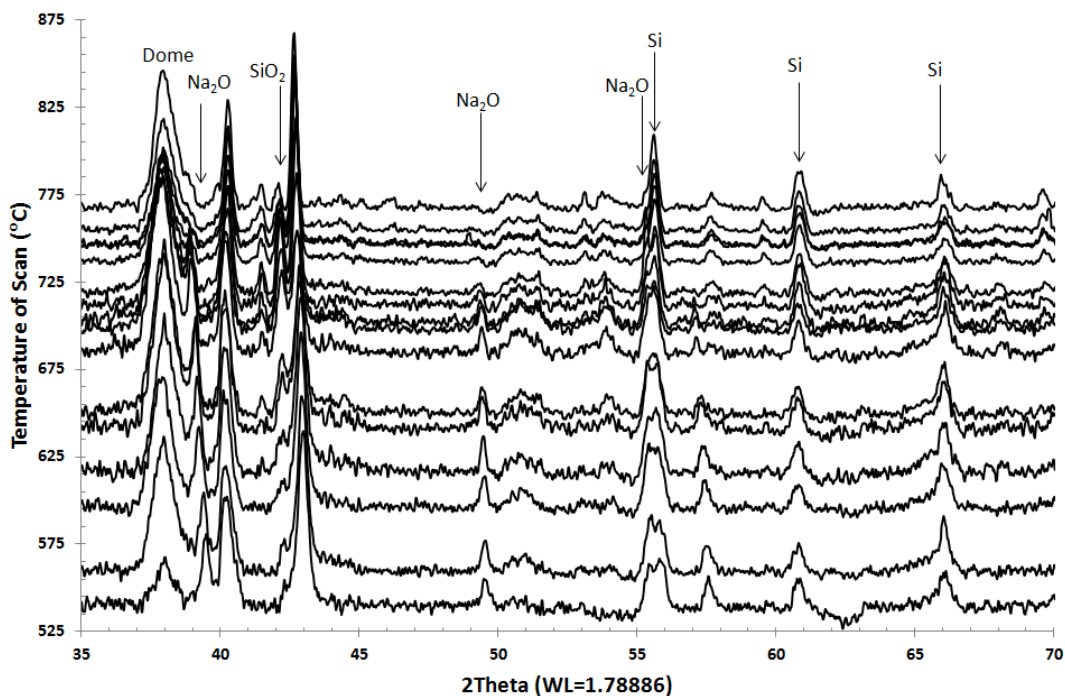


Figure 67: High Temperature of NaSi capillary, with most PEEK dome artifacts removed. Intensity of scan normalized for $I_{\text{Max}}/I_0 = 100^\circ\text{C} + \text{Temperature}$.

DTA & DSC Experiments

Thermogravimetric analysis and differential scanning calorimetry were both attempted in an effort to better understand the NaSi phase. DTA was performed first to provide a qualitative understanding of the system. The experiments were attempted using two different types of gas-tight cells: flame-sealed quartz, and stainless steel (300-series) vessel with a screw-top seal. Unfortunately, both types suffered from reaction with products of NaSi decomposition.

The quartz tube method was unsuccessful for the same reasons as the high temperature XRD. Due to the vacuum required to seal the chamber, NaSi decomposition and sodium evaporation were exaggerated at moderate temperatures. Evaporated sodium was absorbed by the quartz, devitrifying and cracking the cell before any results could be recorded.

The stainless steel crucibles were more robust, as they could be tested multiple times. However the iron and chromium reacted with silicon. One of the cells tested was successfully opened after four DTA cycles. The extracted powder was tested by XRD, and produced the pattern seen in Figure 68. The identified peaks correspond to FeSi, CrSi₂ and Fe₃Si, while the remaining peaks were from free sodium and sodium silicon clathrates. It should also be noted that the transition metal silicides do not possess phase transformations below 850°C, and therefore were not expected to affect the DTA scans. The formation of the silicides, likely exothermic, could explain some of the unusual behaviour in the DTA heatflow signal. Two of the three transition metal silicides found here were also detected in the conductivity measurements.

Another downside of the steel cells was the high relative weight of the container compared to the sample. The average cell weighed nearly 3 g, but could only be loaded with 150 mg of active material. This meant that the signals from the samples, especially broad low amplitude peaks, would be lost to the background. Additionally, due to the thermal mass of the cell, a response lag was detected. The signal shift caused by the lag was estimated using a silver standard, and was corrected as if all cells were identical.

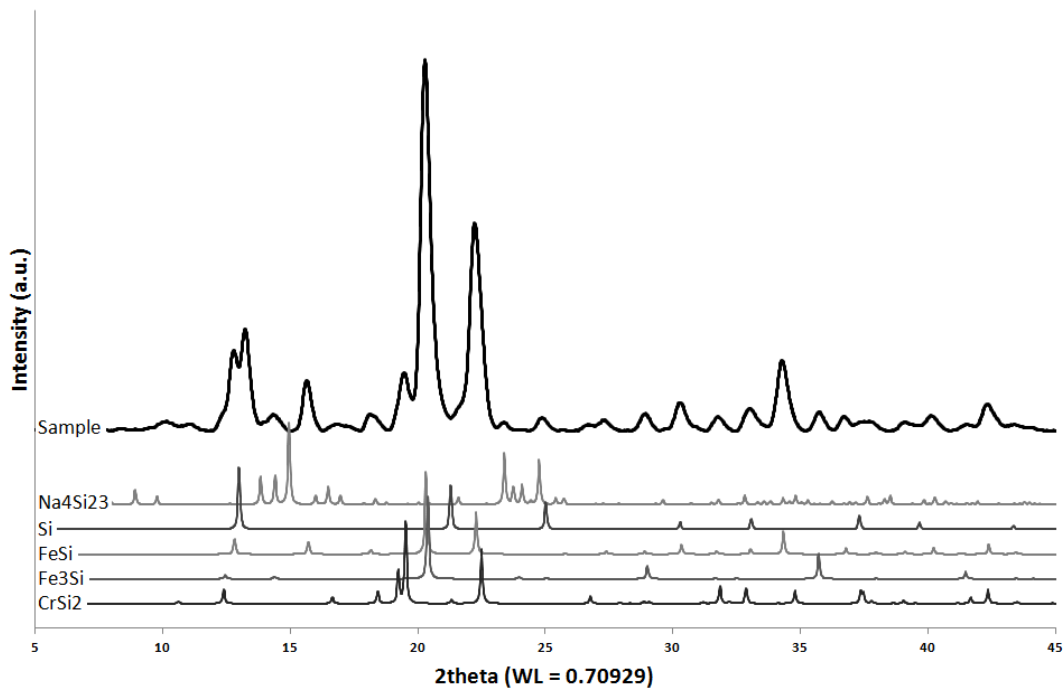


Figure 68: Secondary reactions with NaSi within DTA cells. Silicon from the NaSi reacted with cells.

The first DTA experiment was performed on industrial NaSi powder. The four DTA experiments for this cell are shown in Figure 69. On initial heating, there are two peaks, the first with an onset at 613°C and the second at 765°C. The 613°C peak was due to the allotropic phase change of NaSi, as reported by Morito. This peak was found in all samples tested by DTA and DSC, unless the NaSi had decomposed. The peak at 765°C was attributed to another phase change. Morito explained this as the melting of NaSi at 798°C. Alternatively, this peak could be related to the incongruent decomposition of NaSi to sodium and sodium silicon clathrates or silicon.

On the second heating of the material, the endothermic peak of sodium melting was seen. The presence of sodium in the sample indicates that NaSi had decomposed to its elemental components, or to sodium and a Si-clathrate phase. Additionally, the peak at 765°C had disappeared, and a new endothermic peak was detected at 689°C. Since any free silicon would have reacted with the steel crucible, it can be assumed that the composition of the sample shifted to a sodium content greater than 50 mol%. This new peak would then belong to a sodium rich composition, and not to the synthesized material. The cell was accidentally heated to 1000°C during the second heating. This would have accelerated the decomposition of NaSi and the reaction of silicon with the crucible. Incidentally, all peaks associated with NaSi disappeared from the third and fourth heating, leaving only the melting of sodium to be detected.

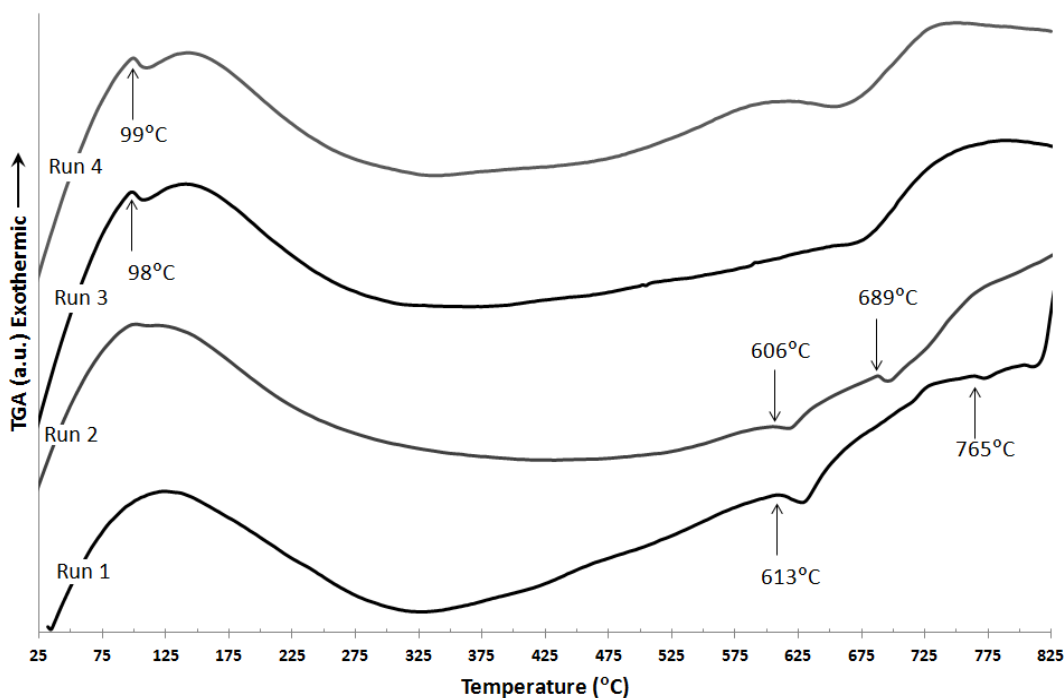


Figure 69: DTA of NaSi powder (SiGNa material).

The second DTA cell consisted of 51% sodium and 49% silicon (molar basis), assembled from elemental reactants. This cell was used to determine the onset and end point temperatures of the NaSi formation reaction. A slight excess of sodium was added to the cell for two reasons. The first was to overcome the error of the scale used to measure the loaded mass. Second, there are no compounds found in the sodium rich region (>50 mol%) of the phase diagram. Therefore, all the peaks found in these DTA tests belong to NaSi or liquid solution. In the first DTA run, the melting of sodium can clearly be seen. This was followed by a complex two-part exothermic peak that started at 446°C and ended at 536°C. This was the clearest exothermic peak, and was believed to be the onset temperature of NaSi formation. The complexity of the peak would indicate that the formation of NaSi was rate limited, taking an extended period of time to complete. The allotropic transformation peak was then detected at 605°C, and followed by another peak at 739°C. These last two peaks were the only peaks detected on subsequent runs. The 605°C peak was likely the LT-HT NaSi phase transformation peak, with a slight shift due to mass, while the peak at 739°C could not be identified.

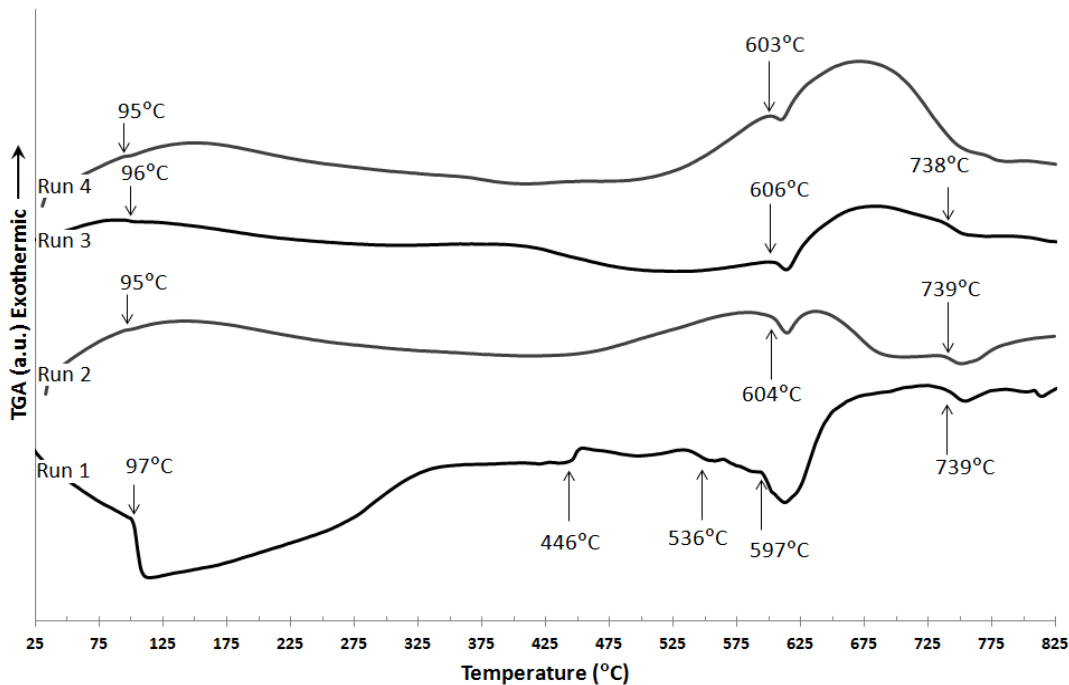


Figure 70: DTA of NaSi using a cell loaded from elemental Na (51 mol%) and Si (49 mol%).

The third DTA cell contained a low sodium concentration (14 mol%). Its purpose was to test for the stability of NaSi compared to sodium silicon clathrates. Two peaks were consistently observed throughout the four DTA runs. These peaks occurred at 615°C and 738°C. The cell was successfully opened and the resultant powder was crushed and analyzed by XRD. The analysis showed that the cell was primarily sodium metal, with some NaSi and sodium silicon clathrates, excluding the transition metal silicides discussed before. This could indicate that the minute amount of NaSi melted or decomposed at 738°C. It is unlikely that this endothermic reaction was caused by the clathrates. No clathrates were expected to be present in the sodium rich DTA cell, yet it also showed this endothermic peak. The reason why the sodium endothermic peaks were

not seen in the DTA analysis was likely due to the miniscule amount of sodium in the cell.

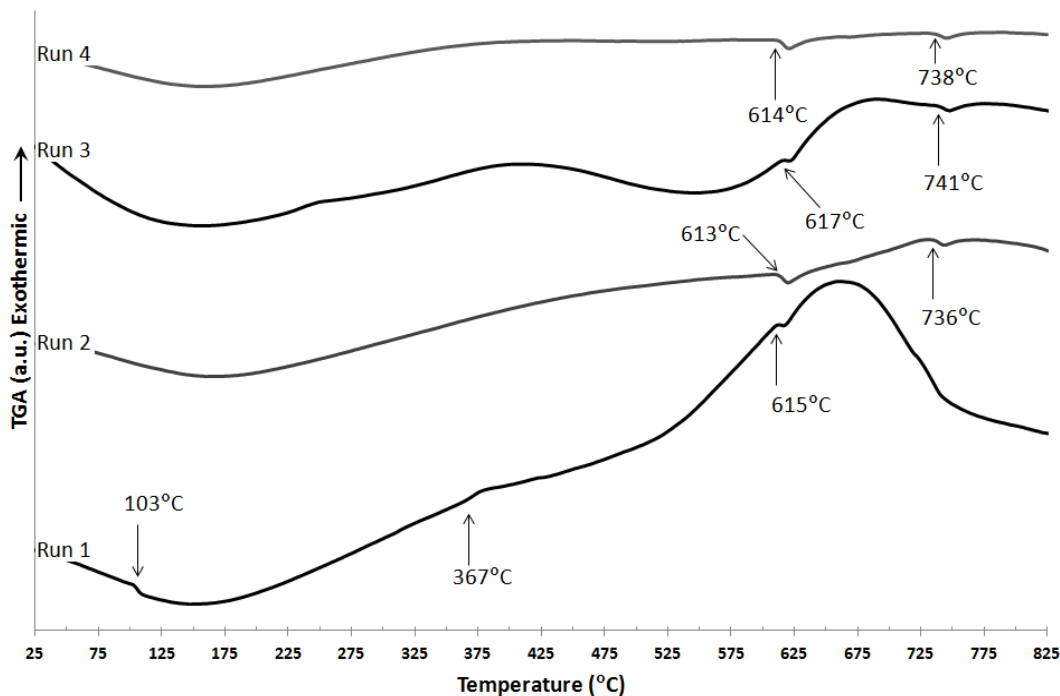


Figure 71: DTA from pure elements Na (14% mole basis).

Unfortunately, due to the low sensitivity of the experiments, potentially useful data could have been lost. The bulky cells had large, broad peaks in signal not consistent with any chemical processes. These were likely due to physical processes, like strain relief in the crucible itself, and may have masked small amplitude peaks characteristic to NaSi and its decomposition products.

Approximation of Heat of Reaction for NaSi from DTA signals

Due the reactive nature of NaSi, and the need to prevent its release, the custom cells used to do DTA prevented the more useful, differential scanning calorimetry [DSC] analysis,

from being implemented. An approximate heat of reaction was calculated using the area below the reaction exotherm, which was compared to that of the silver standard. Using the assumption that the custom cells were nearly identical, the heat of reaction was approximated to -5 kJ mol^{-1} , at 450°C . This value was unusually low for a silicide, but matches first principle calculations by Hao 2012.

Additionally, from the XRD analysis of DTA and conductivity samples, the silicides of iron and chromium were found to have formed at the expense of NaSi. This would indicate that these silicides are more stable at elevated temperatures. Therefore, the Gibbs free energy of NaSi was less negative than that of FeSi and CrSi₂. Assuming that their entropy of formations were similar, this would indicate a considerably lower heat of formation for NaSi than FeSi ($-78.66 \text{ kJ mol}^{-1}$), Fe₃Si ($-93.72 \text{ kJ mol}^{-1}$) and CrSi₂ ($-80.08 \text{ kJ mol}^{-1}$) [89].

This estimation was useful in narrowing the range of heats of formation from the varying values reported in literature. However, the assumption that different cells were identical was flawed, as can be seen by the signal issues. Combining this with the potential for side reactions, higher accuracy was required for modelling.

DSC Experiments

High accuracy cells were designed and produced at McMaster to safely measure the heat of formation of NaSi. These cells had a mass of $860 \pm 20 \text{ mg}$, and were rated to maintain a gas-tight seal to at least 650°C . However, these cells were for a single use. Due to the limitations of the device, the reference for the DSC was not optimum, which required

additional calibration. Figure 72 shows the DSC heatflow profiles of the NaSi, and its two calibration curves. It should be noted that the curves for both calibrations and NaSi show good reproducibility. The first calibration was a silver slug, which was used to determine the shape of the heatflow curve when there are no transitions in the system. The second was a sample of zinc, which was used to determine the equipment specific coefficient. This coefficient represented the difference between the measured ΔH of zinc and literature values. The measured enthalpy of melting zinc was 109.87 J g^{-1} , compared to the literature value of 112.06 J g^{-1} . The coefficient was therefore 1.02. Additionally, the onset temperature for the melting of zinc was measured at 418°C , compared to the literature value of 420°C .

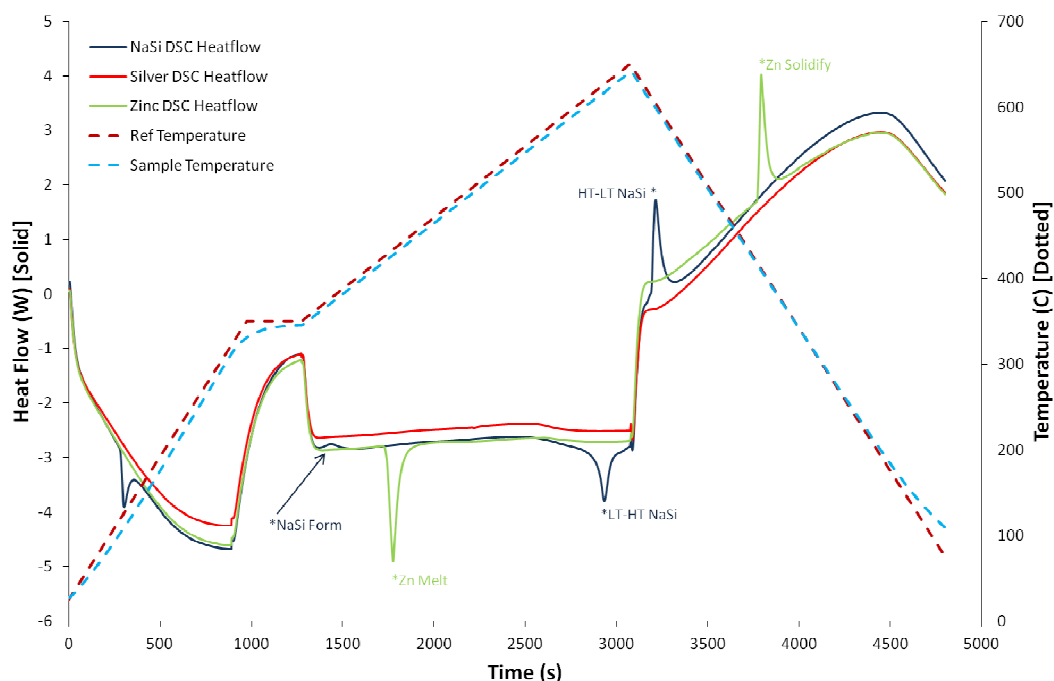


Figure 72: DSC Analysis of NaSi (Blue), Silver (Red), Zinc (Green). The dotted lines show the temperature difference between the sample and reference crucibles.

The NaSi cell was loaded with a combined mass of 37 mg of elemental silicon and sodium at an approximate molar ratio of 55:45, which was done inside an argon-filled glovebox. The error on the sodium and silicon mass measurements was 0.5 mg out of 15 mg and 22 mg, respectively. The section of interest (Figure 73), between 350°C and 650°C, included the only exothermic peak (NaSi formation) and the endothermic LT-HT NaSi allotropic formation. The onset temperature for the allotropic transformation was not very clear, but occurred between 605°C and 613°C, as expected. The enthalpy of transformation was measured at 4.55 kJ mol⁻¹. Unlike the DTA experiment, the formation of NaSi in the DSC was initiated at the much lower temperature of 360°C. The enthalpy of formation for NaSi was measured at 0.27 kJ mol⁻¹. This value was surprisingly low, as many recorded silicides report formations two orders of magnitude larger. First principle calculations of LiSi and NaSi estimated their respective heats of formations at 19.2 and 5.0 kJ mol⁻¹.

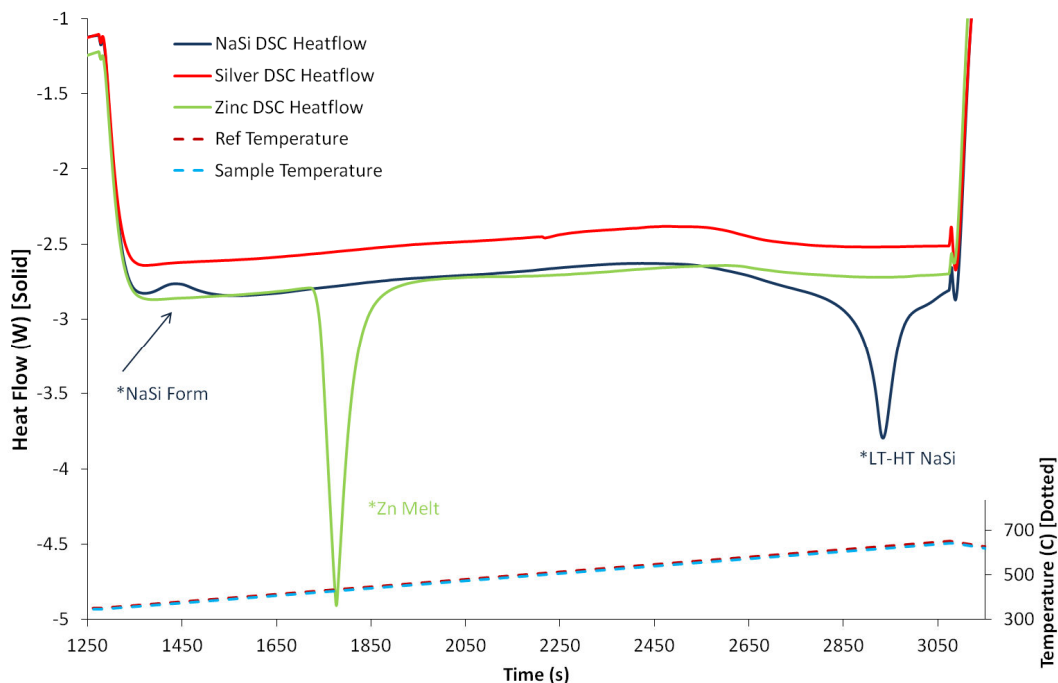


Figure 73: Area of interest for the DSC analysis of NaSi (blue). Notice the high reproducibility of DSC signal.

This discrepancy in enthalpies is hard to rationalize, as there was little room for significant signal losses to the instrument background, based on the instrument coefficient of 1.02 in the temperature range of interest. A reasonable explanation was the reaction of sodium and silicon to form NaSi was slow, and that not all the material had reacted. Therefore, to confirm this hypothesis, the data of an earlier DSC qualifying test was revisited (Figure 74). This test was done at a consistent heating and cooling rate of $10^{\circ}\text{C min}^{-1}$ to 600°C , which more closely resembled the heating profile used in the DTA experiments. Again, the onset temperature was approximately 350°C , much lower than expected, but similar to that of the other DSC run. The measured enthalpy of formation for this run was 0.38 kJ mol^{-1} . An important note was the sodium melting peak before and after the test. By measuring the peak areas, the extent of reaction can be estimated. The

area of the peak for the sodium remainder was 23% of the original sodium melt peak. Assuming that this was consistent between tests, the enthalpy of formation was corrected to $\sim 0.5 \text{ kJ mol}^{-1}$.

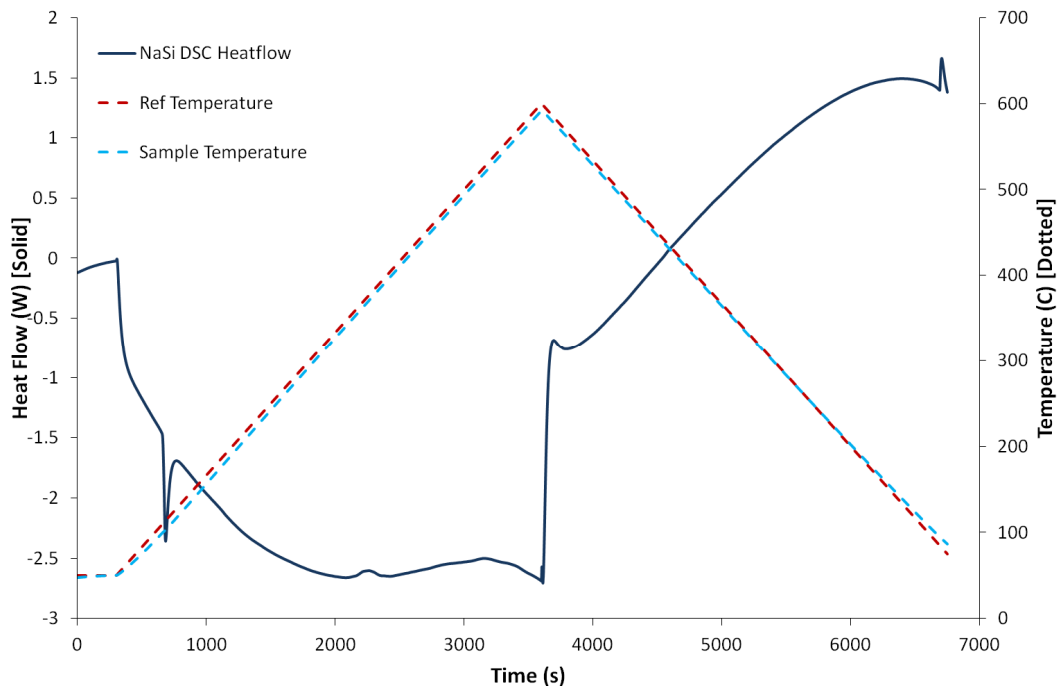


Figure 74: Continuous ramp DSC of NaSi from elements

The alternative hypothesis was that a portion of the enthalpy of formation of NaSi was lost during the LT-HT allotropic transformation. If it was assumed that by 600°C , 77% of the Na mass had been consumed, the remainder would react during the period between 600°C and 650°C . The amount of energy masked by the transformation could be determined by comparing the enthalpies during the heating and cooling stages. During the heating step, the LT-HT transformation enthalpy was measured to be 4.55 kJ mol^{-1} . However, during the cooling portion the coefficient was no longer 1.02, but rather 1.19, based on the zinc calibration. The HT-LT transformation during the cooling step was

measured to be 5.82 kJ mol^{-1} . If this assumption was correct, the difference of 1.27 kJ mol^{-1} plus the initial lower temperature peak of $\sim 0.5 \text{ kJ mol}^{-1}$, would indicate an enthalpy of formation of approximately 1.8 kJ mol^{-1} . This value, which was more reasonable than the initial measurement, was still a factor of 2 or 3 times less than the first principle calculations.

EMF Experiments

The vapour pressure of sodium over NaSi was found to be significant enough to cause a property change of the Corning 1720 glass. However, as the ceramic options outlined in Chapter 4 did not fully seal the cells, the Corning glass was the only valid option for high temperature EMF experiments. NaSi powder from SiGNa was tested from 500°C to 620°C , as shown in Figure 75. It can be seen that the activity values become erratic above 600°C . The activity values were calculated from the cell voltage measured using Equation 6.3. The average cell voltages are presented in Figure 76.

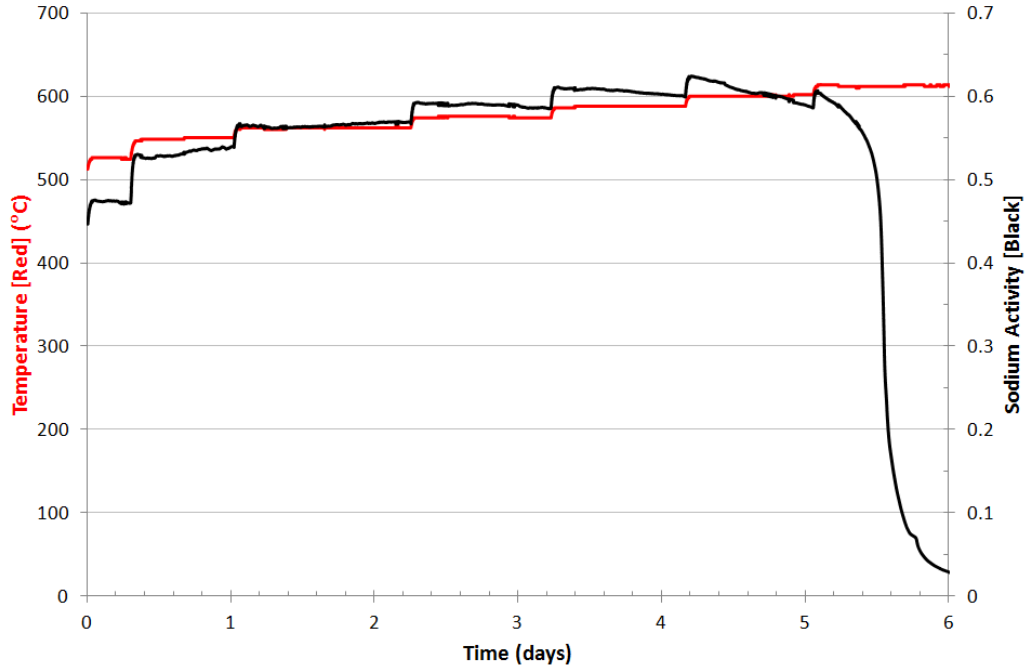


Figure 75: Sodium activity in NaSi (SiGNa).

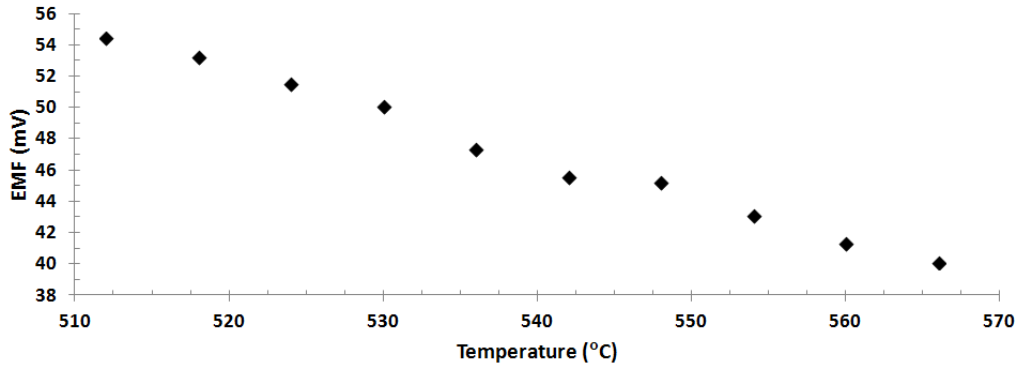


Figure 76: Average EMF values for NaSi, as a function of temperature below 570°C.

$$a_{\text{Na}} = e^{\left(\frac{-E_{\text{cell}}F}{RT}\right)} \quad \text{Eq. 6.3}$$

Here, a_{Na} is the activity of sodium in the phase, while E_{cell} is the EMF recorded (V), F is Faraday's constant, and R the standard gas constant.

Unfortunately, due to the failure of the seal, retrieval of the NaSi powder for XRD was impossible. However, the activity of sodium at the end of the experiment was still at least an order of magnitude higher than the values reported by Mali et al. They also reported cracking and seal failure in their experiments, and as such, additional testing would be beneficial.

Concluding Phase Diagram

The result of the study can be compiled into a phase diagram. From the autoclave measurements, it was seen that NaSi did not melt, but rather decomposed to a mixture of NaSi, Si, and Na₄Si₂₃. Sodium vapour had condensed on the autoclave walls during cooling. Although a three-phase equilibrium is unlikely, it can be deduced that NaSi melts incongruently. The DTA data support the transition of LT-NaSi to HT-NaSi at 612°C.

The DTA and DSC data showed that the heat of formation of NaSi is likely near 1.5 kJ mol⁻¹, but potentially as high as 5 kJ mol⁻¹. Furthermore, the transition enthalpy from LT-NaSi to HT-NaSi was measured to be between 4.5 and 5.8 kJ mol⁻¹. The EMF experiment provides evidence that the activity of liquid sodium in the NaSi-Na₄Si₂₃ region to be as high as 0.6.

Using FactSage, a phase diagram was modelled with the information mentioned above. The lack of evidence for the formation of Type II clathrates allowed them to be ignored for this diagram. This leaves the two phases, NaSi and Na₄Si₂₃. The enthalpy data was used as measured, and the heat capacity values were derived from a linear combination from the elements. The entropy of both phases and the enthalpy of formation of Na₄Si₂₃

were adjusted such that the calculated activity of sodium was within a factor of 2 to those measured. The Na-Si liquid was modelled so as to provide incongruent melting of NaSi. From the autoclave experiments, it could be seen that significant solid phase remained above 800°C. The Gibbs energy of the liquid is presented in Equation 6.4. The final phase diagram is presented in Figure 77.

$$G_{\text{ex}} = 10,000X_{\text{Na}}^1X_{\text{Si}}^1 - 21,000X_{\text{Na}}^2X_{\text{Si}}^1 - 19,500X_{\text{Na}}^3X_{\text{Si}}^1 + 44,000X_{\text{Na}}^5X_{\text{Si}}^1 - 25,000X_{\text{Na}}^1X_{\text{Si}}^5 - 65,000X_{\text{Na}}^5X_{\text{Si}}^2 - 2,200,000X_{\text{Na}}^5X_{\text{Si}}^6 - 3,600,000X_{\text{Na}}^4X_{\text{Si}}^9 \quad \text{Eq. 6.4}$$

Table 14: Thermodynamic Properties of Na-Si phases.

	ΔH_{298} [J mol ⁻¹]	ΔS_{298} [J mol ⁻¹ k ⁻¹]	ΔH_{Trans} [J mol ⁻¹]	T_{Trans} [K]
LT-NaSi	-18,500	62.3	—	—
HT-NaSi	—	—	4,500	885.15
Na ₄ Si ₂₃	-95,000	700	—	—

Na - Si

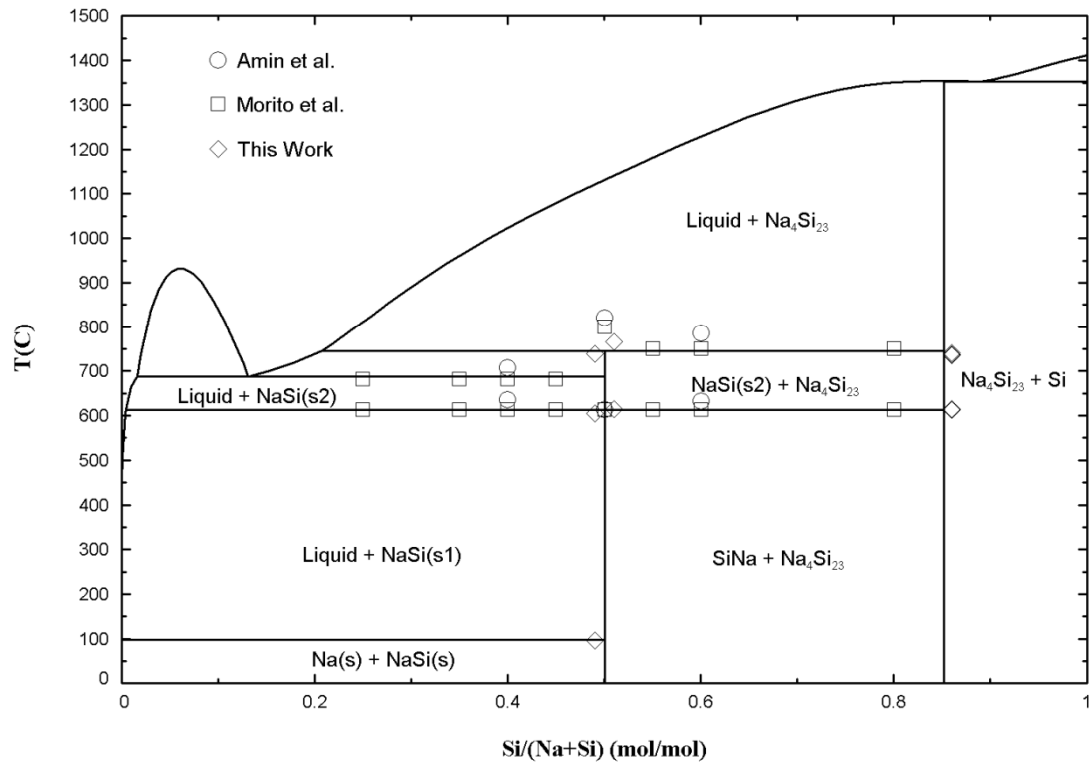


Figure 77: Revised Na-Si phase diagram using new DTA/DSC and EMF data. Symbols represent phase transition onset temperatures of various DTA and DSC experiments.

Chapter 7: Bismuth Manganese Oxide Supercapacitors

Bismuth manganese oxide is normally synthesized using high temperature or lengthy hydrothermal processes. The sol-gel method was applied, and optimized, to produce fine BiMn_2O_5 powders. The powders resulting from a consistent method were tested for pseudocapacitance using bulk and thin film electrodes.

Synthesis of BiMn_2O_5

The sol-gel production method was used to produce small 2 g batches of fine BiMn_2O_5 powders [**BMO**]. The sol-gel process could be scaled up to larger batch sizes. A slight excess of manganese nitrate was added to the synthesis to assure complete reaction to BiMn_2O_5 . A shortage of manganese nitrate could cause other phases, like Bi_2O_3 or $\text{MnBi}_{12}\text{O}_{20}$, to form. Three process parameters needed to be considered, and optimized, to form the BMO powders. These parameters were sol-gel preparation ordering, sol composition, and heat treatment.

In the process for making BASE by sol-gel, the metal nitrates and citric acid could be mixed together and water added to fully dissolve the material prior to drying. However, it was found that adding water directly to the mixture would cause dissolution issues. No appreciable dissolution of the bismuth nitrate was likely the culprit, since it could form insoluble bismuth oxynitrate in an insufficiently acidic aqueous solution [90]. As such, a step process was required. The first attempt, which also corresponded to SC-A in Table 15, first dissolved the citric acid in water. The bismuth and manganese nitrates were then added to the citric acid solution. Dissolution of the bismuth nitrate was still not observed.

Bismuth nitrate can be dissolved rapidly in dilute nitric acid. The last and most successful, process diluted concentrated nitric acid in water, prior to dissolving each metal nitrate separately. The solution was completed by dissolving the citric acid at the end of the process.

The sol-gel composition needed to be optimized to produce the best possible product. Table 15 shows a variety of sol-gel compositions tested. With the knowledge that nitric acid was a requirement for xerogel stability, various metal nitrate to nitric and citric acid ratios were tested. It was known that citric acid should be present at an equimolar concentration to the metal nitrates, which corresponded to 0.7 g citric acid per gram of metal nitrates. However, the amount of nitric acid needed to be optimized. SC-B, SC-D and SC-F tested three different nitric acid concentrations. A critical mass of nitric acid existed above which the xerogel was stable. Below this mass, the sol-gel would start precipitating early, while significant amounts of liquid remained. SC-C tested the feasibility of using excess citric acid as a replacement for nitric acid. The end result was an aggressive over boiling at evaporation (90°C) temperatures. All subsequent BMO powders were prepared using SC-D. The resultant xerogel powders were converted to amorphous oxides at around 200°C on a hotplate in a fume hood, and then calcined to produce the final powders.

Table 15: BiMn₂O₅ Xerogel Synthesis Method

Sol-gel Composition	Bi(NO ₃) ₃ ·5H ₂ O to Mn(NO ₃) ₂ ·4H ₂ O Ratio by Mass	Metal Nitrates to HNO ₃ Ratio by Mass	Metal Nitrates to Citric Acid Ratio by Mass	Xerogel Result
SC-A	1 : 1.1	0	1 : 0.7	Fail – No Dissolution
SC-B	1 : 1.1	1 : 0.6	1 : 0.7	Fail – Early Precipitate
SC-C	1 : 1.1	1 : 0.6	1 : 1.4	Fail – Over boil
SC-D	1 : 1.1	1 : 1.2	1 : 0.7	Success
SC-E	1 : 1.1	1 : 1.2	1 : 1.0	Fail – Over boil
SC-F	1 : 1.1	1 : 2.9	1 : 0.7	Success

The last optimization step was the heat treatment of the xerogel. The converted xerogels produced by SC-D were poured into small α -alumina crucibles, and heated at 5°C min⁻¹ to various temperatures. The powders were not packed into the crucible, to avoid the tendency for reducing particle-particle sintering. Table 16 shows the different heat treatments and the resulting material. The HT-C to HT-E heat treatments reliably produced materials with ideal compositions. Increasing the reaction temperature above 750°C (HT-F & HT-G) did not provide additional benefit, and was likely to suffer from bismuth volatilization that plagues solid state synthesis. The two interesting heat treatments were HT-A and HT-B. Firstly, HT-B had remnants of both Bi₂O₃ and Mn₂O₃, which indicated that a longer calcination might produce the desired product. HT-A, on the other hand, produced a mixture of crystalline and amorphous material of varying composition. Compared to the solid state sintering and hydrothermal methods found in literature, the reaction time of HT-A was short. Increasing the reaction time might produce a better material without excessive particle sintering. The XRD patterns of powders heat-treated using HT-A to HT-E are shown in Figure 78. The XRD pattern for

Bi_2O_3 has several peaks overlapping those produced by Mn_2O_3 and BMO (Figure 111-Appendix). However, the peak found at $2\theta = 28.0$ provided clear indication whether Bi_2O_3 was present.

Table 16: Result of Calcination of BiMn_2O_5 Xerogel

Heat Treatment	Temperature – Hold	Result
HT-A	400°C – 2.0 h	Non-BMO powder
HT-B	600°C – 1.5 h	Lightly sintered BiMn_2O_5 powder with Mn_2O_3 & Bi_2O_3
HT-C	650°C – 1.5 h	Lightly sintered BiMn_2O_5 powder with Mn_2O_3
HT-D	700°C – 1.5 h	Lightly sintered BiMn_2O_5 powder with Mn_2O_3
HT-E	750°C – 1.5 h	Lightly sintered BiMn_2O_5 powder with Mn_2O_3
HT-F	900°C – 30 m	Sintered into hard pellet
HT-G	1100°C – 10 m	Reacted with Crucible (likely melting)

The repeatability of the sol-gel process was tested by processing two powders identically using SC-D and HT-E. BMO-G and BMO-O successfully produced BiMn_2O_5 powders with trace amounts of Mn_2O_3 . Figure 79 shows the near identical XRD profiles with a minor variation in the Mn_2O_3 peaks. This variation in Mn_2O_3 can be explained by a slight deviation in the Bi to Mn ratios during the weighing of metal nitrates.

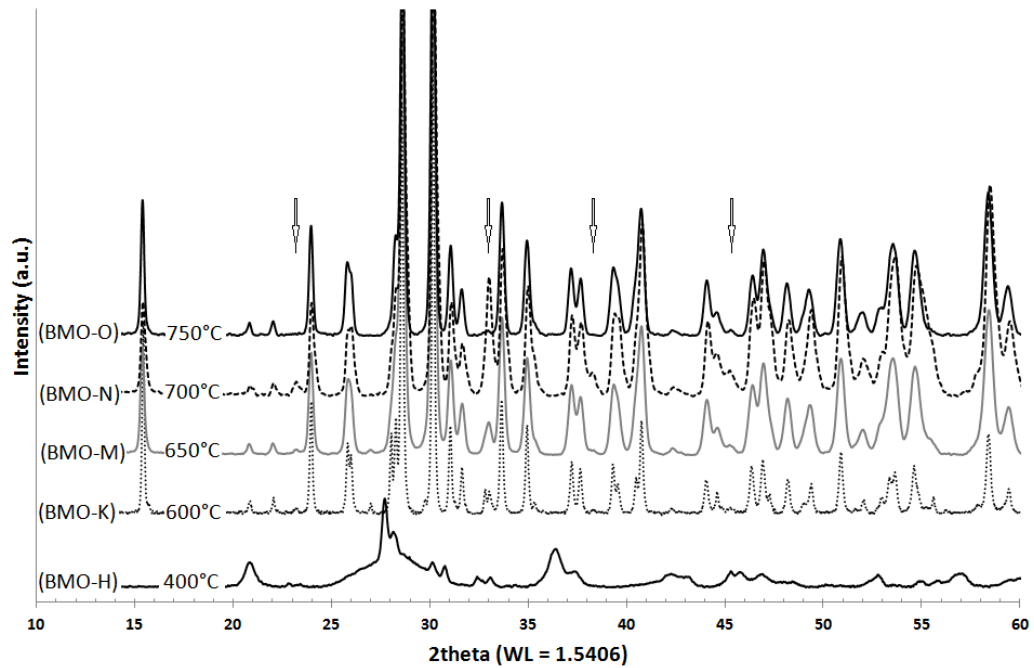


Figure 78: XRD Analysis of BiMn₂O₅ powders calcined at various temperatures. Arrows point to characteristic peaks of Mn₂O₃. All other peaks in sample K through O are from BiMn₂O₅.

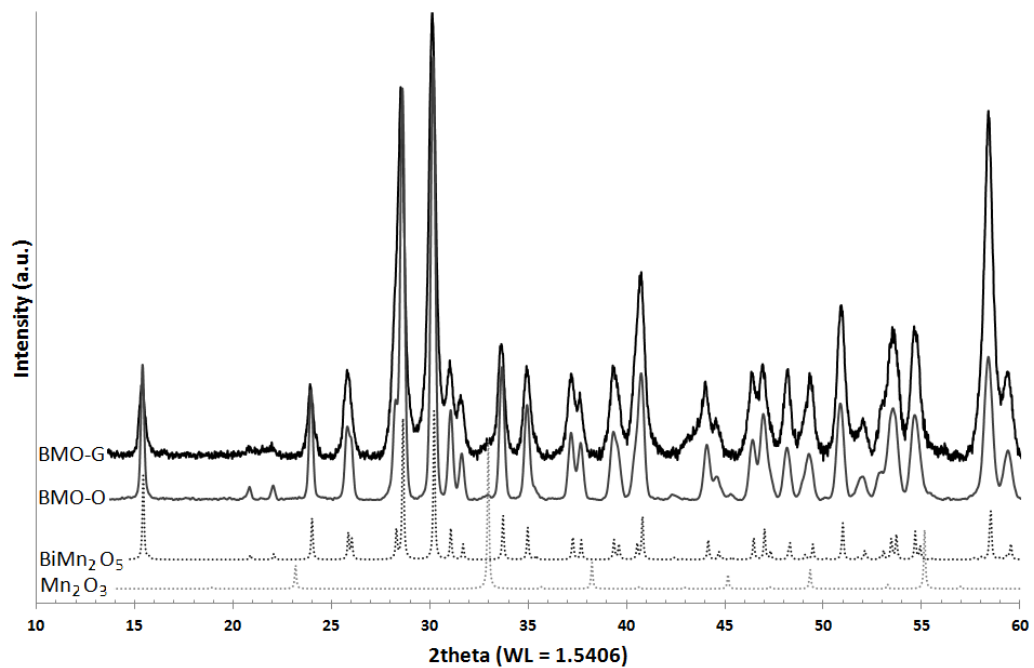


Figure 79: Repeatability of BiMn₂O₅ Sol-gel Synthesis at 750°C

The BMO powders produced were relatively fine, with an average particle diameter of 2.65 microns, with the largest particles approximately 10 microns in diameter. However, these large particles were not ideal for capacitor applications. Additionally, considering the density of BMO, the feasibility of suspending the powders for processing was low. A low energy jar-mill was used to reduce the particle size of the powders. Figure 80 shows the reduction of particles size, using a two step process, from 2.65 microns to 0.25 microns after ~3 weeks of ballmilling using 5 mm zirconia balls. The first step, using only slightly basic water, quickly reduced the particle size to sub-micron size. Figure 81 shows that none of the particles were above 1 micron, by the end of this step. Some of the material was harvested for testing. The remainder of the powder was further ballmilled. To assist the milling, a surfactant was used to suspend and separate BMO particles. After a total of three weeks, the operation was stopped. Extensive ballmilling will introduce zirconia (milling media) and HDPE (jar) impurities, especially due to the light loading (< 2 g) BMO added to the jar.

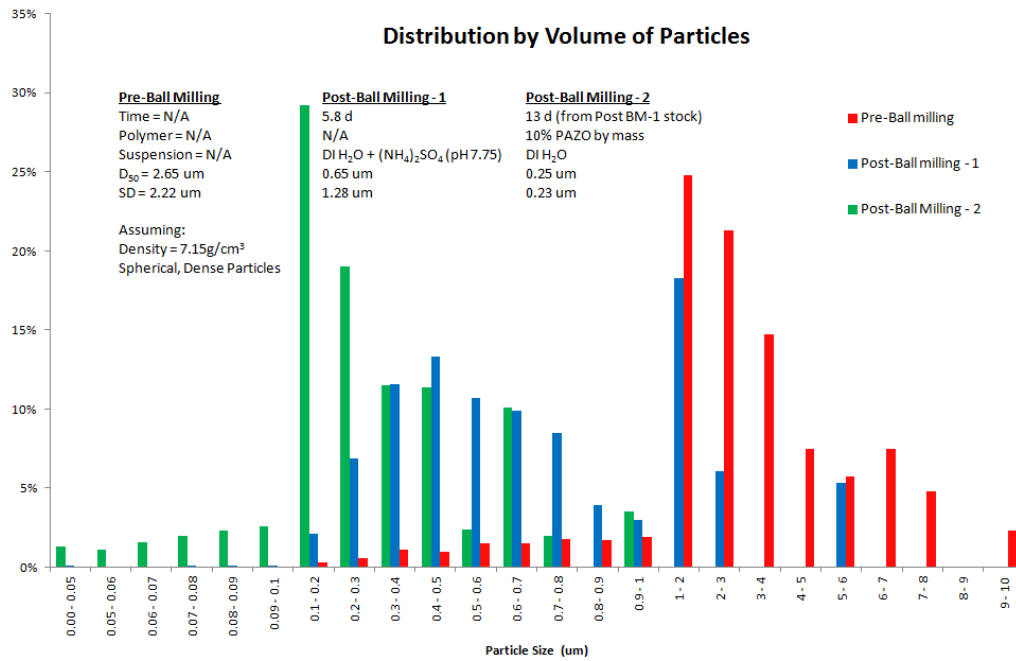


Figure 80: Change in BiMn_2O_5 particle size with ball milling.

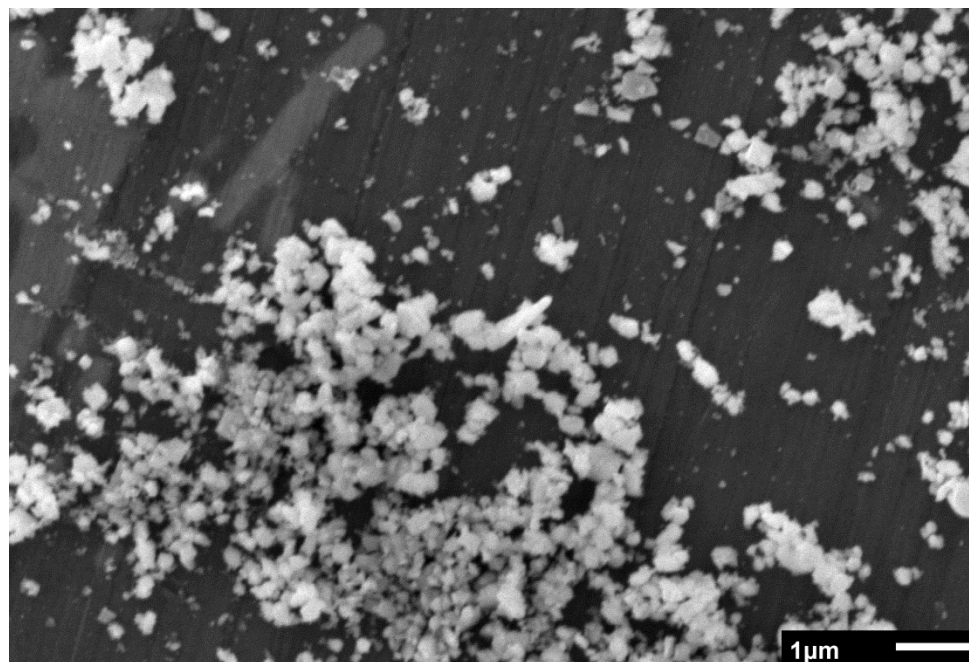


Figure 81: SEM image of BiMn_2O_5 powders after ball milling for 13 days.

Testing of Material for Pseudocapacitance

Bismuth manganese oxide was tested for pseudocapacitance using two types of electrodes. These electrodes had a surface area of 1 cm^2 . The first were bulk electrodes using nickel foams loaded with approximately 58 mg of material. These were used to characterize the effects of ballmilling on the capacitance. The second were thin film electrodes, where 1 to 2 mg of material was electrophoretically deposited on steel substrates. In both cases, the BMO was mixed with CNT in a 4 to 1 mass ratio. Bulk electrodes used an addition of 3% of PVB to bind the active material to the nickel foam, while the thin film electrodes used 10% PAZO.

Bulk Electrode Capacitance

Three bulk electrodes (BMO-G) were tested, one before ballmilling ($D_{50} = 2.65 \text{ }\mu\text{m}$), a second after the first milling step ($D_{50} = 0.65 \text{ }\mu\text{m}$), and the third after milling was completed ($D_{50} = 0.25 \text{ }\mu\text{m}$). Each electrode was activated, by subjecting it to one hundred cyclic voltammetric 20 mV s^{-1} sweeps, prior to testing. The testing comprised of a series of voltammetric sweeps at 2, 5, 10, 20, 50, 100 mV s^{-1} , which were followed by impedance spectroscopy.

The un-milled powder exhibited the lowest capacitance of the three electrodes. Figure 82 shows the capacitive behaviour of the powder in a voltage window of 0 - 0.9 V vs SCE. Near box shape CVs were recorded, with the expected rounding at the higher scan rates. Unfortunately, the current response was weak, providing less than 10 mA cm^{-2} at the 100 mV s^{-1} scan rate. As such, the calculated areal (0.09 F cm^{-2}) and gravimetric (1.4 F g^{-1})

capacitances of the powder were low at 2 mV s^{-1} (Figure 82). This value was eclipsed by BMO synthesized by hydrothermal methods, with a capacitance of 6 F cm^{-2} (75 F g^{-1}) at 2 mV s^{-1} [59]. However, the capacitance retention was found to be 41% at 100 mV s^{-1} .

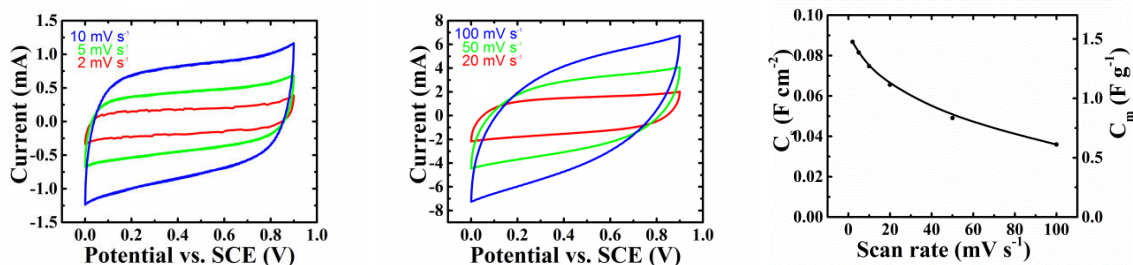


Figure 82: CV of BiMn₂O₅ (Pre Milling) at Left) 2, 5, 10 mV s⁻¹, Center) 20, 50, 100 mV s⁻¹. Gravimetric and areal capacitance (Right).

The first ballmilling significantly increased the capacitance of the BMO powder, while maintaining near box shape of good capacitors (Figure 83). The current response of the material nearly doubled, which increased the capacitance to 0.16 F cm^{-2} (3 F g^{-1}). It should be noted that the electrode was 10% lighter than the unmilled electrode. The milling, however, negatively impacted the capacitance retention at 100 mV s^{-1} . The retention for this electrode was 36%. The impedance response showed a reduction of the Z'' vs Z' slope, from nearly 90° to 70° (Appendix).

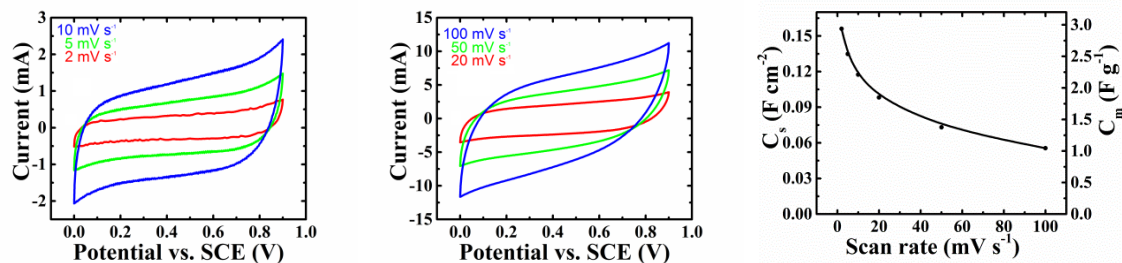


Figure 83: CV of BiMn₂O₅ (Milling to 0.65 μm) at Left) 2, 5, 10 mV s⁻¹, Center) 20, 50, 100 mV s⁻¹. Gravimetric and areal capacitance (Right).

The second ballmilling reduced the particle D_{50} from 0.65 to 0.25 μm . This reduction in particle size corresponded to an approximate tripling of powder surface area ($4.5 \text{ m}^2 \text{ g}^{-1}$ from $1.5 \text{ m}^2 \text{ g}^{-1}$). A significant increase in the cyclic voltammetric response was shown due to the aggressive reduction in particle size. However, the box shape (Figure 84) was severely distorted near the upper edge of the voltage window, especially at higher scan rates. This distortion was likely caused by conditions that limited Mn^{4+} to Mn^{3+} reduction. The capacitance at 2 mV s^{-1} significantly improved to 0.62 F cm^{-2} (10 F g^{-1}). However, this still represented a fraction ($\sim 10\%$) of the capacitance reported by Liu, even though the particle sizes of the powders were similar. Additionally, the capacitance retention of this milled material was significantly hindered, even at low voltage sweeps. The retention at 100 mV s^{-1} was below 20%. It should be noted that some of the improvement was contributed by the mass loading of the electrode, as it was slightly heavier than the first electrode by 7%.

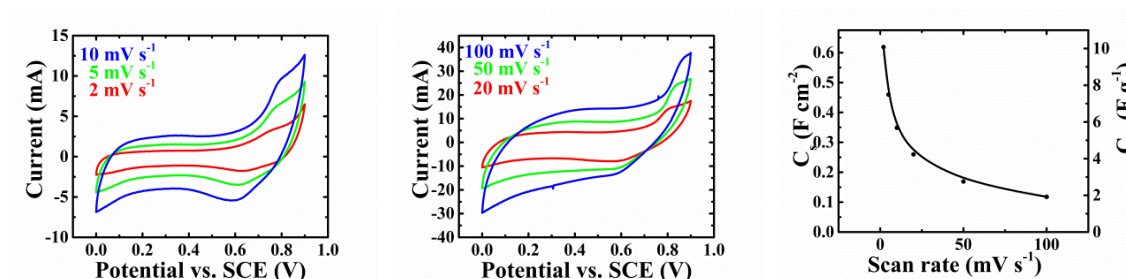


Figure 84: CV of BiMn_2O_5 (Milling to $0.25 \mu\text{m}$) at Left) 2, 5, 10 mV s^{-1} , Center) 20, 50, 100 mV s^{-1} . Gravimetric and areal capacitance (Right).

Thin Film Electrodes Capacitance

The feasibility of thin film capacitors from sol-gel BMO powders was studied. The first point of order was to find a suitable dispersant for BMO. The first tested were CMC and PAZO, in their respective H₂O-ethanol solutions. BMO was added to the dispersants (1 g L⁻¹) at a 2.67 to 1 mass ratio, and electrophoretically deposited onto steel coupons at 10 V (10 min), 30 V (3 min), and 50 V (3 min). Figure 85 shows the coating morphology of each sample. The CMC samples at all voltages deposited sporadic films, and were unsuitable for thin film electrodes. The use of PAZO allowed deposition of thick and visually uniform coatings at 30 V and 50 V. The coupon treated at 10 V still had areas of steel which were still visible. This was explained by the sporadic film seen in Figure 85-B. Both the PAZO-30 V and 50 V coatings were strongly adherent, but, through SEM imaging, it was seen that the 30 V coating was more uniform and with less cracking. Electrodes for capacitance testing were deposited at 30 V for various times, such that they would have a mass loading between 1 and 2 mg cm⁻².

Figure 86 shows the FTIR profiles of CMC (Left) and PAZO (Right) assisted electrophoretically deposited BMO. In CMC, the peaks at 1589 cm⁻¹ and 1412 cm⁻¹ corresponded to –COONa, while the peak that occurred near 1719 cm⁻¹ corresponded to the protonated –COOH group. This peak is most prominent in b) which is the deposited polymer only. It is still seen in BMO-polymer deposit (c).

In the case of PAZO, the peak near 1675 cm⁻¹ corresponded to protonated –COOH groups, while the peaks at 1589 and 1624 cm⁻¹ corresponded to –COONa. Again, the pure

polymer shows the protonated peaks, while the co-deposited BMO/Polymer has this peak suppressed.

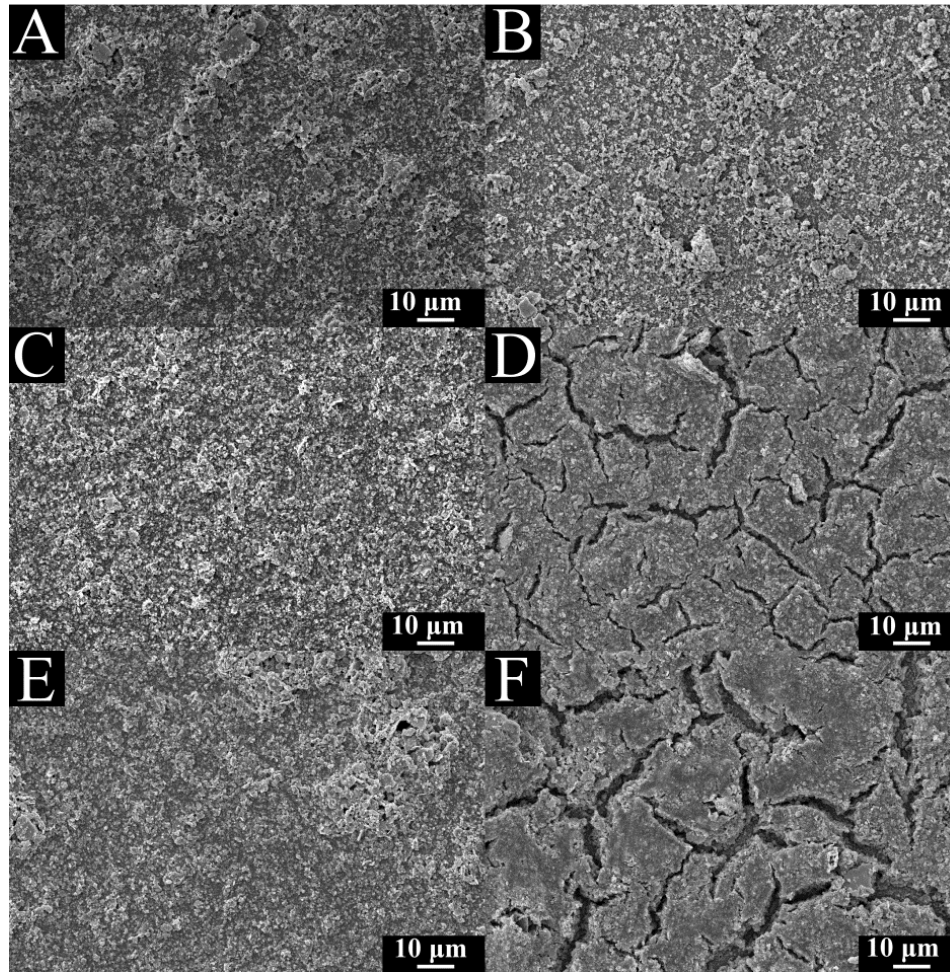


Figure 85: SEM images of coating deposited using CMC Surfactant A) 10 V, C) 30 V, E) 50 V, and PAZO Surfactant B) 10 V, D) 30 V, F) 50 V.

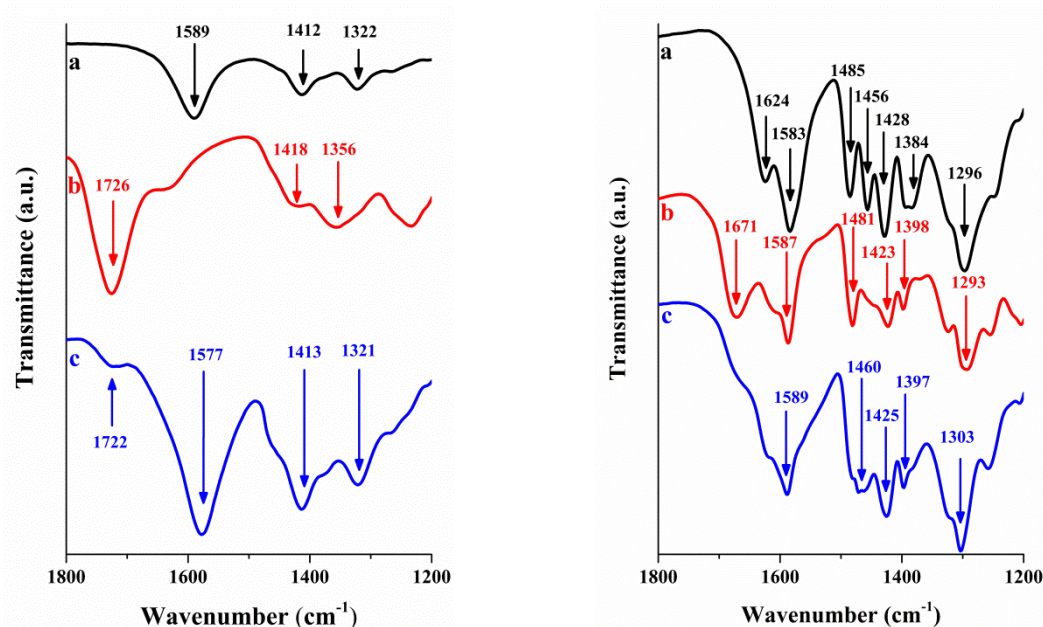


Figure 86: FTIR analysis of BMO deposits using CMC (Left) and PAZO (Right). Comparative profiles of a) Pure polymer, b) Deposited polymer, c) Deposited Polymer + BMO.

An electrode was produced using the ballmilled BMO ($D_{50} = 0.25 \mu\text{m}$) by PAZO assisted EPD at 30 V. The total mass loading was 0.9 mg cm^{-2} , with a BMO:CNT ratio of 4:1. The PAZO content was 10% of the total mass. This electrode was plagued by extremely high resistance. This excessive resistance was likely due to zirconia impurities from ballmilling. These zirconia nanoparticles were present in significant amounts in the sample (Figure 87), and these would efficiently form resistive coatings by EPD alongside the BMO. Therefore, coatings from as-synthesized BMO were tested.

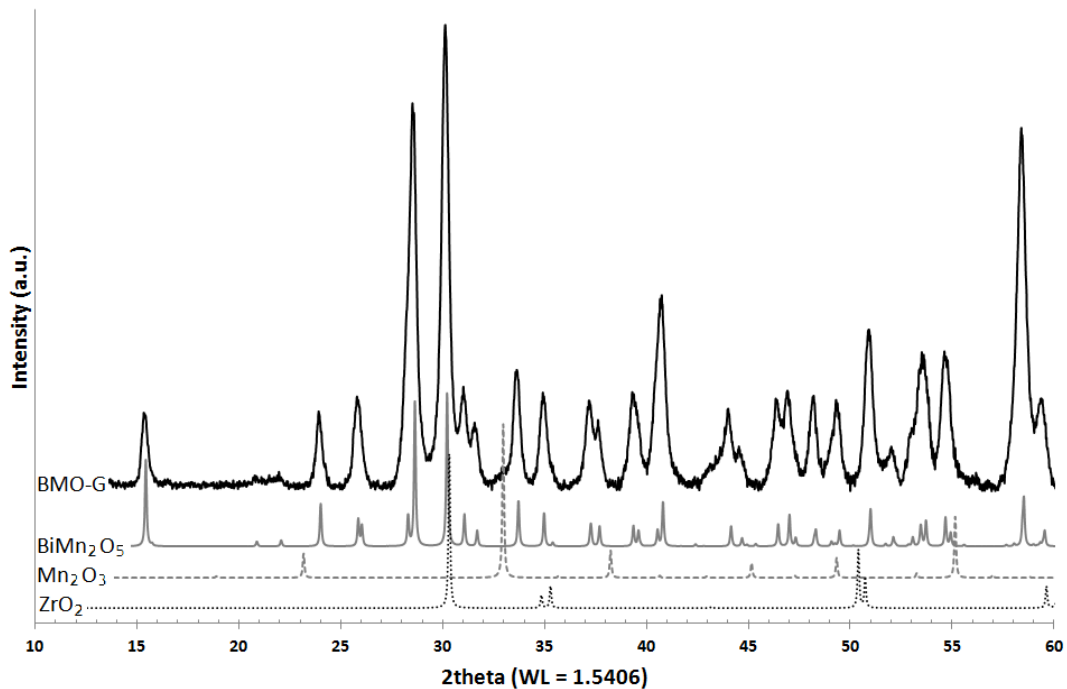


Figure 87: XRD analysis of ball milled BiMn_2O_5 with ZrO_2 impurities.

Bismuth manganese oxide can be difficult to suspend in water-ethanol solutions due to its density of 7.15 g cm^{-3} . The as-synthesized BMO powders have a broad particle size distribution, with significant amounts of particles with diameters greater than 1 or 2 microns. These particles have low surface area, make up a large amount of the sample mass, and segregate from the solution rapidly. A fresh sample ($\sim 2 \text{ g}$) of BMO powders was suspended in anhydrous ethanol by ultrasonication. The coarse particles were allowed to separate from the suspension by settling to the bottom during a short period of time. The fine particles, still suspended, were removed and allowed to dry. Figure 88 shows the significant reduction in particle size and distribution without introducing impurities.

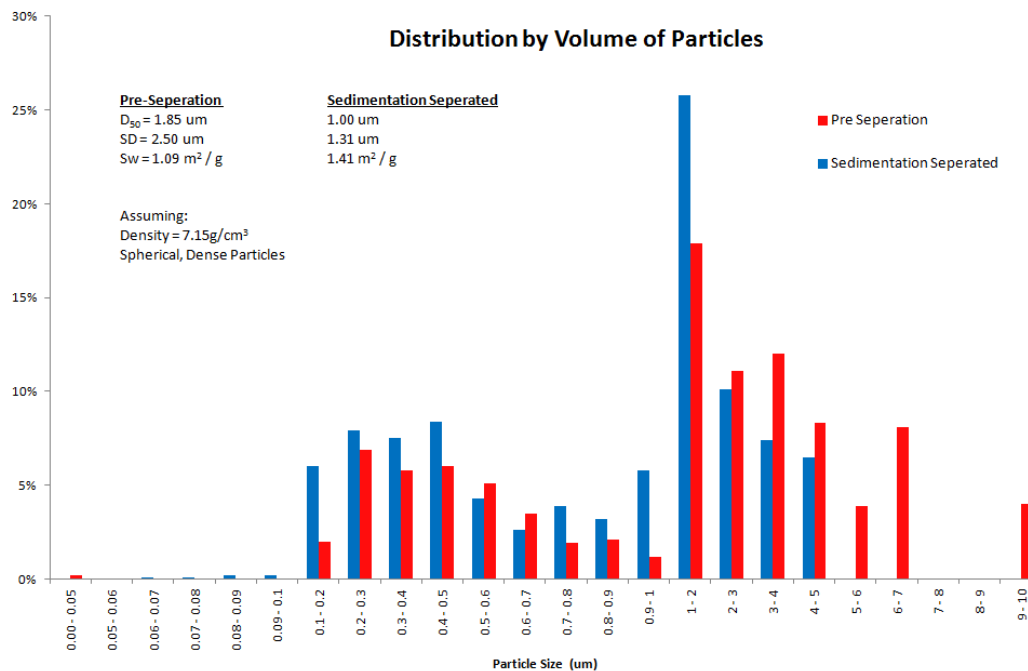


Figure 88: Particle Size reduction of BiMn_2O_5 powders through sedimentation in ethanol.

This pure powder was deposited with the same parameters as before, with a final mass loading of 2 g cm^{-2} . Figure 89 shows the results of the deposited BMO electrode with an area of 3.24 cm^2 . The CVs at all sweep rates maintained their box shape, albeit with very low current response. Thin film electrodes are generally expected to have enhanced capacitance when compared to bulk electrodes. However, the gravimetric and areal capacitances of this thin film capacity were approximately 2.4 F g^{-1} and 6.0 mF cm^{-2} . Although the gravimetric capacitance is about twice that of the un-milled BMO powder, it is still about four times lower than the reduced size BMO powders. The retention of the thin film electrode at 100 mV s^{-1} was 70%, a significant retention over the bulk electrodes.

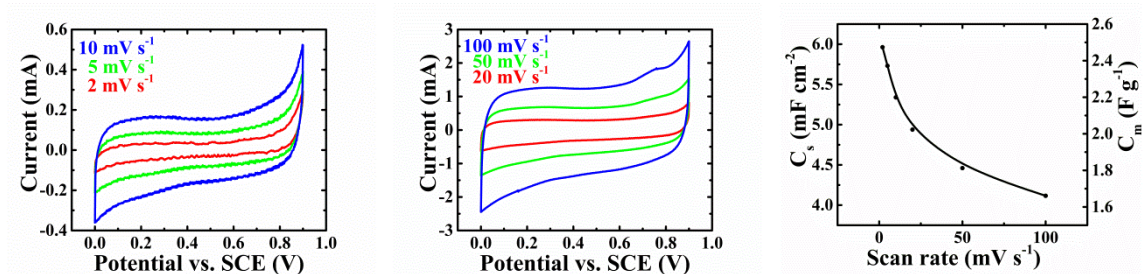


Figure 89: CV of BiMn₂O₅ (Separated 1.00µm) at Left) 2, 5, 10 mV s⁻¹, Center) 20, 50, 100 mV s⁻¹. Gravimetric and areal capacitance (Right).

Comparatively, the performance of this material was poor. When compared to Liu et al., the best gravimetric capacitance of the sol-gel synthesized BMO was about 10% of the capacitance of the hydrothermally synthesized BMO. Additionally, when compared to other transition metal oxide capacitors, this material fared poorly. Other sol-gel synthesized capacitor materials like RuO₂ and Co₃O₄ have reported capacitance of 720 and 740 F g⁻¹ [91]. MnO₂ has been shown to have a capacitance of 140 F g⁻¹ [92], while Bi₂O₃ doped MnO₂ had a capacitance of 136 F g⁻¹ [93].

Conclusion to BiMn₂O₅ Capacitance

This study showed that BiMn₂O₅ could be successfully synthesized using the citrate sol-gel method. Powders of BiMn₂O₅ with engineered Mn₂O₃ excess could be calcined between 600°C and 750°C for short periods of time without BiMn₂O₅ decomposition through Bi₂O₃ evaporation. The BiMn₂O₅-CNT electrodes were shown to have a gravimetric capacitance of 1.4 F g⁻¹. This was improved to 10 F g⁻¹ through particle size reduction, however, significant ZrO₂ impurities due to ball milling negatively affected cells.

Chapter 8: Electrophoretic Deposition of Lithium-ion

Battery Materials

The use of PAZO and CMC assisted EPD was tested for oxide materials commonly used for lithium ion batteries anodes and cathodes. The anode material was $\text{Li}_4\text{Ti}_5\text{O}_{12}$ [LTO], and the cathode materials were LiFePO_4 [LFPO], LiMn_2O_4 [LMO] and $\text{LiMn}_{1.5}\text{Ni}_{0.5}\text{O}_4$ [LMNO]. Large (25 cm^2) battery cathodes were successfully deposited on aluminium substrates. These cathodes were sent for testing at the National Research Council of Canada.

EPD Coating of Li^+ Compounds

Small steel coupons were coated with the various oxide materials from solutions (80 mL) of 1 g L^{-1} PAZO or CMC with 2.67 g L^{-1} oxide additions. These were coated at voltages of 10 V, 30 V, and 50 V, for 10 min, 3 min, and 3 min, respectively. Three factors were monitored during the EPD suitability experiments. First, the stability of the oxides in the EPD solution was tested (Table 17). In this case, the stability was defined as the ability of the powders to remain suspended in solution for extended periods of time with minimal settling. Table 17 shows the particle size and stability of the powders in CMC and PAZO.

Table 17: Stability of EPD Solution for Li^+ anode and cathode materials

	LTO	LFPO	LMO	LMNO
D_{50}	200 nm [D_{90}]	3.5 μm	6 – 7 μm	5 – 7 μm
Density	3.5 g cm^{-3}	4.4 g cm^{-3}	4.29 g cm^{-3}	4.45 g cm^{-3}
Stability (CMC)	Stable	Stable	Slow Settling	Rapid Settling
Stability (PAZO)	Stable	Rapid Settling	Rapid Settling	Rapid Settling

Second, the quality of the deposits was examined to find unusual features, which included cracking, spallation, nodules, and gaps. This was done using SEM surface imaging near the center of the sample. Lastly, the bonding of CMC and PAZO to particles and steel substrates was tested by FTIR.

Lithium titanate exhibited good stability in both PAZO and CMC solutions. This was expected, since it had a relatively low density and particle size, both important in colloidal solutions. The dispersants were more instrumental in the prevention of agglomeration and coating adhesion. The coatings resulting from both polymers were strongly adherent and visually uniform, with the exception of some spallation at the edges of 30 V and 50 V PAZO assisted samples. The SEM images (Figure 90) show that both PAZO and CMC assisted EPD produced dense coatings of LTO at all voltages. However, both sets of coatings suffered from the formation nodules of agglomerated LTO (Figure 91).

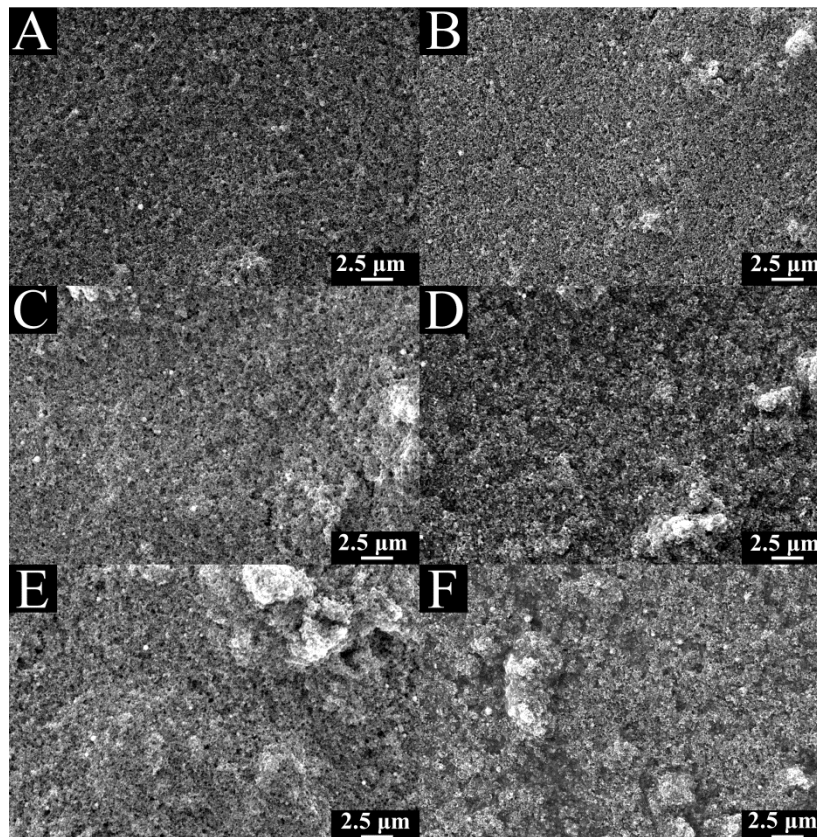


Figure 90: SEM images of LTO powders using CMC- (Left), and PAZO- (Right) assisted EPD, deposited at constant voltage of 10 V (A,B), 30 V (C, D), 50 V(E, F).

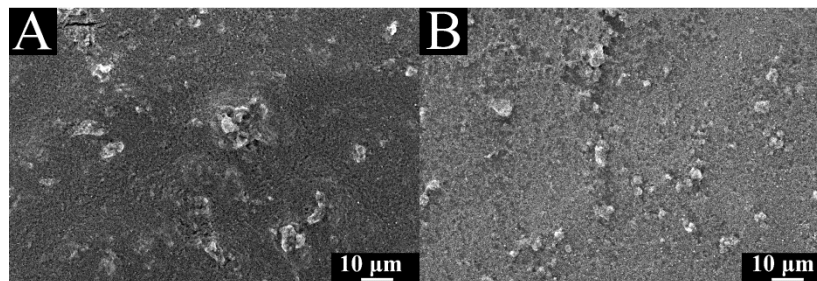


Figure 91: SEM images of LTO deposits at low magnification showing the formation of nodules due to agglomeration. A) CMC deposit at 50V, B) PAZO deposit at 50 V.

Lithium iron phosphate exhibited very good stability in CMC, but rapid settling in PAZO. The settling in PAZO occurred quickly enough to impede the coating quality of the deposit. As seen in Figure 92, only the smallest of suspended LFPO particles coated along

with the PAZO polymer. The quality of the dried coatings with increasing voltages exhibited worsening cracking of the PAZO, with less adhered LFPO particles. On the other hand, CMC based coatings at all voltages exhibited tightly deposited films with little evidence of cracking. However, the CMC deposits exhibited significant surface roughness.

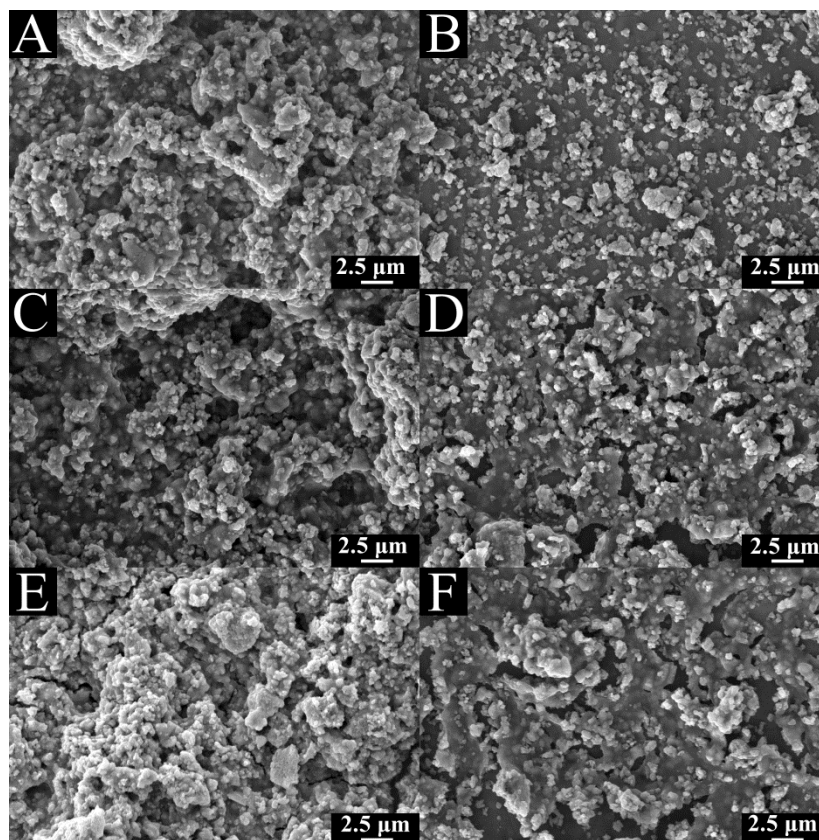


Figure 92: SEM images of LFPO powders using CMC- (Left), and PAZO- (Right) assisted EPD, deposited at constant voltage of 10 V (A,B), 30 V (C, D), 50 V(E, F).

The deposition of LMO particles at 50 V produced the best coatings for both CMC- and PAZO-assisted EPD. At lower voltages (10 V and 30 V), the PAZO coatings provided significantly less coverage than CMC coatings. CMC-based coatings generally had less

defects than those formed with PAZO. This was likely due to the difference in suspension stability of CMC- and PAZO-solutions.

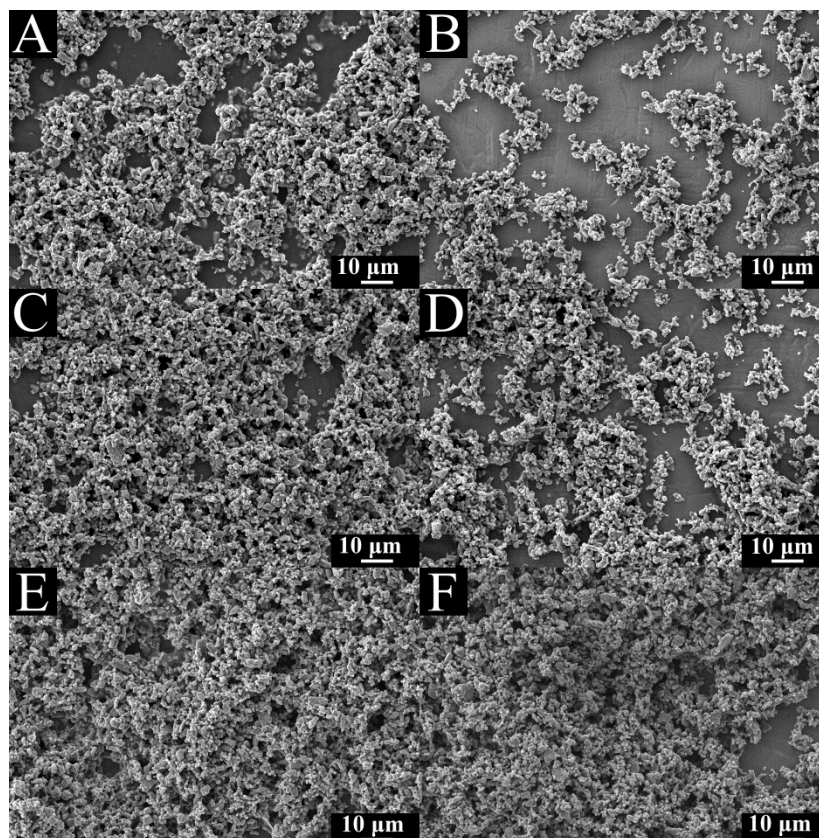


Figure 93: SEM images of LMO powders using CMC- (Left), and PAZO- (Right) assisted EPD, deposited at constant voltage of 10 V (A,B), 30 V (C, D), 50 V (E, F).

The LMNO particles were more difficult to deposit due to the low solution stability. Settling occurred rapidly, preventing uniform coatings from being deposited. The best coating (Figure 94) was achieved from CMC-assisted EPD at 50 V. At lower voltages, the coating quality was poor, leaving significant portions of the electrode uncoated. Coatings using PAZO were less successful than those using CMC. At higher voltages (30 V and 50 V), shrinkage and cracking of thick PAZO films combined with poor deposition of

LMNO particles was observed. At 10 V, PAZO assisted deposition produced coatings of similar quality as low voltage CMC coatings.

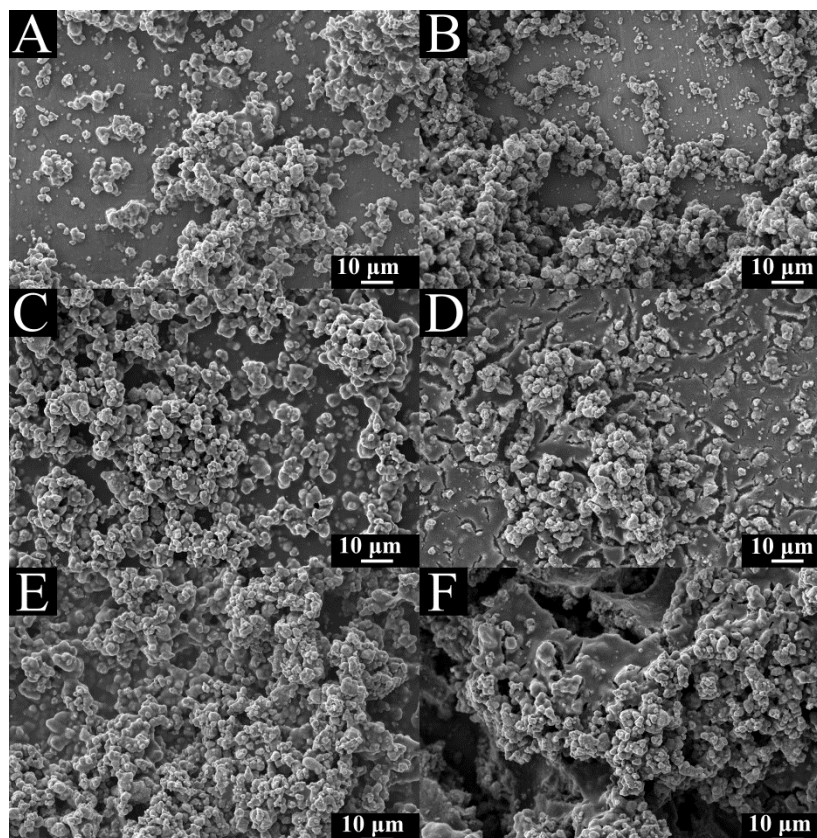


Figure 94: SEM images of LMNO powders using CMC- (Left), and PAZO- (Right) assisted EPD, deposited at constant voltage of 10 V (A,B), 30 V (C, D), 50 V (E, F).

FTIR analysis was performed on the samples above. The deposits were removed from the substrates and lightly crushed prior to testing. The FTIR analysis focused on a wavenumber range of 1200 to 1800 cm^{-1} . Characteristic peaks of both CMC and PAZO are present in this range.

Figure 95 (left) shows the characteristic peaks of fresh CMC, as well as the profiles of the co-deposited powders. The peak at 1589 cm^{-1} and 1412 cm^{-1} corresponded to the

asymmetric and symmetric stretching of the $-\text{COONa}$, respectively. The peak that occurred near 1719 cm^{-1} corresponded to the protonated $-\text{COOH}$ group. This peak was prominent only in the LMNO sample, but can be seen in all other coatings. This indicated that CMC was bonded and co-deposited with the Li-oxide particles.

Figure 95 (right) shows the FTIR results for PAZO and corresponding coatings. The peak near 1675 cm^{-1} corresponded to the vibrations of protonated $-\text{COOH}$ groups, while the peaks at 1589 and 1624 cm^{-1} corresponded to $-\text{COONa}$. The peaks at 1429 and 1456 cm^{-1} are characteristic of the stretching $\text{N}=\text{N}$ bond in PAZO, while the peaks at 1396 and 1488 cm^{-1} were from vibrations in the aromatic rings. Co-deposition of PAZO and Li-oxide particles was observed and verified by FTIR.

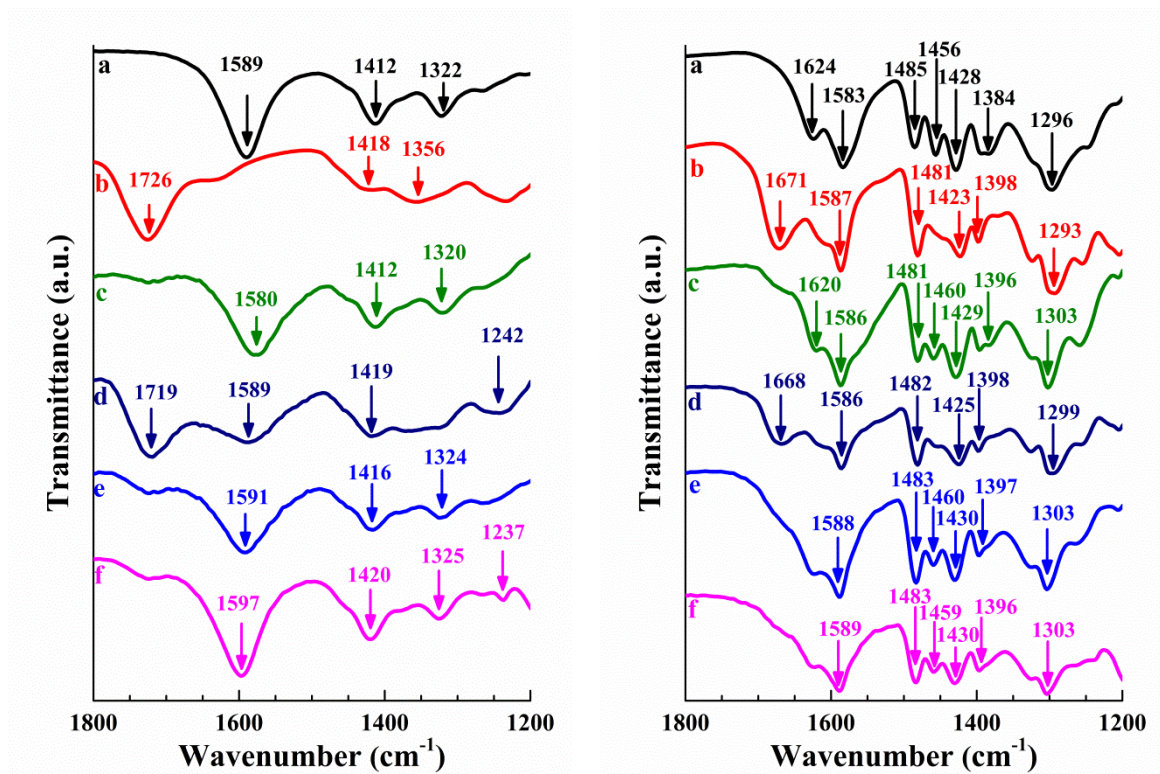


Figure 95: FTIR Profiles of Deposited CMC (Left) PAZO (Right) where: a) Pure Polymer, b) Deposited Polymer, c) LMO, d) LMNO, e) LTO, and f) LFPO.

For the four battery materials, CMC-assisted deposition was shown to be superior to PAZO-assisted deposition. The stability of the CMC suspensions was superior, providing the most uniform coatings. Additionally, it was less susceptible to cracking and shrinkage than PAZO, having less spallation at the edges of the deposit. As such, CMC was exclusively used to deposit material on large 25 cm² electrodes.

Anode Materials / Carbon Black on Aluminum Using CMC

The three cathode materials could readily deposit on their aluminium substrate using CMC as the dispersant and binder. Figure 96 below shows an example of a successful 25 cm² anode produced by CMC-assisted EPD. These cathodes needed an active material loading between 4 and 6 g cm⁻². To deposit 100 to 150 mg of material on each cathode, large solutions needed to be used for two reasons. First, enough solution was needed to cover both the electrodes which required at least a 300 mL beaker. Secondly, several electrodes were to be deposited from a single solution, and depletion of active material would quickly become problematic.



Figure 96: Successful coating of LFPO-CB on Aluminium

The solution used for both LMO and LMNO were concentrated 1 g L^{-1} solutions of CMC in 30% H_2O -ethanol solvent. The concentrations of lithium spinels and graphite materials were 9 g L^{-1} and 1.1 g L^{-1} , respectively. For LMO, deposition times of 3 to 5 minutes at 50 V produced desired mass loading. For LMNO, deposition times of 5 to 7 minutes at 50 V were needed. The Figure 97 shows deposition mass loading with deposition time for both LMO and LMNO. It is important to note that as additional electrodes are produced the concentration of the solution dropped significantly. Figure 98 shows the drop in solution concentration with each additional electrode, as a function of total deposition time. Only the concentration drop from deposit masses was considered, as it was difficult to calculate transfer losses during electrode removal. It can be expected that as concentration dropped, deposition time needed to increase in order to provide identical mass loadings. The concentration of the solution, after 8 electrodes and 30 to 35 minutes of total deposition time, had dropped to approximately 75%.

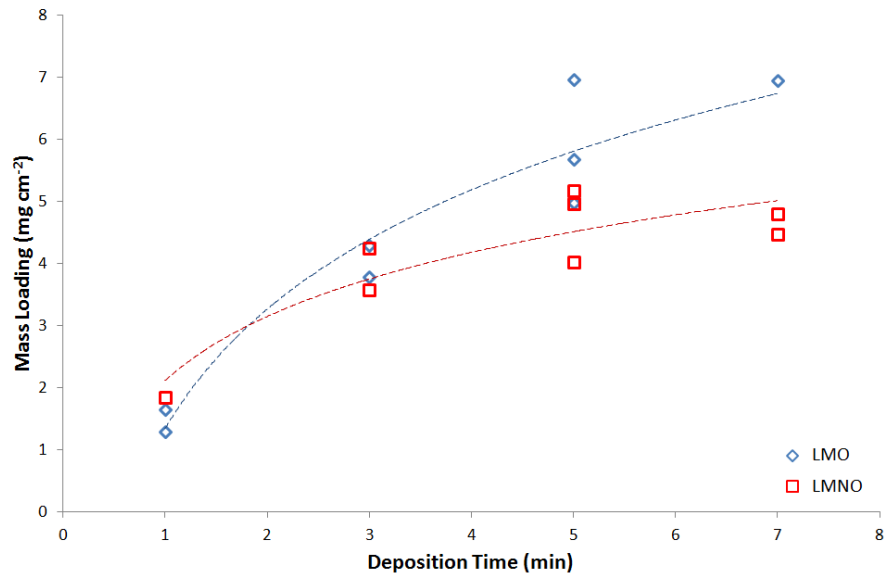


Figure 97: Mass loading of LMO and LMNO cathodes as a function of deposition time.

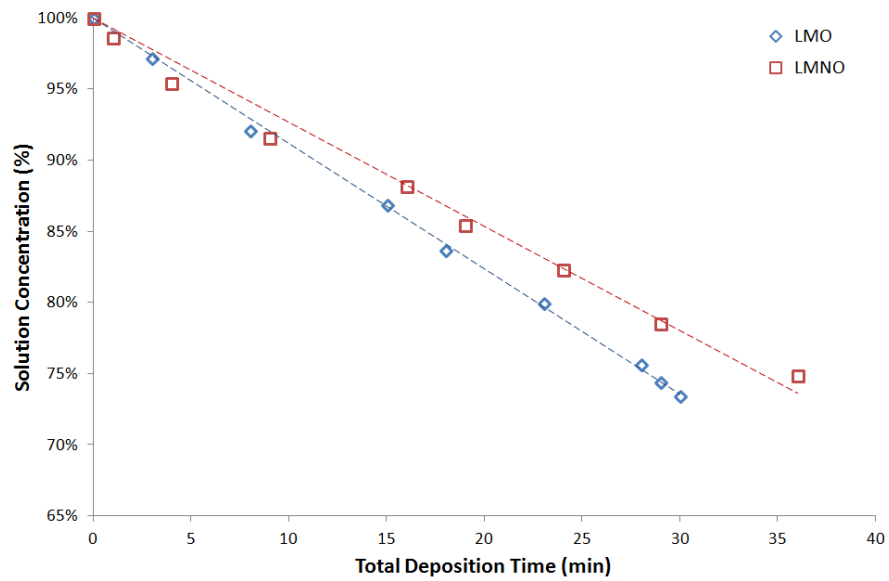


Figure 98: Solution Depletion with each additional electrode deposited.

For LFPO deposition, the solution was diluted to a 50% concentration compared to that of the LMO and LMNO. This was done due to deposition defects when LFPO was deposited at 50 V in concentrated solutions. Large anodes were successfully coated with deposition times between 12 and 15 minutes.

Li₄Ti₅O₁₂ / Carbon Black on Copper Anodes

Unlike the cathode lithium materials, LTO could not be deposited onto its large electrode. Although the suitability tests had shown LTO depositing on steel, the LTO/C deposits from CMC and PAZO assisted EPD cracked, shrank and spalled during drying (Figure 99). The likely hypothesis was that, unlike the anode materials, the LTO particle sizes had diameters under 200 nm. These small particles had very high surface area which could rapidly degrade due to the sudden pH change at the electrode surface during deposition. Waterless solvent systems, primarily mixtures of polyvinyl butyral [PVB] and phosphate ester dissolved in various alcohols were tried; however, none could successfully deposit LTO/C.

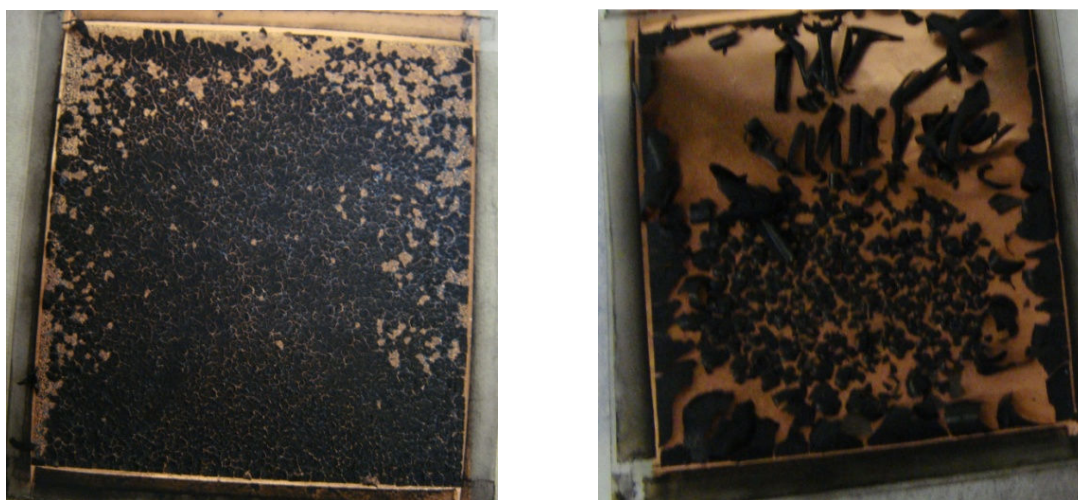


Figure 99: Spallation of LTO-CB electrodes (copper) Left) CMC, Right) PAZO

Performance of Electrodes

The three cathode materials were tested by galvanostatic charge-discharge and cyclic voltammetry. These were performed in the voltage window from 2 V to 4.2 V vs Li. The extended voltage window was expected to increase the cell capacity for each material. The cells were tested using an electrolyte solution of 1 M LiPF₆ in (3:7 volume ratio) ethylene carbonate:diethyl carbonate mixed solvent. In the case of LFPO, the cycling stability was maintained. However, for LMO and LMNO, irreversible reactions caused the capacity to quickly drop.

LiFePO₄/ Carbon Black on Aluminum Using CMC

The CV tests for LFPO showed well defined redox peaks in the range of 3.2 to 3.7 V (Figure 100-Left), which correspond to the extraction and insertion of lithium into the Li_xFePO₄ structure. Extraction of lithium caused oxidation of Fe²⁺ to Fe³⁺, while insertion reversibly reduced it back to Fe²⁺. The electrode showed reversible discharge capacity at all discharge rates, as can be seen from the stable voltage plateaus in Figure 100-Right. The capacity of the cell was tested at different rates (C/10, C/5, C/2, C, 2C, 5C), showing results of 146.7, 138.5, 122.9, 104.9, 87.1, and 56.1 mAh g⁻¹. The capacity at C/10, C/2 and C were slightly lower compared to the ideal values reported by the manufacturer (150, 150, and 131 mAh g⁻¹). Other cells produced by EPD report capacities between 125.8 (C/10) and 54 (5C) mAh g⁻¹, while exhibiting instability at higher charge-discharge rates [94]. The cycling stability of the cell is shown in Figure 101, using a

cycling rate of C/10. The initial coulomb efficiency was 73.5%, but quickly stabilized to above 99% during cycling. The capacity retention of the cell after 50 cycles was 103%.

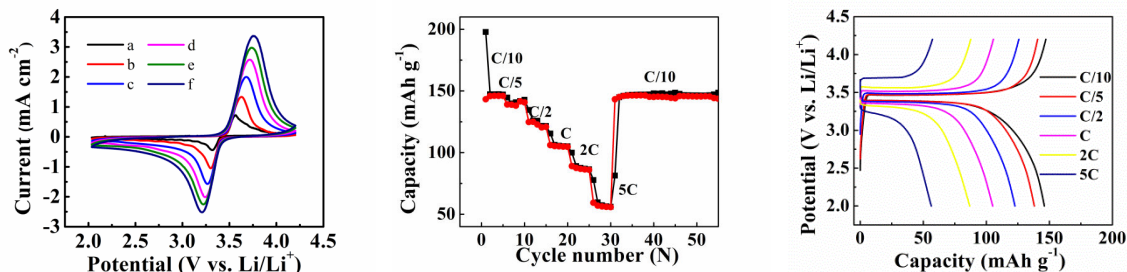


Figure 100: Cell performance of LFPO cathode. Left) Cyclic Voltammetry at sweep rates of a) 0.1, b) 0.2, c) 0.4, d) 0.6, e) 0.8, and f) 1.0 mV s^{-1} . Center) Capacity with varying C-rates, Right) Potential Curve with varying C-rates.

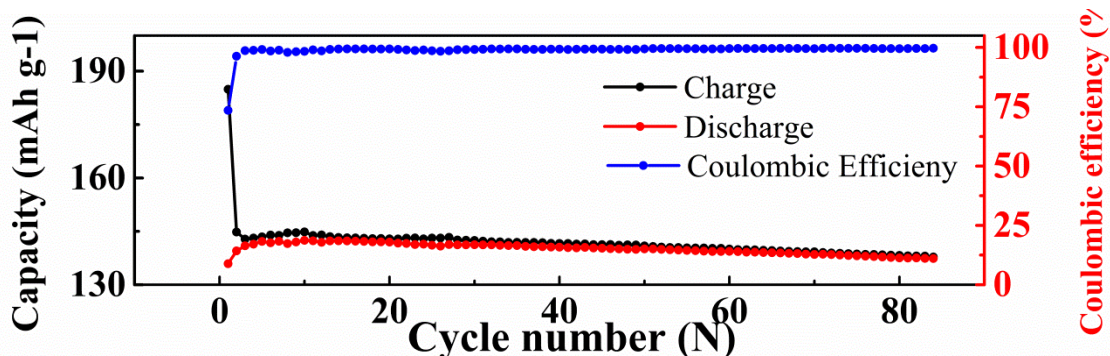


Figure 101: Cycling of LFPO/C Cathode at charge-discharge current of C/10.

LiMn₂O₄ and LiMn_{1.5}Ni_{0.5}O₄ with Carbon Black on Aluminium Using CMC

The LMO and LMNO cells were tested in a voltage window (2 – 4.2 V) that would provide additional capacity. Figure 102 shows the capacity of the LMO cell during cycling at C/10. After 70 cycles, it had lost approximately half its initial capacity. However, the remaining capacity was still above 100 mAh g^{-1} . LMNO on the other hand did not have a significant increase in capacity (Figure 103), and lost most of it within 60 cycles. Figure 104 shows the capacity of the cells with increasing charge-discharge rates.

While LMO shows capacity retention of nearly 20% at 5C, the charge-discharge plateaus are relatively stable. LMNO, on the other hand, shows capacity retention less than 1% at 5C. Additionally, the charge-discharge plateaus are increasingly unstable.

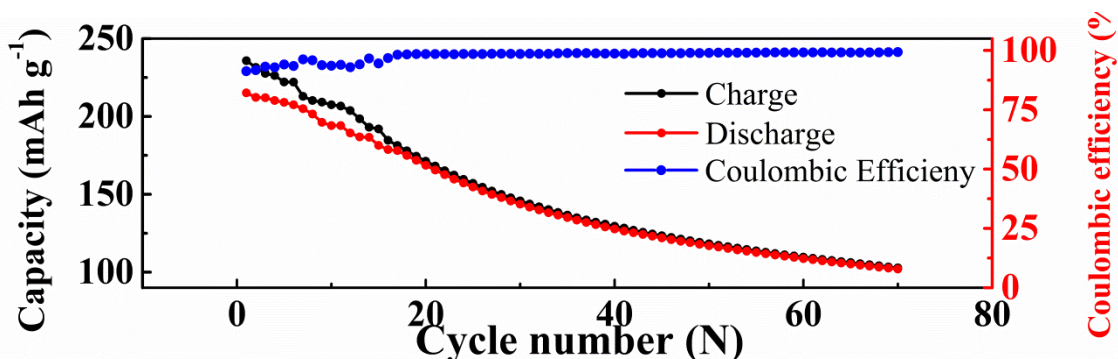


Figure 102: Cycling of LMO/C Cathode at charge-discharge current of C/10.

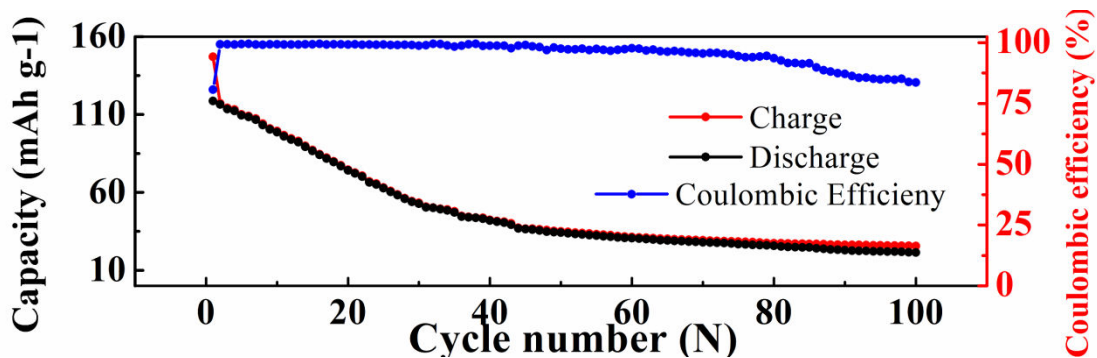


Figure 103: Cycling of LMNO/C Cathode at charge-discharge current of C/10.

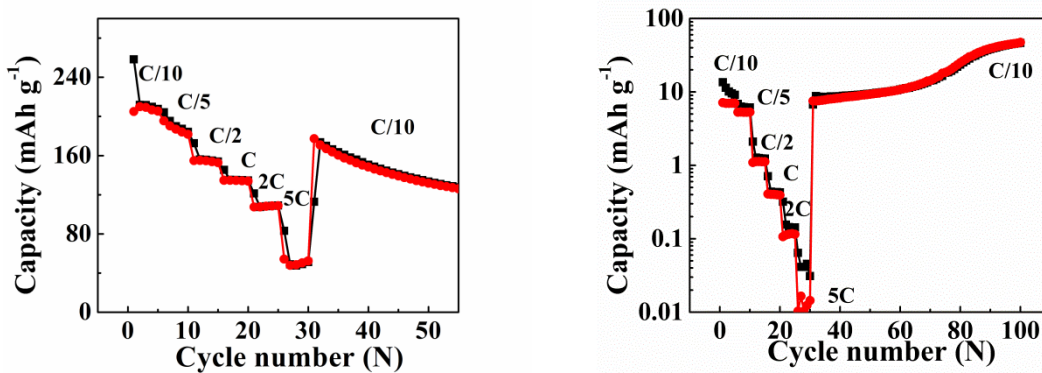


Figure 104: Capacity of LMO (Left) and LMNO (Right) with varying charge-discharge rates.

Conclusion to Li-ion Battery Electrode Materials

This study showed that CMC-Na and PAZO-Na could be used for dispersing, and charging of lithium cathode materials for electrophoretic deposition on electrodes. Oxides deposited using CMC show good adhesion, while PAZO was more prone to cracking and shrinkage. CMC based LiFePO_4 cathodes showed good rate performance and excellent cycling stability. The capacity of 146.7 mAh g^{-1} was achieved at C/10. The LiMn_2O_4 and $\text{LiMn}_{1.5}\text{Ni}_{0.5}\text{O}_4$ were tested in the same voltage window as LiFePO_4 . Although LiMn_2O_4 had an initial capacity of over 200 mAh g^{-1} , it quickly decayed to approximately 100 mAh g^{-1} . $\text{LiMn}_{1.5}\text{Ni}_{0.5}\text{O}_4$ demonstrated even more instability in the extended window.

Overall Conclusions

Four projects were explored over the breadth of the thesis. Each project tackled a different aspect of energy storage devices, had different scopes and experimental methods. The findings are summarized below.

An investigation of ionic conductivity of duplex sodium beta alumina solid electrolytes showed that the porous layer reduced the interfacial resistance, between the BASE and sodium electrode, by up to 75%. The overall resistance of the BASE was also significantly decreased as the dense portion of the duplex was thinned. However, due to failures in experimental methods, the accuracy of the tests was not high. An alternative method of characterizing the ionic conductivity of the duplex BASE should be carried out. One such method would be to produce disks of uniform diameter and measure the changes in conductivity by varying the thicknesses of the dense and porous layers.

The sodium-silicon system was further developed by measuring thermodynamic properties of NaSi by use of DSC as well as EMF activity measurements. The heat of formation for NaSi was measured to be approximately 0.5 kJ mol^{-1} near 350°C . The heat of transformation of NaSi at 612°C measured between 4.5 and 5.8 kJ mol^{-1} . The sodium activity of the NaSi-Na₄Si₂₃ binary phase was in the order of 10^{-1} , indicating that NaSi had low stability. From autoclave melting experiments, NaSi was found to decompose into clathrates rather than show evidence of melting. This information was used to model a new Na-Si binary phase diagram. To further improve the quality of the phase diagram additional determination of thermodynamic properties of NaSi and sodium Si-clathrates is

required. The heat capacity of NaSi can be measured by DSC using the sealed steel crucibles designed in this thesis. Additional EMF measurements of sodium activity at additional compositions and elevated temperatures would be crucial to better model the liquid phase. To do this, EMF cells would need to be designed such that glass seal would not be used. Two options exist here: find a suitable ceramic seal that is not susceptible to sodium vapour, or make cells from a single casting so that no joining is required. The determination of the high temperature NaSi phase crystal structure was attempted using a sealed quartz tube. However, due to the nature of NaSi, the phase decomposed and quartz tube failed prior to reaching the transition temperature. This experiment should be repeated using a method where NaSi can safely be heated to above 612°C. Potentially, a steel capillary could be used with a sufficiently powerful x-ray source. Finally, the electronic conductivity of NaSi at elevated temperature was measured. It was found that the conductivity increased with increasing temperature. A change in the slope of the $\ln(\sigma)$ vs $1/T$ line occurred around 430°C. The reason for this change is still unknown. Additional conductivity measured should be done to better understand the phase.

Bismuth manganese oxide for supercapacitor electrodes was synthesized using a sol gel method. Although the phase was successfully synthesized, after significant ball milling, it provided a maximum of 10 F g⁻¹ at a 2 mV s⁻¹ scan rate. Increasing the scan rate to 100 mV s⁻¹, the capacitance showed retention of only 20%. The capacitive behaviour of the sol gel-synthesized BMO was a fraction of that measured from hydrothermal-synthesized BMO. The effects of particle and grainsize, as well as surface properties of BMO need to be investigated. Changes to the sol gel composition, including the precursor materials, as

well as looking into the effects of calcination temperature, atmosphere and process time could yield increased capacitance.

The feasibility of electrophoretically depositing lithium ion battery electrodes was tested using simple suspensions of common materials and polyanions. The lithium ion electrode materials were $\text{Li}_4\text{Ti}_5\text{O}_{12}$, LiFePO_4 , LiMn_2O_4 and $\text{LiMn}_{1.5}\text{Ni}_{0.5}\text{O}_4$. Two polyanions were used; CMC-Na and PAZO-Na. While both suspended and deposited the electrode materials, CMC provided better coverage. On large electrodes, LTO would crack and spall during drying. This was likely due to the nature of the nano-sized particles and the water-ethanol suspensions. EPD of nano-LTO should explore water-less suspensions. However, the cathode materials were successfully coated on aluminum foil. These were tested in an extended voltage window. While LiFePO_4 retained a high capacity and coulombic efficiency, the spinels both showed rapid performance degradation. The spinel electrodes produced by this EPD method need to be retested in their appropriate voltage windows. Additional work on further stabilizing the suspensions should be done, since the largest particles were required to be suspended after each deposition process.

References

- [1] "67th BP Statistical Review of World Energy," British Petroleum Company, London, 2018.
- [2] D. Kundu, E. Talaie, V. Duffort and L. F. Nazar, "The Emerging Chemistry of Sodium Ion Batteries for Electrochemical Energy Storage," *Angewandte Chemie International*, vol. 54, pp. 3431-3448, 2015.
- [3] M. Kamibayashi and K. Tanaka, "Recent Sodium Sulfur Battery Applications," *IEEE*, pp. 1169-1173, 2001.
- [4] N. Nitta, F. Wu, J. T. Lee and G. Yushin, "Li-ion battery materials: present and future," *Materials Today*, vol. 18, no. 5, pp. 252-264, 2015.
- [5] M. M. Thackeray, C. Wolverton and E. D. Isaacs, "Electrical energy storage for transportation - approaching the limits of, and going beyond, lithium-ion batteries," *Energy & Environmental Science*, vol. 5, pp. 7854-7863, 2012.
- [6] Y.-F. Y. Yao and J. T. Kummer, "Ion Exchange Properties of and Rates of Ionic Diffusion in Beta-ALumina," *Journal of inorganic nuclear chemistry*, vol. 29, pp.

2453-2475, 1967.

- [7] R. M. Dell and P. T. Moseley, "Beta-Alumina Electrolyte for Use in Sodium/Sulfur Batteries: Part 1. Fundamental Properties," *Journal of Power Sources*, vol. 6, pp. 143-160, 1981.
- [8] J. L. Sudworth, "Zebra Batteries," *Journal of Power Sources*, vol. 51, pp. 105-114, 1994.
- [9] J. L. Sudworth and A. R. Tilley, *The Sodium Sulfur Battery*, London: Chapman and Hall Ltd, 1985.
- [10] X. Lu, G. Li, J. Y. Kim, K. D. Meinhardt and V. L. Sprenkle, "Enhanced Sintering of B"-Al₂O₃/YSZ with the Sintering Aids of TiO₂ and MnO₂," *Journal of Power Sources*, vol. 295, pp. 167-174, 2015.
- [11] T. Ohta, M. Harata and A. Imai, "Preferred Orientation on Beta-Alumina Ceramics," *Mat. Res. Bull.* , vol. 11, pp. 1343-1350, 1976.
- [12] J. L. Sudworth, P. Barrow, W. Wong, B. Dunn, G. C. Farrington and J. O. Thomas, "Toward Commercialization of the Beta-Alumina Family of Ionic Conductors," *MRS Bulletin*, pp. 22-26, March 2000.
- [13] A. V. Virkar and L. Viswanathan, "Sodium Penetration in Rapid Ion Conductors," *J. Am. Ceram. Soc.*, vol. 62, no. 9-10, pp. 528-529, 1979.

- [14] A. Mali and A. Petric, "Synthesis of sodium B"-alumina powder by sol-gel combustion," *Journal of the European Ceramic Society*, vol. 32, pp. 1229-1234, 2012.
- [15] G. Zhang, Z. Wen, X. Wu, J. Zhang, G. Ma and J. Jin, "Sol-gel synthesis of Mg²⁺ stabilized Na-B"/B-Al₂O₃ solid electrolyte for sodium anode battery," *Journal of Alloys and Compounds*, vol. 613, pp. 80-86, 2014.
- [16] A. C. Sutorik, S. S. Neo, D. R. Treadwell and R. M. Laine, "Synthesis of Ultrafine B"-Alumina Powders via Flame Spray Pyrolysis of Polymeric Precursors," *J. Am. Ceram. Soc.*, vol. 81, no. 6, pp. 1477-1486, 1998.
- [17] K. Kuribayashi and P. S. Nicholson, "Dense Conductive B"-Al₂O₃ Ceramics by Spray-Freeze/Freeze-Drying," *Mat. Res. Bull.*, vol. 15, pp. 1595-1601, 1980.
- [18] A. Pekarsky and P. S. Nicholson, "The Relative Stability of Spray-Frozen/Freeze-Dried B-Al₂O₃ Powders," *Mat. Res. Bull.*, vol. 15, pp. 1517-1524, 1980.
- [19] Z. Wang, X. Li and Z. Feng, "The Effect of CTAB on the Citrate Sol-gel Process for the Synthesis of Sodium Beta-Alumina Nano-Powders," *Bull. Korean Chem. Soc.*, vol. 32, no. 4, pp. 1310-1314, 2011.
- [20] T. Maki and S. Sakka, "Preparation of Beta-Alumina Fibers by Sol-Gel Method," *Nippon Seramikkusu Kyokai Gakujutsu Ronbunshi*, vol. 97, no. 10, pp. 1082-1086,

1989.

- [21] L. B. Caliman, R. Bouchet, D. Gouvea, P. Soudant and M. C. Steil, "Flash Sintering of ionic conductors: The need of a reversible reaction," *J. Euro. Ceram. Soc.*, vol. 36, pp. 1253-1260, 2016.
- [22] K. B. Hueso, M. Armand and T. Rojo, "High temperature sodium batteries: status, challenges and future trends," *Energy Environ. Sci.*, vol. 6, p. 734–749, 2013.
- [23] J. L. Sudworth, J. Twidell, N. E. Bagshaw and R. M. Dell, "High-Temperature Battery Systems," *Phil Trans. R. Soc. Lond. A*, vol. 354, pp. 1595-1612, 1996.
- [24] C. H. Dustmann, "Advances in ZEBRA batteries," *Journal of Power Sources*, vol. 127, p. 85–92, 2004.
- [25] G. Li, X. Lu, J. Y. Kim, V. V. Viswanathan, K. D. Meinhardt, M. H. Engelhard and V. L. Sprenkle, "An Advanced Na–FeCl₂ ZEBRA Battery for Stationary Energy Storage Application," *Adv. Energy Mater.*, vol. 5, 2015.
- [26] L.-P. Yang, X.-M. Liu, Y.-W. Zhang, H. Yang and X.-D. Shen, "Advanced intermediate temperature sodium copper chloride battery," *Journal of Power Sources*, vol. 272, pp. 987-990, 2014.
- [27] B.-R. Kim, G. Jeong, A. Kim, Y. Kim, M. G. Kim, H. Kim and Y.-J. Kim, "High Performance Na–CuCl₂ Rechargeable Battery toward Room Temperature ZEBRA-

Type Battery," *Adv. Energy Mater.*, vol. 6, 2016.

- [28] X. Lu, G. Li, J. Y. Kim, J. P. Lemmon, V. L. Sprenkle and Z. Yang, "A novel low-cost sodium–zinc chloride battery," *Energy Environ. Sci.*, vol. 6, p. 1837–1843, 2013.
- [29] H. Bohm and G. Beyermann, "ZEBRA batteries, enhanced power by doping," *Journal of Power Sources*, vol. 84, pp. 270-274, 1999.
- [30] R. C. Galloway and S. Haslam, "The ZEBRA electric vehicle battery: power and energy improvements," *Journal of Power Sources*, vol. 80, p. 164–170, 1999.
- [31] J. Prakash, L. Redey and D. R. Vissers, "Effect of Chemical Additives on the Performance of Na/NiCl₂ Cells," *Ionics*, vol. 6, pp. 210-217, 2000.
- [32] R. A. Pett, A. N. Theodore, G. J. Tennenhouse and F. D. Runkle, "Plate-Type Beta" Alumina Electrolytes for an advanced Sodium-sulfur cell design," *Am. Ceram. Soc. Bull.*, vol. 64, no. 4, pp. 589-592, 1985.
- [33] S.-M. Kim, S.-M. Lee, K. Jung, Y.-C. Park, N.-u. Cho and H.-S. Kim, "Feasibility Study of a Planar-type Sodium–Nickel Chloride Battery," *Bull. Korean Chem. Soc.*, vol. 37, p. 695–699, 2016.
- [34] H. J. Chang, X. Lu, J. F. Bonnett, N. L. Canfield, S. Son, Y.-C. Park, K. Jung, V. L. Sprenkle and G. Li, "Development of intermediate temperature sodium nickel

chloride rechargeable batteries using conventional polymer sealing technologies," *Journal of Power Sources*, vol. 348, p. 150e157, 2017.

- [35] E. Mercadelli, A. S. Arico, A. Gondolini, S. Siracusano, M. Ferraro, V. Antonucci and A. Sanson, "Influence of powders thermal activation process on the production of planar B-alumina ceramic membranes," *Journal of Alloys and Compounds*, vol. 696, pp. 1080-1089, 2017.
- [36] T. Wu, S. Zhang, X. Ao, X. Wu, J. Yang and Z. Wen, "Enhanced stability performance of nickel nanowire with 3D conducting network for planar sodium-nickel chloride batteries," *Journal of Power Sources*, vol. 360, pp. 345-352, 2017.
- [37] G. Kim, Y.-C. Park, Y. Lee, N. Cho, C.-S. Kim and K. Jung, "The effect of cathode felt geometries on electrochemical characteristics of sodium sulfur (NaS) cells: Planar vs. tubular," *Journal of Power Sources*, vol. 325, pp. 238-245, 2016.
- [38] K. Jung, J. P. Colker, Y. Cao, G. Kim, Y.-C. Park and C.-S. Kim, "A thermo-mechanical stress prediction model for contemporary planar sodium sulfur (NaS) cells," *Journal of Power Sources*, vol. 324, pp. 665-673, 2016.
- [39] J. Y. Kim, N. L. Canfield, J. F. Bonnett, V. L. Sprenkle, K. Jung and I. Hong, "A duplex β -Al₂O₃ solid electrolyte consisting of a thin dense layer and a porous substrate," *Solid State Ionics*, vol. 278, pp. 192-197, 2015.

- [40] N. L. Canfield, J. Y. Kim, J. F. Bonnett, R. L. Pearson III, V. L. Sprenkle and K. Jung, "Effects of fabrication conditions on mechanical properties and microstructure of duplex B"-Al₂O₃ solid electrolyte," *Materials Science and Engineering B*, vol. 197, pp. 43-50, 2015.
- [41] X. Lu, G. Li, J. Y. Kim, D. Mei, J. P. Lemmon, V. L. Sprenkle and J. Liu, "Liquid-metal electrode to enable ultra-low temperature sodium–beta alumina batteries for renewable energy storage," *Nature Communications*, 2014.
- [42] X. Lu, M. E. Bowden, V. L. Sprenkle and J. Liu, "A Low Cost, High Energy Density, and Long Cycle Life Potassium–Sulfur Battery for Grid-Scale Energy Storage," *Adv. Mater.*, vol. 27, pp. 5915-5922, 2015.
- [43] J.-K. Park, *Principles and Applications of Lithium Secondary Batteries*, Weinheim: Wiley-VCH, 2012.
- [44] Z. Yang, J. Zhang, M. C. W. Kinter-Meyer, X. Lu, D. Choi, J. P. Lemmon and J. Liu, "Electrochemical Energy Storage for Green Grid," *Chem. Rev.*, vol. 111, pp. 3577-3613, 2011.
- [45] F. Wang, O. Borodin, M. S. Ding, S. Greenbaum, K. Xu and C. Wang, "Hybrid Aqueous/Non-aqueous Electrolyte for Safe and High-Energy Li-Ion Batteries," *Joule*, vol. 2, p. 927–937, 2018.

- [46] P. Simon and Y. Gogotsi, "Materials for Electrochemical Capacitors," *Nature Materials*, vol. 7, pp. 845-854, 2008.
- [47] A. Gonzalez, E. Goikolea, J. A. Barrena and R. Mysyk, "Review on supercapacitors: Technologies and materials," *Renewable and Sustainable Energy Reviews*, vol. 58, pp. 1189-1206, 2016.
- [48] E. F. Bertaut, G. Buisson, S. Quezel-Ambrunez and G. Quezel, "STRUCTURE MAGNETIQUE ET PROPRIETES MAGNETIQUES DE BiMn₂O₅," *Solid State Communications*, vol. 5, pp. 25-30, 1967.
- [49] I. Fier, L. Walmsley and J. A. Souza, "Relaxor behavior in multiferroic BiMn₂O₅ ceramics," *Journal of Applied Physics*, vol. 110, 2011.
- [50] I. Fier, D. L. Chinaglia, L. Walmsley, E. C. Pereira, A. C. Rabelo and R. G. Freitas, "Contribution of an extrinsic mechanism for the electrical polarization in BiMn₂O₅ Ceramics," *AIP Advances*, vol. 2, 2012.
- [51] Q. Liu, D. Sallagoity, M. Josse and O. Toulemonde, "On the Anomalous Magnetic Behavior and the Multiferroic Properties in BiMn₂O₅," *Inorganic Chemistry*, vol. 52, pp. 7853-7861, 2013.
- [52] Z. H. Sun, B. L. Cheng, S. Dai, K. J. Jin, Y. L. Zhou, H. B. Lu, Z. H. Chen and G. Z. Yang, "Effect of Ce substitution on magnetic and dielectric properties of BiMn₂O₅,"

Journal of Applied Physics, vol. 99, 2006.

- [53] G. Huo, Z. Gu and M. Qiu, "Phase relations in the $\text{Bi}_2\text{O}_3\text{--Fe}_2\text{O}_3\text{--MnO}_y$ system at room temperature," *Journal of Alloys and Compounds*, vol. 381, pp. 317-319, 2004.
- [54] N. Nguyen, M. Legrain, A. Ducouret and B. Raveau, "Distribution of Mn^{3+} and Mn^{4+} species between octahedral and square pyramidal sites in $\text{Bi}_2\text{Mn}_4\text{O}_{10}$ -type structure," *J. Mater. Chem.*, vol. 9, pp. 731-734, 1999.
- [55] R.-J. Jia, J.-T. Han, X.-J. Wu, C.-L. Wu, Y.-H. Huang and W. Huang, "Controllable synthesis and magnetic property of BiMn_2O_5 crystals," *Materials Research Bulletin*, vol. 43, p. 1702–1708, 2008.
- [56] Y. Chen, H. Yuan, G. Tian, G. Zhang and S. Feng, "Hydrothermal synthesis and magnetic properties of RMn_2O_5 ($\text{R} = \text{La, Pr, Nd, Tb, Bi}$) and $\text{LaMn}_2\text{O}_5+\text{d}$," *Journal of Solid State Chemistry*, vol. 180, pp. 1340-1346, 2007.
- [57] V. T. Santana, L. Walmsley, I. Fier, R. A. Eichel, P. Jakes, I. Chumak, A. Ozarowski, J. van Tol and O. R. Nascimento, "Antiferromagnetic resonance of polycrystalline BiMn_2O_5 ," *Solid State Communications*, vol. 207, pp. 40-43, 2015.
- [58] Y. Q. Lin, Y. J. Wu, X. M. Chen, S. P. Gu, J. Tong and S. Guan, "Dielectric relaxation mechanisms of BiMn_2O_5 ceramics," *Journal of Applied Physics*, vol. 105,

2009.

- [59] Y. Liu and I. Zhitomirsky, "Electrochemical supercapacitor based on multiferroic BiMn₂O₅," *Journal of Power Sources*, vol. 284, pp. 377-382, 2015.
- [60] M. N. Rahaman, *Ceramic Processing and Sintering*, 2nd ed., New York: Marcel Dekker Inc, 2003.
- [61] J. Sangster and A. D. Pelton, "The Na-Si (Sodium-Silicon) System," *Journal of Phase Equilibria*, vol. 1, pp. 67-68, 1992.
- [62] H. Kawaji, H.-o. Horie, S. Yamanaka and M. Ishikawa, "Superconductivity in the Silicon Clathrate Compound (Na,Ba)_xSi₄₆," *Physical Review Letters*, vol. 74, no. 8, 1995.
- [63] G. S. Nolas, M. Beekman, J. Griko, G. A. Lamberton, T. M. Tritt and P. F. McMillan, "Thermal conductivity of elemental crystalline silicon clathrate Si₁₃₆," *Applied Physics Letters*, vol. 82, no. 6, pp. 910-912, 2003.
- [64] M. Beekman and G. S. Nolas, "Synthesis and thermal conductivity of type II silicon clathrates," *2006*, vol. 383, pp. 111-114, Physics B.
- [65] G. S. Nolas, J. M. Ward, J. Gryko, L. Qiu and M. A. White, "Transport properties of Na₈Si₄₆," *Physical Review B*, vol. 64, 2001.

- [66] B. Liu, X. Jia, D. Huo, H. Sun, Y. Zhang, B. Sun, H. Liu, L. Kong and H. Ma, "Evolution of thermoelectric properties of substituted Si-based clathrates prepared by HPHT," *Journal of Alloys and Compounds*, vol. 666, pp. 93-97, 2016.
- [67] J. Gryko, P. F. McMillan, R. F. Marzke, G. K. Ramachandran, D. Patton, S. K. Deb and O. F. Sankey, "Low-density framework form of crystalline silicon with a wide optical band gap," *Physical Review B*, vol. 62, no. 12, 2000.
- [68] R. Himeno, T. Kume, F. Ohashi, T. Ban and S. Nonomura, "Optical absorption properties of $\text{Na}_x\text{Si}_{136}$ clathrate studied by diffuse reflection spectroscopy," *Journal of Alloys and Compounds*, vol. 574, pp. 398-401, 2013.
- [69] R. Himeno, F. Ohashi, T. Kume, E. Asai, T. Ban, T. Suzuki, T. Iida, H. Habuchi, Y. Tsutsumi, H. Natsuhara and S. Nonomura, "Optical band gap of semiconductive type II Si clathrate purified by centrifugation," *Journal of Non-Crystalline Solids*, vol. 358, p. 2138–2140, 2012.
- [70] M. Beekman, M. Baitinger, H. Borrmann, W. Schnelle, K. Meier, G. S. Nolas and Y. Grin, "Preparation and Crystal Growth of $\text{Na}_{24}\text{Si}_{136}$," *J. Am. Chem. Soc.*, vol. 131, no. 28, pp. 9642-9643, 2009.
- [71] H.-o. Horie, T. Kikudome, K. Teramura and S. Yamanaka, "Controlled thermal decomposition of NaSi to derive silicon clathrate compounds," *Journal of Solid State Chemistry*, vol. 182, pp. 129-135, 2009.

- [72] H. Yamane, H. Morito and M. Uchikoshi, "Formation of Si grains from a NaSi melt prepared by reaction of SiO₂ and Na," *Journal of Crystal Growth*, vol. 377, pp. 66-71, 2013.
- [73] H. Morito, M. Uchikoshi and H. Yamane, "Boron removal by dissolution and recrystallization of silicon in a sodium–silicon solution," *Separation and Purification Technology*, vol. 118, pp. 723-726, 2013.
- [74] T. Yamada, H. Sato and H. Yamane, "Preparation of Niobium Disilicide Coating by Heating Niobium in a Sodium Silicon melt," *Materials Transactions*, vol. 53, no. 12, pp. 2141-2144, 2012.
- [75] A. P. Wallace, "Sodium Silicide and the Development of the Portable Hydrogen Energy Market," *ECS Transactions*, vol. 42, no. 1, pp. 219-230, 2012.
- [76] T. Agrawal, R. Ajitkumar, R. Prakash and G. Nandan, "Sodium Silicide As A Hydrogen Source For Portable Energy Devices: A Review," *Materials Today: Proceedings*, vol. 5, p. 3563–3570, 2018.
- [77] "Silicide-Based Hydrogen Generation for Back-Up Power and Portable Fuel Cells," SiGNa Hydrogen Energy, 2013.
- [78] V. L. Chevrier and G. Ceder, "Challenges for Na-ion Negative Electrodes," *Journal of The Electrochemical Society*, vol. 158, no. 9, pp. A1011-A1014, 2011.

- [79] Y. Xu, E. Swaans, S. Basak, H. W. Zandbergen, D. M. Borsa and F. M. Mulder, "Reversible Na-Ion Uptake in Si Nanoparticles," *Adv. Energy Mater.*, vol. 6, 2016.
- [80] D.-F. Qiu, X. Ma, J.-D. Zhang, Z.-X. Lin and B. Zhao, "Mesoporous Silicon Microspheres Produced from In Situ Magnesiothermic Reduction of Silicon Oxide for High-Performance Anode Material in Sodium-Ion Batteries," *Nanoscale Research Letters*, 2018.
- [81] H. Morito, T. Yamada, T. Ikeda and H. Yamane, "Na–Si binary phase diagram and solution growth of silicon crystals," *Journal of Alloys and Compounds*, vol. 480, pp. 723-726, 2009.
- [82] A. Mali and A. Petric, "EMF Measurements of the Na-Si System," *Journal of Phase Equilibria and Diffusion*, vol. 34, no. 6, pp. 453-458, 2013.
- [83] H. Morito, T. Karahashi and H. Yamane, "Condition of Si crystal formation by vaporizing Na from NaSi," *Journal of Crystal Growth*, vol. 355, pp. 109-112, 2012.
- [84] D. Hao, M. Bu, Y. Wang, Y. Tang, Q. Gao, M. Wang, B. Hu and Y. Du, "THERMODYNAMIC MODELING OF THE Na–X (X = Si, Ag, Cu, Cr) SYSTEMS," *J. Min. Metall. Sect. B-Metall.*, vol. 48, no. 2, pp. 273-282, 2012.
- [85] A. Mali and A. Petric, "New Ceramic Seal for Na/NiCl₂ Cells," *J. Am. Ceram. Soc.*, vol. 94, no. 10, pp. 3346-3349, 2011.

- [86] S. Kim, J. H. Joo, S.-D. Kim and S.-K. Woo, "Evaluation of CaO–Al₂O₃ adhesive bonding properties for β –Al₂O₃ solid electrolyte sealing for alkali metal thermal electric converter," *Ceramics International*, vol. 39, pp. 9223–9227, 2013.
- [87] S.-M. Kim, S.-M. Lee, K. Jung, Y.-C. Park, N.-U. Cho, J.-H. Choi and H.-S. Kim, "Influence of Carbon Coating on Beta-Alumina Membrane for Sodium–Nickel Chloride Battery," *Bull. Korean Chem. Soc.*, vol. 36, p. 2869–2874, 2015.
- [88] L. A. Stearns, J. Gryko, J. Diefenbacher, G. K. Ramachandran and P. F. McMillan, "Lithium monosilicide (LiSi), a low-dimensional silicon-based material prepared by high pressure synthesis: NMR and vibrational spectroscopy and electrical properties characterization," *Journal of Solid State Chemistry*, vol. 173, p. 251–258, 2003.
- [89] I. Barin, O. Knacke and O. Kubaschewski, Thermochemical properties of inorganic substances, Düsseldorf: Springer-Verlag Berlin Heidelberg, 1977.
- [90] D. F. Smith, "THE CONDITION OF BISMUTH SALTS IN AQUEOUS SOLUTIONS AND THE MOLAL ELECTRODE-POTENTIAL OF BISMUTH," *J. Am. Chem. Soc.*, vol. 45, no. 2, p. 360–370, 1923.
- [91] Y. Wang, J. Guo, T. Wang, J. Shao, D. Wang and Y.-W. Yang, "Mesoporous Transition Metal Oxides for Supercapacitors," *Nanomaterials*, vol. 5, pp. 1667–1689, 2015.

- [92] R. Poon and I. Zhitomirsky, "Supercapacitor electrodes with high active mass loading," *MRS Communications*, vol. 8, p. 1135–1138, 2018.
- [93] C. H. NG, H. N. Lim, S. Hayase, Z. Zainal, S. Shafie and N. M. Huang, "Effects of Temperature on Electrochemical Properties of Bismuth Oxide/Manganese Oxide Pseudocapacitor," *Ind. Eng. Chem. Res.*, vol. 57, pp. 2146-2154, 2018.
- [94] M. Yilmaz, S. Raina, S.-H. Hsu and W. P. Kang, "Micropatterned arrays of vertically-aligned CNTs grown on aluminum as a new cathode platform for LiFePO₄ integration in lithium-ion batteries," *Ionics*, 2018.

Appendix

Appendix: Ceramic Compositions Used for Sealing BASE Tubes

#	Composition (x by mol)		Sintering Temperatures	Result
1	$\text{CaO}_{(1-x)} - (\text{Al}_2\text{O}_3)_x$	$x = 0.5$	1450 – 1650°C	Destruction of tubes & caps
2	$\text{Na}_2\text{O}_{(1-x)} - (\text{Al}_2\text{O}_3)_x$	$x = 0.65$	1600 – 1650°C	Incomplete sealing Weak bonding strength
		$x < 0.5$	1600 – 1650°C	Glassy, hollow seal Weak bonding strength
3	$(\#1)_{(1-x)} - (\#2)_x$	$x = 0 - 1$	1600 – 1650°C	Incomplete sealing Damage to tubes & caps
4	$(\#2)_{(1-x)} - (\text{Ga}_2\text{O}_3)_x$	$x < 0.2$	1600 – 1650°C	No melting of seal
5	$(\#2)_{(1-x)} - (\text{GeO}_2)_x$	$x < 0.2$	1600 – 1650°C	No melting of seal
6	$\text{Na}_2\text{O}_{(1-x)} - (\text{Ga}_2\text{O}_3)_x$	$x > 0.6$	1450 – 1650°C	No melting of seal
		$x \approx 0.1$	1200°C	No bonding
7	$\text{Corning}_{(1-x)} - (\text{Ga}_2\text{O}_3)_x$	$x_{\text{mass}} < 0.7$	1325°C	Weak bonding strength
		$x_{\text{mass}} > 0.7$		No melting of seal
8	$\text{Corning}_{(1-x)} - (\text{Al}_2\text{O}_3)_x$	$x_{\text{mass}} < 0.7$	1325°C	Weak bonding strength
		$x_{\text{mass}} > 0.7$		No melting of seal
9	$(\text{NaH}_2\text{PO}_4)_{(1-x)} - (\text{Al}_2\text{O}_3)_x$	$x = 0 - 1$	1600 – 1650°C	Weak bonding strength
10	$(\#2)_{(1-x)} - (\#9)_x$	$x < 0.2$	1600 – 1650°C	Incomplete sealing
11	$(\text{Na, Mg, Al})(\text{NO}_3)_{(1-3)}$	—	400 – 1100°C	No bonding
12	$(\text{NaNO}_3)_{(1-x)} - (\text{Al}_2\text{O}_3)_x$	$x = 0.6 - 0.9$	1400 – 1650°C	Incomplete sealing
13	NaAlO_2	—	1400 – 1650°C	No bonding
14	$(\text{NaAlO}_2)_{(1-x)} - (\text{Al}_2\text{O}_3)_x$	$x = 0 - 1$	1400 – 1650°C	No bonding

Appendix: Impedance Spectroscopy of BiMn_2O_5 Electrodes

Bulk Electrode (Pre-Ball Milling $2.65\ \mu\text{m}$)

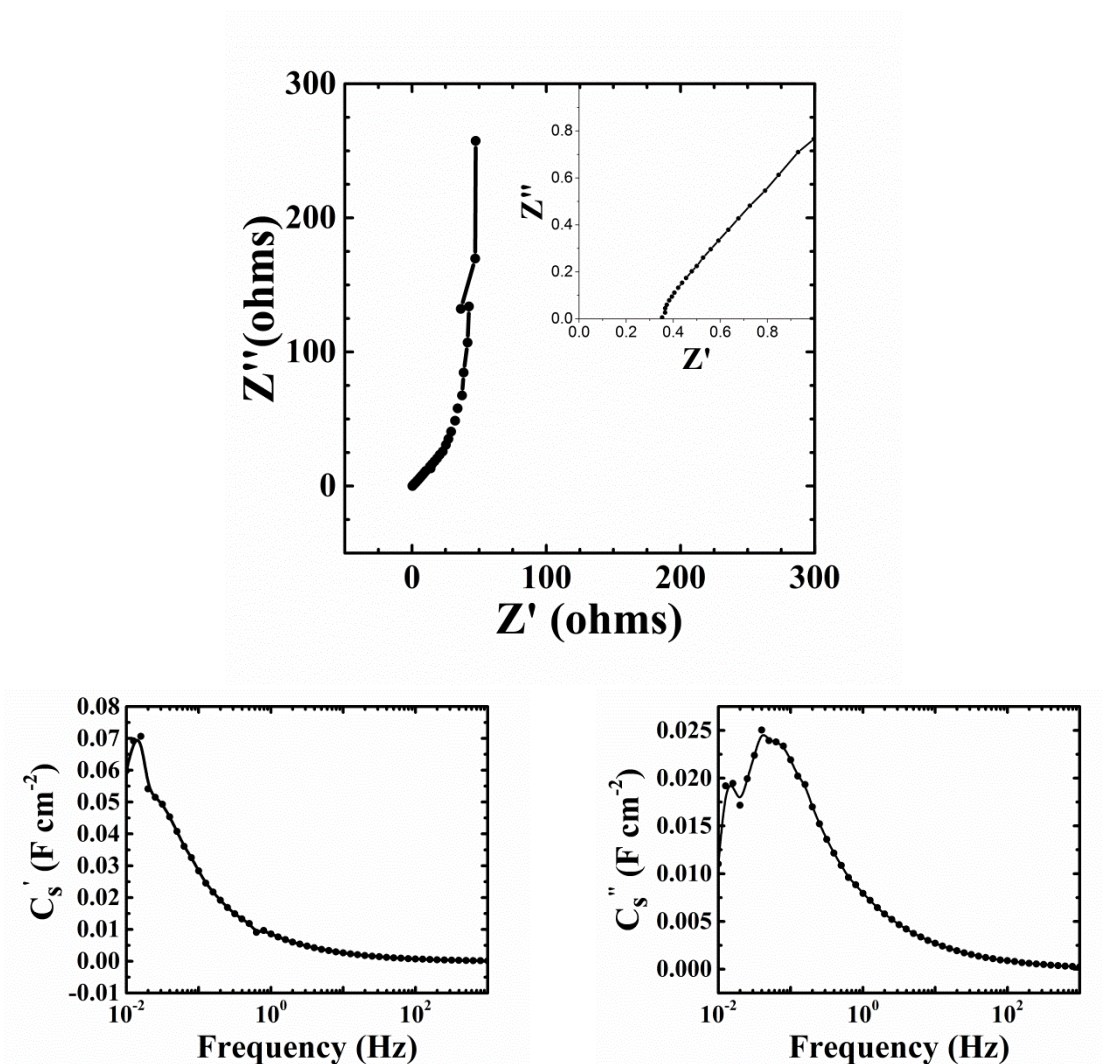


Figure 105-Appendix: Impedance characterization of Bulk BiMn_2O_5 Electrode (Pre Milling, $2.65\ \mu\text{m}$). Top) Nyquist plots of complex impedance. Left) C' , Right) C'' components of complex capacitance.

Bulk Electrode (Ball Milling 1.28 μm)

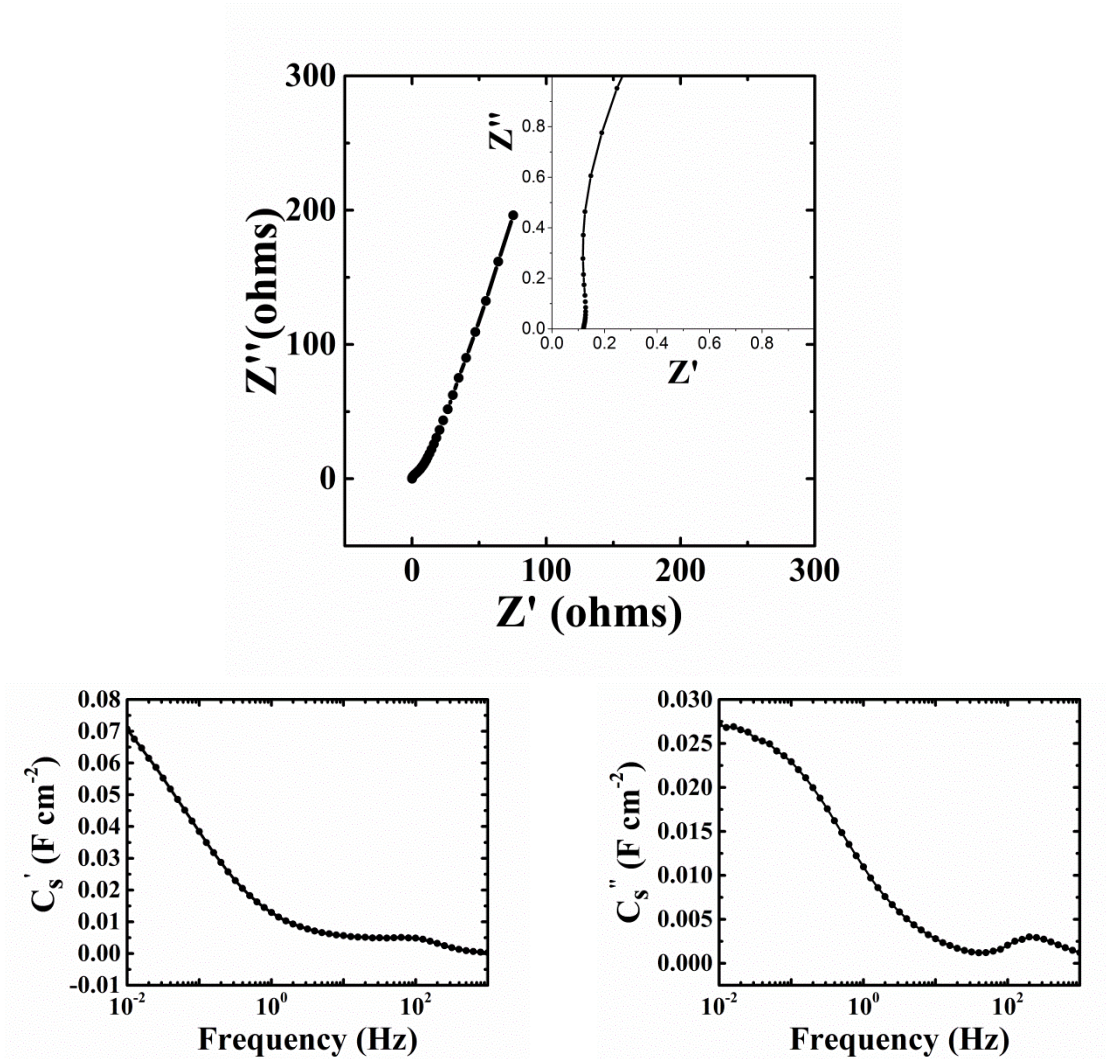


Figure 106-Appendix: Impedance characterization of Bulk BiMn_2O_5 Electrode (Milling to 1.28 μm). Top) Nyquist plots of complex impedance. Left) C' , Right) C'' components of complex capacitance.

Bulk Electrode (Ball Milling 0.23 μm)

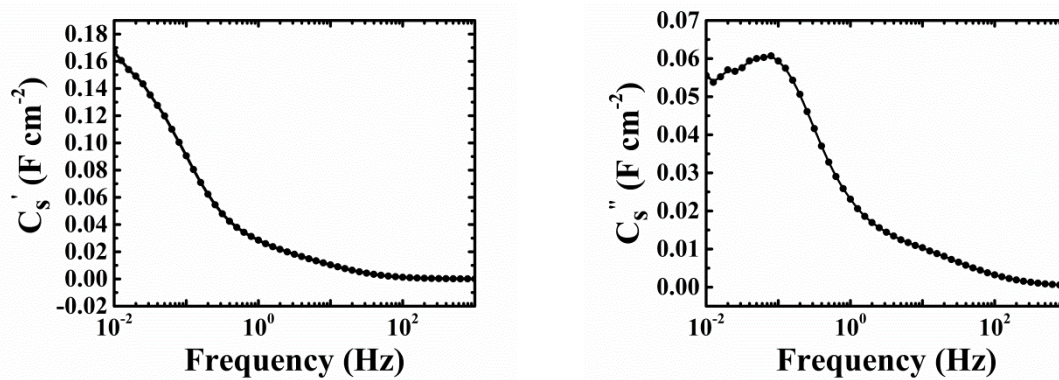
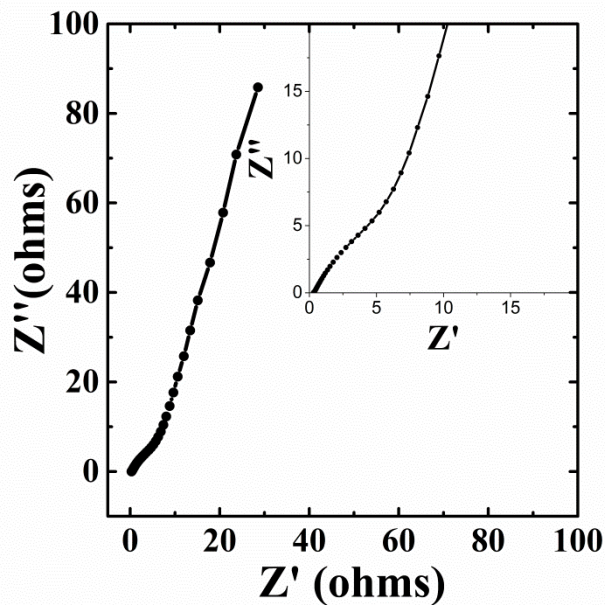


Figure 107-Appendix: Impedance characterization of Bulk BiMn_2O_5 Electrode (Milling to 0.23 μm). Top) Nyquist plots of complex impedance. Left) C_s' , Right) C_s'' components of complex capacitance.

Thin Film Electrode (Separated 1 μm)

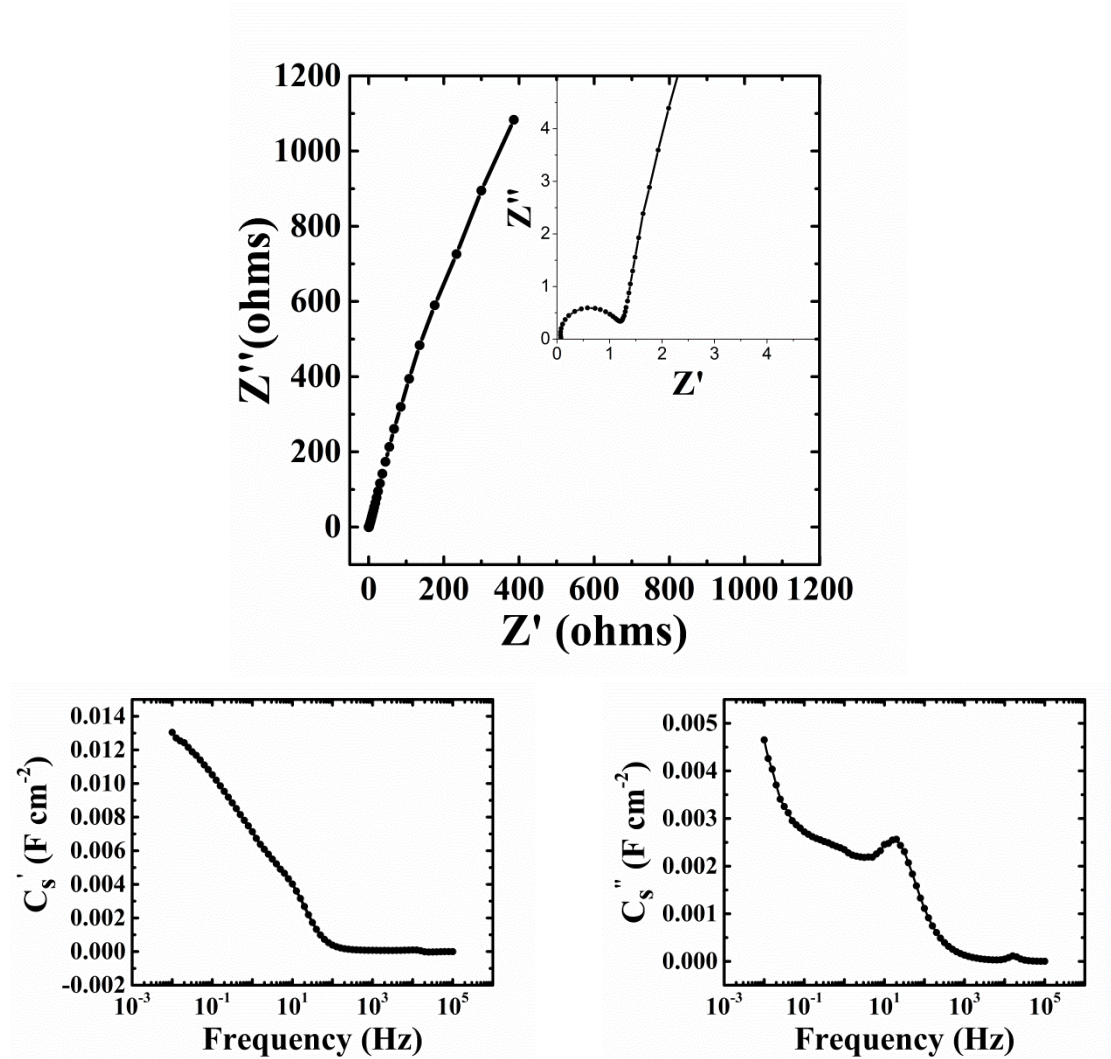


Figure 108-Appendix: Impedance characterization of Thin Film BiMn₂O₅ Electrode (Sedimentation separated to 1.00 μm). Top) Nyquist plots of complex impedance. Left) C' , Right) C'' components of complex capacitance.

Appendix: Important Powder Diffraction Profiles

Sodium Silicon System

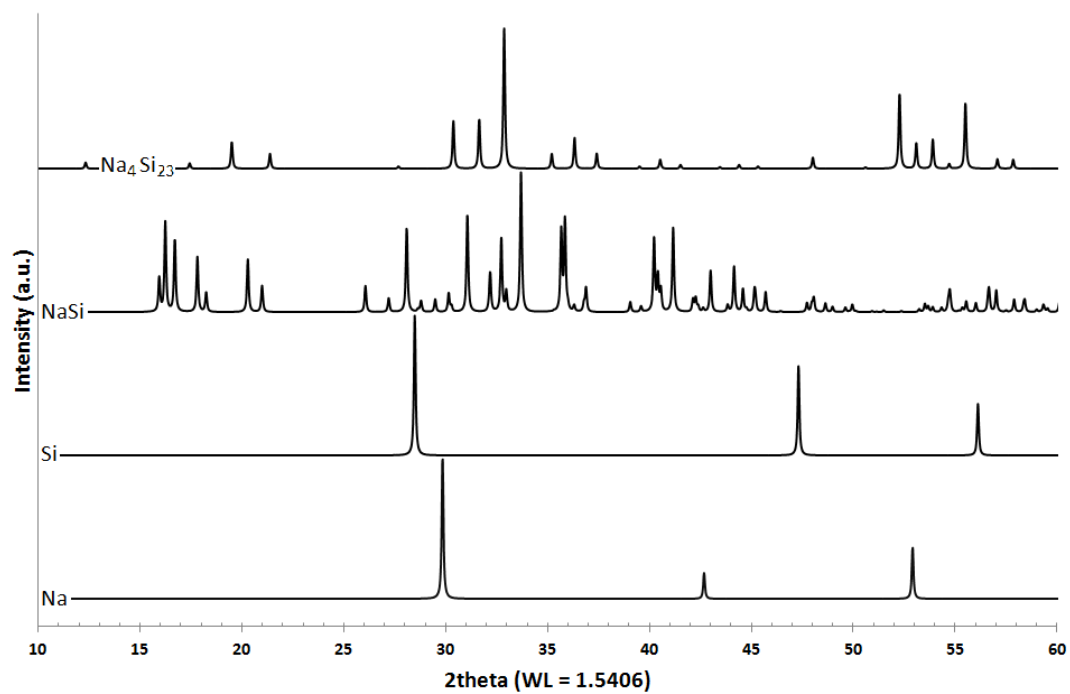


Figure 109-Appendix: XRD Pattern for Sodium (ICSD: 44757), Silicon (ICSD: 51688), NaSi (ICSD: 409953), and Na₄Si₂₃ (ICSD: 50796), used in NaSi powder characterization.

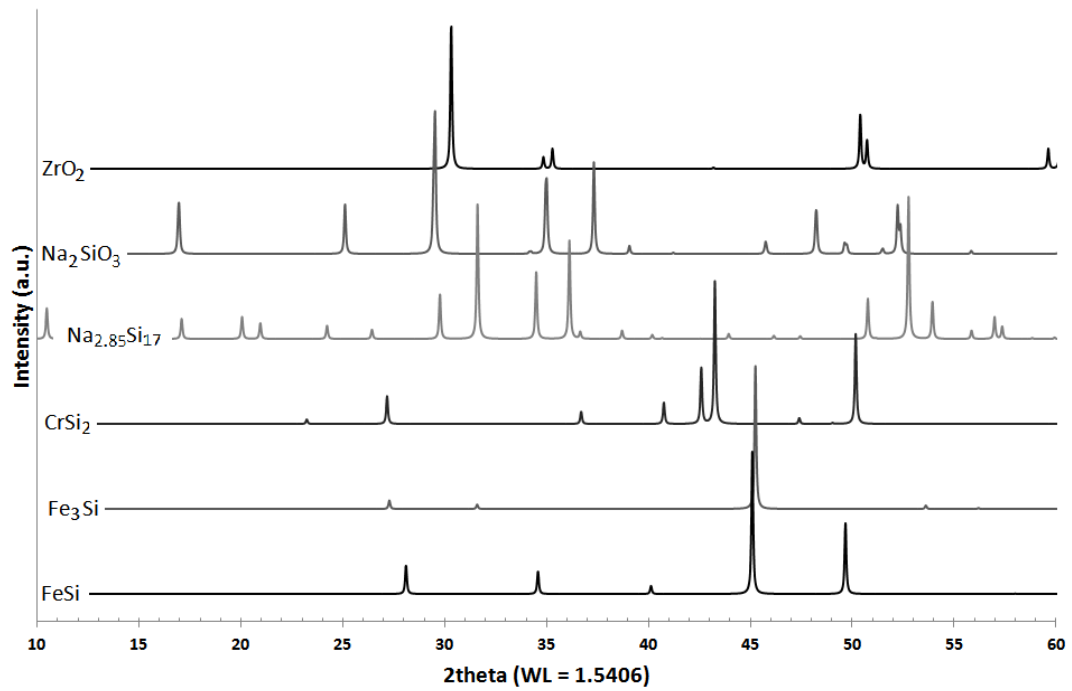


Figure 110-Appendix: XRD Pattern for FeSi (ICSD: 402781), Fe₃Si (ICSD: 412838), CrSi₂ (ICSD: 96026), Na_{2.85}Si₁₇ (ICSD: 248167), Na₂SiO₃ (ICSD: 15388), and ZrO₂ (ICSD: 85322) used in NaSi powder characterization.

Bismuth Manganese Oxide System

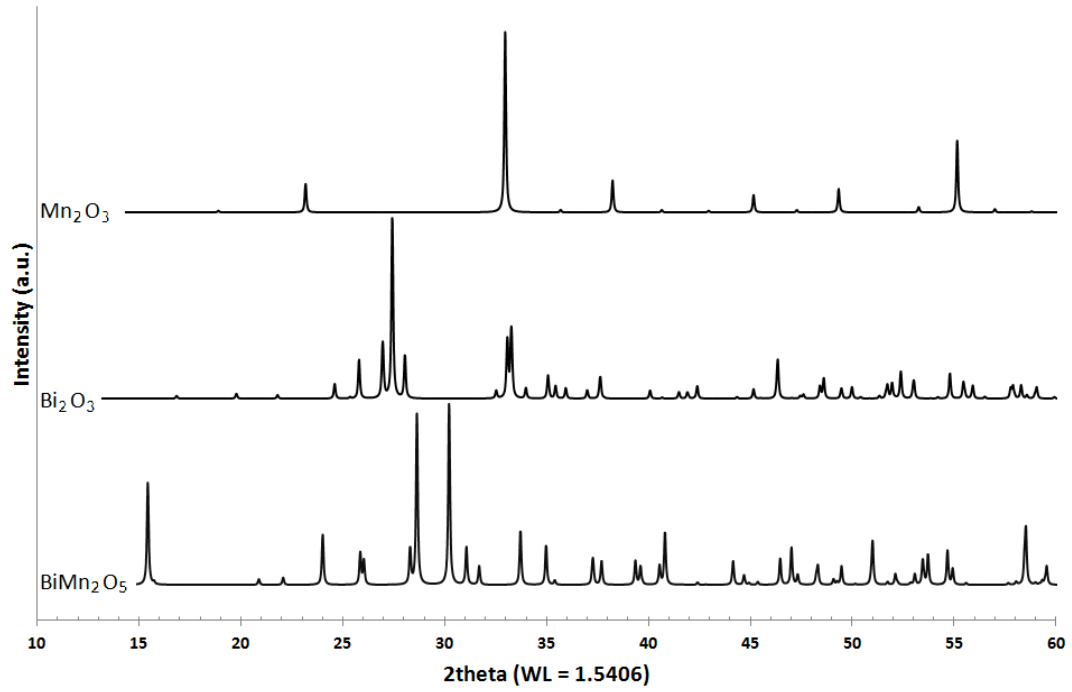


Figure 111-Appendix: XRD Pattern for Mn_2O_3 (ICSD: 159865), Bi_2O_3 (ICSD: 15072), and $BiMn_2O_5$ (ICSD; 169734), used in BMO powder characterization.